



POLITECNICO
MILANO 1863

SCUOLA DI INGEGNERIA INDUSTRIALE
E DELL'INFORMAZIONE

Comprehensive Analysis of Bevel and Hypoid Gears: Experimental Studies, Simulation Modelling, and In-Depth Evaluation of the FZG Hypoid Test Rig

TESI DI LAUREA MAGISTRALE IN
MECHANICAL ENGINEERING - INGEGNERIA MECCANICA

Authors:

Utku Ayrancilar & Tural Aghayev

Student IDs: 990864 & 995598
Advisors: Prof. Carlo Gorla & Prof. Karsten Stahl
Co-advisors: Luca Bonaiti & Lorenz Constien
Academic Year: 2022-2023

Abstract

Thanks to the possibility of transmitting rotating power between perpendicular axes, together with their relatively easy and well-established manufacturing, bevel and hypoid gears have a widespread application. Indeed, they are adopted in all industrial sectors. Thus, there is an industrial call for scientific research on all their aspects, one of which is the investigation of microgeometry, treatments, and materials with respect to the gear pair load-carrying capacity with respect to the several failure modes affecting gears (e.g., macro and micro pitting, tooth root fatigue fracture, scuffing, etc.). Typically, this kind of research is performed on a geared test rig, mainly with a back-to-back configuration. However, in the last few years, an increase in the experimental scatter has been observed on such test rigs.

With reference to the test rig present at the Forschungsstelle für Zahnräder und Getriebesysteme (FZG, Gear Research Center) and to the failure mode of macro and micro pitting, this thesis focuses on the definition and evaluation of possible factors influencing such experimental scatter.

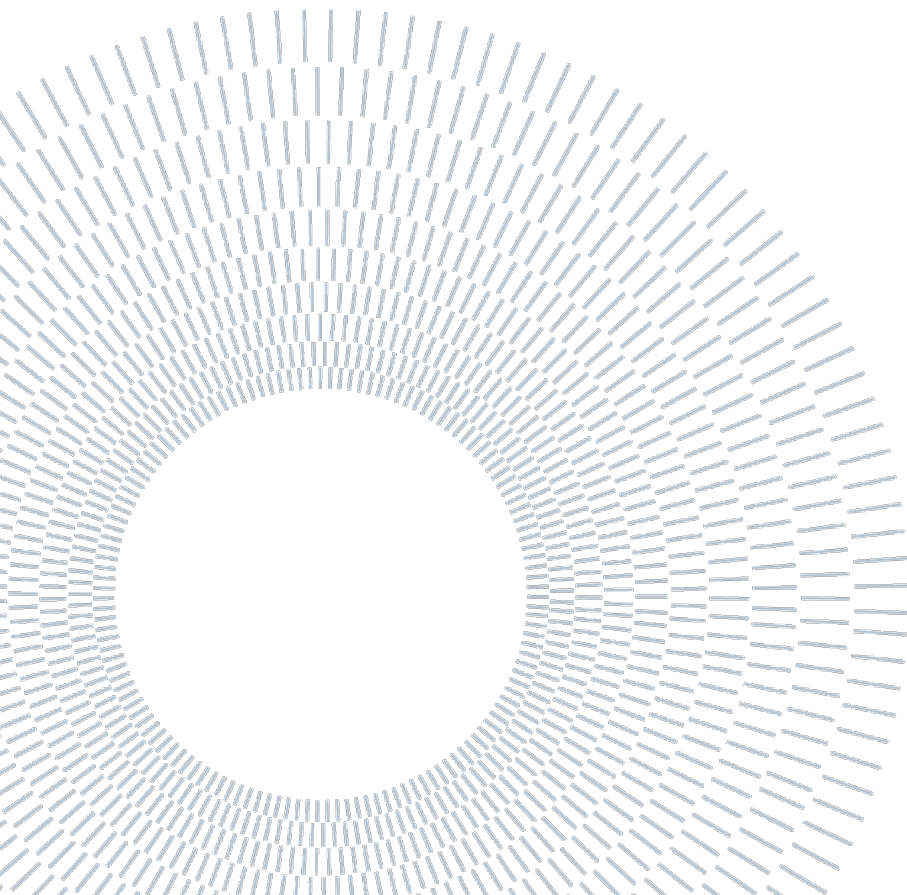
Keywords: Bevel Gears, Hypoid Gears, Gear Set Misalignments, Loaded Tooth Contact Analysis (LTCA), Contact Pattern, Failure Modes, Gear Testing, FZG Test Rig, Torque Measurement, Calibration, Measurement Uncertainty, GUM, Pitting

Abstract in lingua italiana

Grazie alla loro capacità di trasmettere potenza tra assi rotanti perpendicolari tra di loro, così come grazie al loro relativamente facile e consolidato metodo produttivo, le coppie coniche hanno un ampio spettro di applicazione. Infatti, è possibile trovare un loro uso all'interno di tutti i settori industriali. Vi è quindi una necessità industriale di ricerca scientifica su tutti i loro aspetti, uno di questi è lo studio dell'effetto che di microgeometria, trattamenti e materiali hanno sulla loro capacità resistenziale rispetto ai vari meccanismi di cedimento a cui sono soggetti gli ingranaggi (es. macro e micro pitting, fatica flessionale piede dente, grippaggio, etc.). Tipicamente, questo tipo di ricerca viene effettuata su banchi prova ad ingranaggi, principalmente con un principio di funzionamento basato sul ricircolo meccanico della potenza. Purtroppo, negli ultimi anni, si è osservato un aumento della dispersione dei dati ottenuti su questa tipologia di banchi prova.

Facendo riferimento al banco prova presente presso il Forschungsstelle für Zahnräder und Getriebesysteme (FZG, Gear Research Center) e al meccanismo di cedimento del pitting, questa tesi si focalizza sulla definizione e sulla valutazione di tutti quei fattori che possono influenzare tale dispersione.

Parole chiave: Ingranaggi conici, Ingranaggi ipoidi, Mancanze nell'allineamento degli ingranaggi, Analisi del contatto del dente caricato (LTCA), Schema di contatto, Modi di guasto, Test degli ingranaggi, Banco di prova FZG, Misurazione della coppia, Calibrazione, Incertezza di misura, GUM, Pitting



Contents

Abstract	i
Abstract in lingua italiana	iii
Introduction	1
1. Literature Review and Theoretical Background	4
1.1 Bevel & Hypoid Gear Design, Classifications	5
1.1.1 Classification of Bevel Gears.....	5
1.2 Bevel & Hypoid Gear Design.....	8
1.2.1 Definitions for Bevel & Hypoid Gears.....	8
1.2.2 Definition of Gear Dimensions	8
1.2.3 Hypoid Gear Geometry	12
1.3 Failure modes on Bevel and Hypoid Gears: Pitting and Micropitting	13
1.3.1 Pitting	13
1.3.2 Micropitting.....	16
1.3.3 Effects of Micropitting on Contact Pattern	17
1.4 Calculation Methods of Load carrying capacity of Bevel & Hypoid Gears	19
1.5 Experimental Investigations in Gear Research.....	26
1.6 Strength Rating Methods and Review for Bevel and Hypoid Gears	29
1.6.1 Rating Standards and Methods	31
2. Back-to-Back Test Rig at Gear Research Center (FZG)	33
2.1 Introduction to FZG Back-to-Back Test Rig for Bevel and Hypoid Gears.....	34
3. Experimental Investigations at Back-To-Back Hypoid Test Rig	40
3.1 Theoretical Suggestions Regarding the Influence of Micropitting on Contact Pattern..	40
3.2 Description of the Fatigue Test.....	40
3.3 Experimental Test Results	42
4. Simulation Modelling of FZG Hypoid Test Rig	46
4.1 General Definition of Modelling Principles of SMT MASTA Software.....	47
4.2 Simulation Model of The FZG Hypoid Test Rig.....	51
4.3 Simulation Results of Model.....	58

5. Loaded Tooth Contact Analysis.....	64
5.1 Introduction to BECAL (BEvel gear CALculation) Software	64
5.2 Processing of Simulation Results on BECAL LTCA Analysis.....	66
5.3 LTCA Results	68
5.3.1 The Effect of Variation of Preloading on Pinion Shaft Bearings on Contact Pattern.....	72
5.3.2 The Effect of Slight Torque Fluctuation on Contact Pattern.....	73
6. Sensitivity Analysis of the Torque Measurement System of the FZG Hypoid Test Rig	76
6.1 State of Art of the Calibration Procedure	77
6.1.1 Definition of Calibration.....	77
6.1.2 General Information on Torque Measurement Instrument Calibration.....	77
6.1.3 Preparations	78
6.1.4 Performing the Calibration	78
6.1.5 Steps for Evaluation	80
6.1.6 Measurement Uncertainty Analysis and Error Estimation	84
6.1.7 Uncertainty of Measurement According to GUM	85
6.1.8 Uncertainty of Calibration According to DIN-51309.....	89
6.2 Calibration of the Torque Measuring System on the FZG Hypoid Test Rig.....	92
6.2.1 Introduction of Lever-Mass System.....	92
6.2.2 Preparation of Calibration and Calibration Setup.....	93
6.2.3 Carrying out the Calibration.....	96
6.2.4 Data Collection.....	99
6.3 Calibration Test Results & Sensitivity Analysis.....	100
7. Conclusion	105
Bibliography.....	106
A. Appendix A.....	111
B. Appendix B.....	117
C. Appendix C.....	121
List of Figures.....	125
List of Tables	128
List of Symbols	130
Acknowledgements.....	134

Introduction

Nowadays, significant improvements in drive technology, have lead to remarkable developments in machines in several industries based on the principle of mechanical power transmission. For the proper functioning of such developed machines, it is highly essential to clearly determine the mechanical strength properties of all installed mechanical components. Therefore, a variety of methods have been developed in terms of analytical, numerical, and mainly experimental ways in order to properly identify relevant characteristics of materials used in power transmission applications. For the reliability of results achieved, especially in experimental testing, it is highly important to precisely determine the test outputs without a considerable dispersion.

The work carried out in this thesis, mainly considers a particular Back-to-Back Hypoid Test Rig at the Gear Research Center (FZG) at the Institute of Machine Elements of the Technical University of Munich, which is used for the experimental investigation of gear failure, providing support to the analytically developed calculation methods. As a scope of the thesis, it is aimed defining and evaluating possible causes and influences on the scatter of the experimental results at the test rig.

Overall, during the assembly process of gear set, pinion and wheel are precisely installed so that contact pattern is accumulated on the center of the flank surface for proper distribution of load. After initial pre-running at low torque level, contact pattern still emerges correctly in the center of flank surfaces. However, following a large number of load cycles, pitting failure occurs not in the center, but in any shifted position on the flank surface. Therefore, this problem was intensively investigated within a six-month`s period by progressively follow these steps:

Exploring Existing Knowledge: Examining what is known currently about bevel and hypoid gears serves as the starting point of the project. Understanding the different aspects of these mechanical components is crucial due to their common usage in many industrial applications. The classification of gears, design techniques, typical failure mechanisms, such as pitting, and specialized analyses for bevel and hypoid gears are covered in this section. It is also mentioned about the need for flexible standards that take these gears' particular characteristics into account. Additionally, a new method for calculating pitting that takes slip and hypoid effects into account, is presented. This section emphasizes the significance of integrating established values with novel ideas.

Practical Testing and Analysis: Following the literature review, the test rig was explored in detail. This system, which is housed at the Chair of Machine Elements at TUM, is essential for assessing gears in all aspects, including the determination of load carrying capacity. Its detailed description with working principles, components, and configuration was presented, and these details were greatly considered for the objective of the project. Following the description of the all steps of the entire testing procedure, experimental results were presented and discussed, together with consideration of related literature.

Modeling and Analysis Studies: The current test rig was modelled on the SMT MASTA which is a tool for analysis and optimization of gear systems, and drivelines from several aspects. As a result of the proper modelling of test rig, the relevant output parameters were achieved, and their changing trends were analyzed under the impact of different factors. Moreover, these outputs were intended to be used in the subsequent steps in LTCA analyses. The analysis results were compared with those of real experiments in order to investigate the influences of the considered factors on the scatter of the experimental results.

Precision in Torque Measurement: Checking precision of the torque measurement system and the resulting uncertainties are the main topics of the last section. After going over what calibration entails and the regulations that govern torque measurement calibration, the significance of appropriate setup and preparation for precise calibration was explained. Following that, how the calibration test was carried out, how measured data was processed, and how obtained results were evaluated, were revealed.

Finally, this master`s thesis concludes all comprehensive analysis and interpretation of all the research findings.

1. Literature Review and Theoretical Background

The literature review, which is frequently referred to as the state of the art, forms a crucial cornerstone in understanding the current developments and body of knowledge in a particular field of study. This section of the thesis is devoted to providing a thorough overview of current knowledge on bevel and hypoid gear classification, design, particular failure modes, experimental investigations, and load carrying capacity calculation specifically tailored to these gear configurations, within the context of the provided sections.

This section functions as a conceptual framework, offering an in depth investigation of the complex environment around bevel and hypoid gears. Its primary objective is to synthesize the body of knowledge from prior academic endeavors, demonstrate the limits of knowledge, and lay the groundwork for additional research. The literature review attempts to establish the contextual backdrop against which the following research develops by tracing the outlines of scholarly discourse. At the same time, this section explores several design techniques and classifications that have evolved over time in the field of bevel and hypoid gear design. It aims to capture the development of taxonomy and design principles, giving scholars a comprehensive viewpoint that guides their own study.

The topic of failure modes, particularly pitting and micropitting, dives into the weaknesses that can compromise the integrity of gear. The literature review analyzes the root causes and transmission processes of these modes to reveal insights essential for developing preventative measures as well as areas of concern.

By analyzing the procedures and results of earlier experiments, the part emphasizes the empirical aspect of research in the field of experimental investigations.

The explanation of calculation methods for load carrying capacity outlines analytical and computational frameworks for evaluating gear operation under different load conditions. This aspect is crucial because it gives engineers the tools, they need to improve gear designs for robustness in various operational scenarios.

1.1 Bevel & Hypoid Gear Design, Classifications

The content to be discussed in this section (1) has been derived from the book "Bevel Gear Fundamentals and Applications" by Jan Klingelnberg [21], as well as various ISO standards [12, 13, 14], to provide a comprehensive and academically grounded presentation.

1.1.1 Classification of Bevel Gears

Various characteristics that characterize bevel gears can be used to categorize them. These attributes include the order of the tooth depth along the face width, the configuration of the tooth trace (curved or straight), the specific contour of the tooth trace curve, pinion axial offset, the type of indexing operation (continuous or single indexing), the cutting technique (generation or plunge cut), and the manufacturing strategy. Each of these characteristics contributes to the distinctive classification and design of bevel gears, enabling a thorough grasp of their unique features and uses [21].

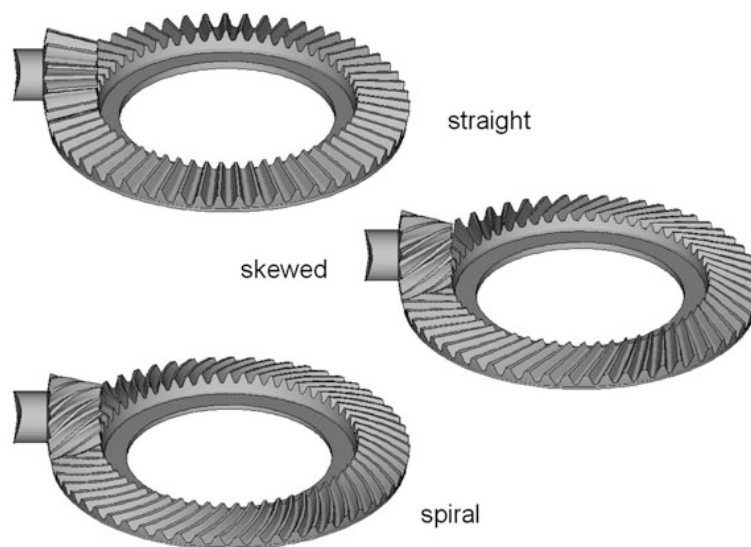


Figure 1.1.1: Straight, skew and spiral bevel gears [21]

The classification of bevel gears is governed by a variety of factors. For instance, the fundamental crown gear is followed by the kind and arrangement of the teeth. Figure 1.1.1 illustrates the tooth trace-based classification of bevel gears.

An interesting subgroup of spiral bevel gears further divides according to the shape of their tooth traces, which can include the following forms:

- An involute, an elongated epicycloid, a circular arc, and an elongated hypocycloid

In addition, the hypoid offset of bevel gears represents a distinctive categorization axis. They can be categorized based on their hypoid offset. Conversely, bevel gears with pinion offset, sometimes referred to as hypoid gears, have crossing axes whereas bevel gears without a pinion offset have intersecting axes.

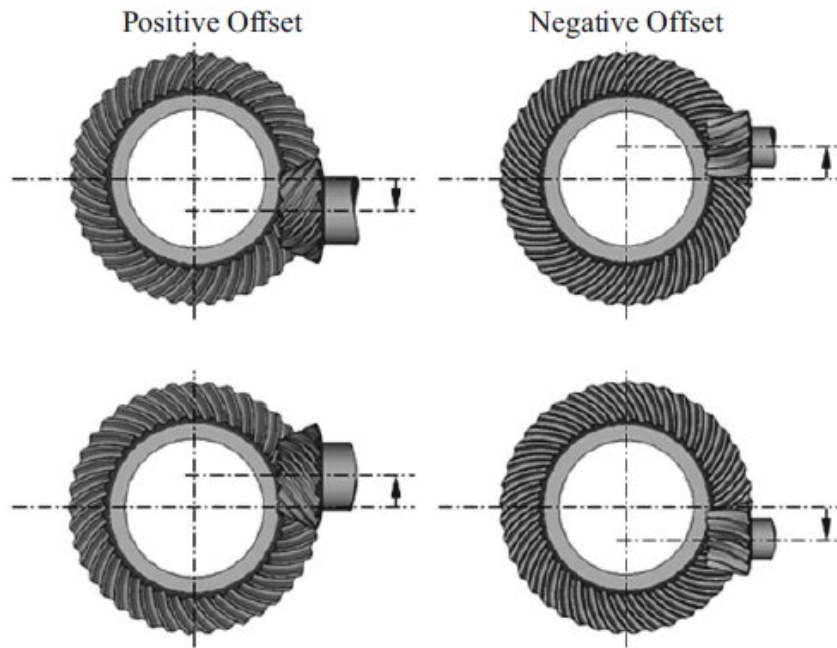


Figure 1.1.2: Hypoid Offset [21]

Based on the type of offset, a greater separation develops within this domain:

Positive Offset: The pinion axis moves in the spiral angle of the wheel's axis direction. The average helix angle of the pinion is greater than that of the wheel. The diameter of the pinion becomes larger in comparison to an offset-less gear set.

Negative Offset: The pinion axis moves in the opposite direction of the spiral angle of the wheel. In comparison to the wheel, the pinion's typical helix angle is less. Compared to an offset-less gear set, the pinion's diameter decreases.

These classifications, as explained above, serve as crucial criteria for classifying and comprehending bevel gears. The complex interaction between tooth trace and offset designs greatly enhances the adaptability and functional variation of these gear systems.

Also, when created using metal-cutting procedures, spiral bevel gears can either be constructed using single or continuous indexing techniques, which affects the geometry of the tooth trace. When one tooth slot is cut in single indexing or face milling, the following slot is cut after rotating the workpiece by one pitch, producing tooth traces that resemble circular arcs. In continuous indexing or face hobbing, the cutter and gear rotation are coordinated so that blade groups travel through particular tooth slots in a predetermined order, resulting in tooth traces that resemble extended epicycloids. Through producing motion, spiral bevel gears can have curved tooth profiles on both the pinion and the wheel. An alternate non-generated method entails shaping the wheel's tooth gaps using plunge cuts and producing the pinion. When transmission ratios are higher, this technique works well. The manufacturing process adopted, which affects the tooth flank and root features as well as the previously mentioned categorization criteria, shapes the tooth geometry in spiral bevel gears [21].

Manufacturing method	Indexing method	Tooth trace curve	Tooth depth	Slot width ^a		Profile crowning	Lengthwise crowning
				pinion	wheel		
Zyklo-Palloid [®] / Zyklomet [®]	Continuous	Epicycloid	Constant	Variable	Variable	In the tool	Radius difference
Palloid [®]	Continuous	Involute	Constant	Constant	Constant	- ^b	In the tool
N-method	Continuous	Epicycloid	Constant	Variable	Variable	In the tool	Lead angle difference
Spiroflex/Spirac [®]	Continuous	Epicycloid	Constant	Variable	Variable	In the tool	Cutter tilt
TRI-AC [®] /PENTAC [®] -FH	Continuous	Epicycloid	Constant	Variable	Variable	In the tool	Cutter tilt
Kurvex	Single	Circular arc	Constant	Variable	Variable	- ^c	Radius difference
Arcoid	Single	Circular arc	Variable	Variable	Variable/ constant	Machine kinematics	Cutter tilt
5-cut	Single	Circular arc	Variable	Variable	Constant	Machine kinematics	Radius difference
Completing	Single	Circular arc	Variable	Constant	Constant	Machine kinematics	Cutter tilt
Wiener 2-Spur	Single	Circular arc	Constant	Variable	Variable	In the tool	Radius difference
Wiener 1-Spur	Single	Circular arc	Constant	Variable	Constant	In the tool	Radius difference
Semi-Completing	Single	Circular arc	Constant	Variable	Variable	In the tool	Radius difference

^aAt root cone in normal section

^bTool with tip relief

^cTool with protuberance

Table 1.1.1: Overview of the main manufacturing techniques for spiral bevel gears [21]

Table 1.1.1 summarizes the production methods. This section will not go further into the details of production techniques.

1.2 Bevel & Hypoid Gear Design

1.2.1 Definitions for Bevel & Hypoid Gears

Non-offset bevel gear pairs exhibit a configuration where two cones interlock and roll against one another without sliding, resembling how a pinion and a wheel interact. These cones, also known as "basic bodies," have axis intersections where their apices meet, forming continuous contact along a common generatrix. The axes of the pitch cones ($\delta_{1,2}$) in the bevel gear pair define the angle, also known as the shaft angle Σ . By using a made-up virtual rack, the idea of creating a cylindrical gear set is conceptually clarified. Accordingly, this comparison becomes a practically flat crown gear when applied to bevel gears. The virtual crown gear uses a pitch angle of $\delta_p=90^\circ$ degrees to help visualize the geometric interaction between the bevel gear and the gear [21].



Figure 1.2.1: Bevel gear pair

1.2.2 Definition of Gear Dimensions

No.	Designation	No.	Designation
1	Back angle	13	Mounting distance, t_{B1} , t_{B2}
2	Back cone angle	14	Outer cone distance, R_e
3	Back cone distance	15	Outside diameter, d_{ae1} , d_{ae2}
4	Clearance, c	16	Pitch angle, δ_1 , δ_2
5	Crown point	17	Pitch cone apex
6	Crown to back	18	Crown to crossing point, t_{x01} , t_{x02}
7	Dedendum angle, θ_{r1} , θ_{r2}	19	Outer pitch diameter, d_{e1} , d_{e2}
8	Face angle, δ_{a1} , δ_{a2}	20	Root angle, δ_{r1} , δ_{r2}
9	Face width, b	21	Shaft angle, Σ
10	Front angle	22	Equivalent pitch radius
11	Mean cone distance, R_m	23	Mean pitch diameter, d_{m1} , d_{m2}
12	Mean point		

Table 1.2.1: Bevel Gear Designations for Fig 1.2.2 [21]

Non-offset bevel gear designs are listed in Table 1.2.1, and the gear sizes are shown in an axial cross-section in Figure 1.2.2.

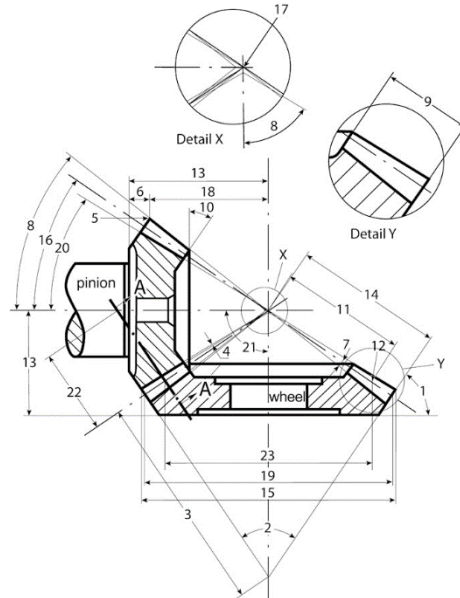


Figure 1.2.2 : Bevel gear geometry definition in the axial section [13]

A transverse section on bevel gears is shown in Figure 1.2.3's Section A-A. This area effectively mirrors the complementary cone at the place of interest because it is always positioned perpendicular to the pitch cone. Figure 1.2.3 unfolds the complementary cone with the mean point onto a hypothetical plane for better viewing. The equivalent pitch diameter produced by this transformation is given in Table 1.2.3 along with its related dimensions ($d_v = d_m / \cos \delta$).

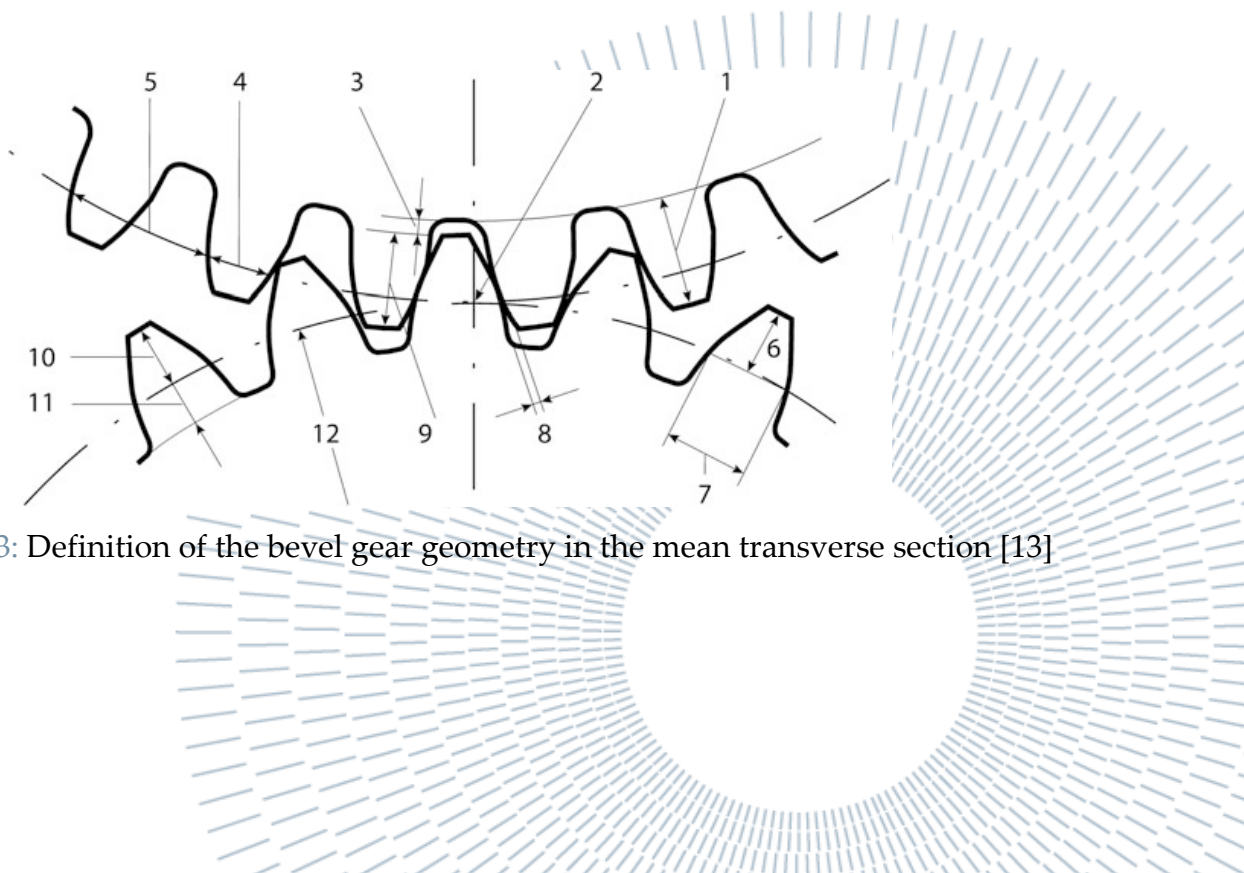


Figure 1.2.3: Definition of the bevel gear geometry in the mean transverse section [13]

No.	Designation	No.	Designation
1	(Mean) whole depth, h_m	7	Tooth thickness, s_{mc} (mean chordal)
2	Pitch point	8	Backlash
3	Clearance, c	9	(Mean) working depth, h_{mw}
4	Circular thickness, s_t	10	Addendum, h_{am}
5	Circular pitch	11	Dedendum, h_{fm}
6	Addendum h_{amc} (mean chordal)	12	Equivalent pitch radius

Table 1.2.2: Bevel Gear Designations for Fig 1.2.3 [21]

Furthermore, Figure 1.2.4 shows the essential characteristics of hypoid gears, and Table 1.2.3 provides a detailed explanation.

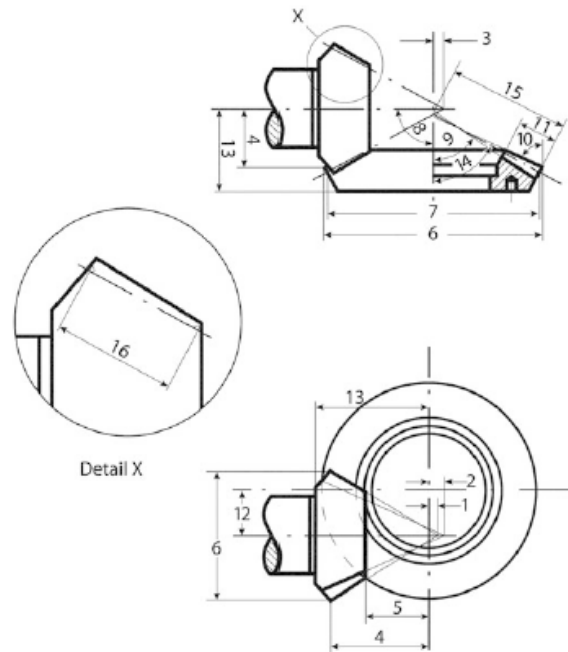


Figure 1.2.4: Hypoid gear geometry definition [13]

No.	Designation	No.	Designation
1	Face apex beyond crossing point, t_{zF1}	9	Root angle, δ_{f1} , δ_{f2}
2	Root apex beyond crossing point, t_{zR1}	10	Face angle, δ_{a1} , δ_{a2}
3	Pitch apex beyond crossing point, t_{z1}	11	Face width of the wheel, b_2
4	Crown to crossing point, t_{xO1} , t_{xO2}	12	Hypoid offset, a
5	Front crown to crossing point, t_{xI1}	13	Mounting distance, t_{B1} , t_{B2}
6	Outside diameter, d_{ac1} , d_{ac2}	14	Pitch angle of the wheel, δ_2
7	Outer pitch diameter, d_{c1} , d_{c2}	15	Outer cone distance, R_c
8	Shaft angle, Σ	16	Face width of the pinion, b_1

Table 1.2.3: Bevel Gear Designations for Figure 1.2.5 [21]

When defining the spiral hand of a bevel gear, one looks from the pitch cone apex toward a tooth that is at the 12 o'clock position. If the tooth curves to the right when viewed from the front to the back, the gear has a right hand of spirals, and vice versa.

On right-handed bevel gears, the concave flank is often on the right side of the tooth, and on left-handed bevel gears, on the left side of the tooth (see Fig. 1.2.5). When there is an inverse spiral, however, the situation is inverted [21].

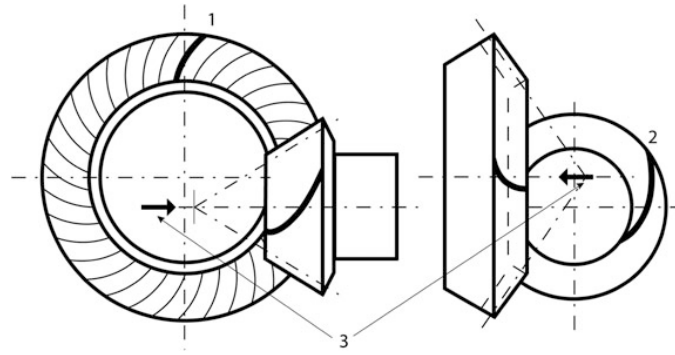


Figure 1.2.5: Definition of the spiral hand. 1 right hand, 2 left hand, 3 view from the pitch cone apex [21]

If spiral bevel gears with a positive hypoid offset cause the concave tooth flank of the pinion to drive the convex tooth flank of the wheel, load circumstances are advantageous. The flank of the pinion tooth was chosen for the drive mode, or when the engine is driving the vehicle forward, due to its use in car axle drives.

Inversely, when in coast mode, or when the moving vehicle is stopped by the engine, the convex tooth flank of the pinion is loaded. The following designations are given to the tooth flanks on all spiral bevel gear sets, whether they have hypoid offset or not, as a result of the preceding considerations:

Pinion	concave flank = drive flank
	convex flank = coast flank
Wheel	convex flank = drive flank
	concave flank = coast flank

Table 1.2.4: Coast and Drive Tooth Flanks [21]

Bevel gears use the same idea of contact ratio as cylindrical gears, which represents the typical number of engaged teeth. Profile contact and overlap combine to form the total contact portion of this ratio. The way they interact is seen in Figure 1.2.6. Only if the tooth flanks are conjugate does the total ratio hold true. Total ratio is impacted by crowning, producing a somewhat lower number. In calculations, the total ratio is frequently approximated as the square root of the sums of the overlap and profile ratios.

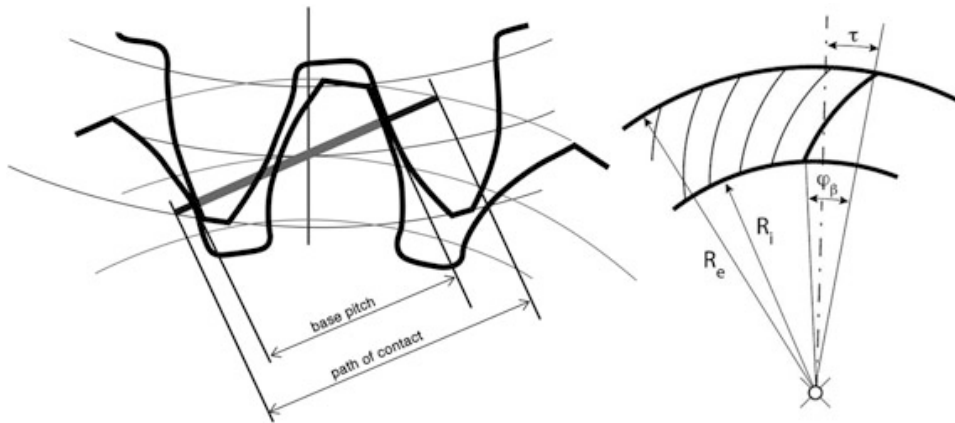


Figure 1.2.6: Contact Ratio [21]

Tooth contact analysis provides information on the efficient total contact ratio while enhancing precision. It depends on elements like crowning and dimension changes brought on by loads. For precise total ratio calculation, analytical approaches, such as FEM and BEM, take into account difficulties such profile flattening, tooth deflection, and axis changes.

1.2.3 Hypoid Gear Geometry

Bevel gears are an extension of this idea, whereas hypoid gears use one-sheet hyperboloids as their "basic bodies." These hyperboloids engage along a straight helix axis, unlike non-offset gears, engaging in helical motion and simultaneous sliding. Due to crowning in bevel gear teeth, economic manufacture necessitates approaching helical pitch surfaces with conical surfaces. The framework for hypoid gears, where the pinion and wheel pitch cones share a contact plane, is formed by the mean point P exactly satisfying helical motion criteria. Here, the gear axes cross at a distance rather than intersecting. Gear ratio, shaft angle, offset, and tool radius are taken into account when calculating pitch angles iteratively. The mean point P is the name given to this calculating point.

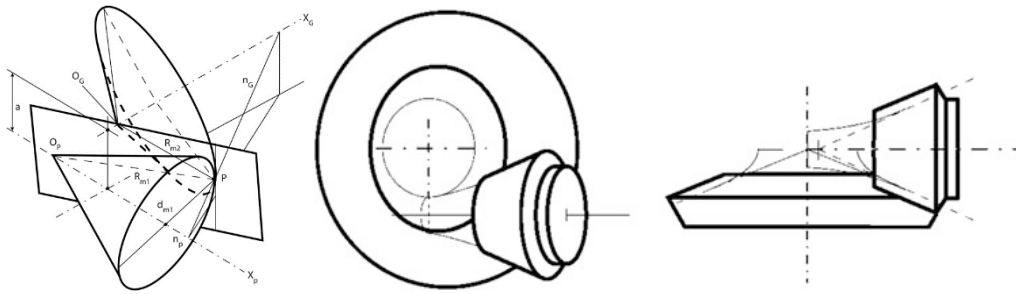


Figure 1.2.7: Schematic elements of a hypoid gear set [13]

Optimizing bevel gears involves choosing design pressure angles, which can differ on each side and become important for balanced sliding in hypoid gears. Unlike simple cylindrical gears, possible pressure angles can go beyond 0 degrees to a limit pressure angle, influenced by factors like hypoid offset and tool size. Sometimes, specific designs might limit pressure angle to zero. The influence factor f , or limit pressure angle helps handle practical tool angle calculations, compensating in different situations. These factors also affect the flank angle in gear design.

1.3 Failure modes on Bevel and Hypoid Gears: Pitting and Micropitting

1.3.1 Pitting

Macropitting or pitting as it's referred to in the thesis is a fatigue failure condition in active region of the tooth flank. Shell-shaped craters are created at the surface when the Hertzian stress is greater than the material strength. These pits continue to increase and finally cause a gear to fail completely as a result of a series of localized failures [21].



Figure 1.3.1: Pitting on the Flank Surface [21]

Particles break out of the meshing flanks when the surface durability limits are reached, "leaving pits" in the flank. The size and number of these pits that can be tolerated vary widely within broad bounds that are heavily influenced by the application field. While no pitting is acceptable in some domains, significant pitting is acceptable in others. Pitting that is linear or progressive is often seen as inappropriate because it increases the total area of pits [21].

However, there is a possibility that initial pitting increases the effective tooth bearing surface, and that later on the rate of pit creation declines (degressive pitting) or stops (arrested pitting), at which point it may be considered acceptable. Nevertheless, the following clause shall be controlling in cases of disagreement regarding the acceptableness of pitting [21].

Pitting results in the creation of pits that grow linearly or gradually over time while still meeting service requirements is prohibited. The assessment of damage must take into account every tooth flank's active area. In unhardened tooth flanks, the quantity and size of newly formed pits must be taken into account. On one or some of the flanks of the surface-hardened gear tooth, pits typically occur. In these cases, evaluation must focus on the flanks that are actually pitted. If a quantitative analysis is required, teeth thought to be particularly at risk should be marked for critical examination. In exceptional circumstances, it is possible that a preliminary evaluation could be made using the total amount of wear debris [21].

However, in critical situations, it is necessary to check the flanks minimum three times. Nevertheless, the examination shouldn't be performed for the first time until at least 10^6 cycles have passed under load. After a certain amount of service, further tests should be conducted based on the outcomes of earlier ones. Pitting must not be tolerated if the deterioration it causes puts human life in danger or creates the possibility of other serious effects [21].

Because of the effects of stress concentration, a 1 mm-diameter pit close to the fillet of a through- or case-hardened gear tooth may start a crack that could result in tooth breakage; for this reason, such a pit is forbidden (for instance, in aerospace transmissions) [21].

Regarding turbine gears, the same factors need to be taken into account. Neither excessively severe wear nor pitting should be regarded as acceptable during the extended life (10^{10} to 10^{11} cycles) required of these gears as such degradation could result in intolerable vibrations and high dynamic loads. Only a low probability of failure shall be accepted, hence the computation should consider appropriately generous safety measures. For certain industrial gears with large teeth that operate at slow speed and are constructed of low-hardness steel, such as module 25, with which

the rated power may be securely transmitted for 10 to 20 years, pitting on the operating flanks may be permitted. A single pit may have a diameter of up to 20 mm and a depth of 0.8 mm.

During the first two or three years of use, so-called "destructive pitting" slows down. These circumstances are observed with that the tooth flanks smooth out and harden to the point where the surface Brinell hardness value rises by at least 50%. In these circumstances, comparably low safety factors (in some cases, less than 1) can be selected, increasing the probability of tooth surface injury. However, it is important to choose a high safety factor to prevent tooth breakage [13, 14, 21].

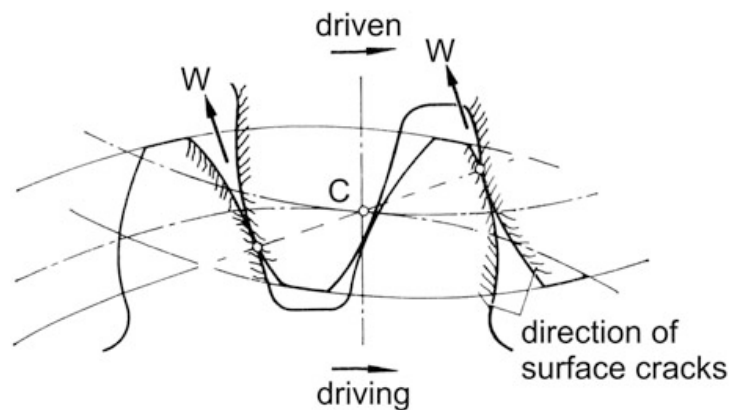


Figure 1.3.2: Crack directions, rolling, and sliding on a gear tooth flank [21]

It becomes crucial to reduce the stress brought on by Hertzian contact in order to increase the ability to endure pitting. Larger radial curve curvatures can be used to reduce this. This is then achieved by using smaller gear modules, which result in higher contact ratios. Other tactics include choosing greater pressure angles and using a positive pinion profile shift. The contact ratio can also be increased with a larger offset, which necessitates a more prominent spiral angle for hypoid pinions [21].

Though a higher contact ratio is advantageous, it's important to remember that a larger offset introduces increased sliding velocity due to longitudinal sliding. Therefore, surface stress increases significantly. As a result, the possible negative effects of increased sliding velocity tend to balance out the positive effects of a higher contact ratio. It is crucial to calculate an ideal offset that maximizes resistance to pitting in light of these parameters. The use of case-hardened steel, maintaining proper surface hardness and quality, and using lubricants with greater viscosities combined with efficient additives are all possible options when it comes to strength considerations [21].

Finally, selecting the right lubricant can successfully reduce the coefficient of friction within a gear system, improving the gear setup's resistance to loads brought on by pitting. The FZG pitting test is an alternative way to assess quality of a lubricant in terms of pitting potential [21].

1.3.2 Micropitting

Micropitting is a form of failure that happens when high-stress regions on the surface of a tooth coincide with insufficient lubricating film thickness. As a result, matte gray areas with little cracks and fractures start to form. These fissures eventually grow into tiny craters called "micro" pits, which essentially take material from the surface as a result of wear and tear. In addition to changing the geometry of the tooth flanks and interfering with stress distribution, this process also generates noise, increases dynamic forces, and may have an impact on the capacity for pitting [21].

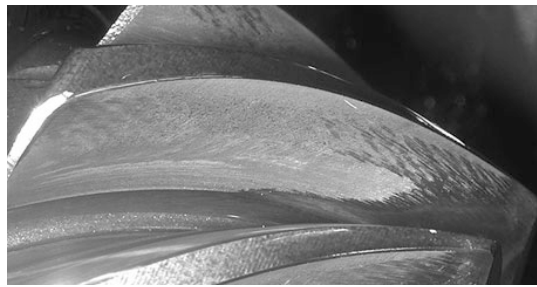


Figure 1.3.3: Micropitting on the Flank Surface [21]

Surface and lubrication properties are the main determinants of micropitting. The ratio between the minimum lubrication film thickness to the typical roughness of tooth flank is used to calculate the relative lubricant film thickness, which serves as the failure criterion. Then, this ratio is contrasted with an acceptable value obtained from the FZG micropitting test.

In contrast to contact stress, speed and lubricant viscosity are the main determinants of lubricant film thickness. While sliding velocity prevents film development, the combined velocities aid in it. The pinion's minor profile shifts and low hypoid offset, which produce less frictional heat and lead to higher viscosity and a thicker lubrication film, are favorable for the creation of the lubricant film.

A low coefficient of friction lubricant has to be used to increase micropitting load capability. Additionally, lubricant additives, especially those based on phosphorus sulfide, have a significant effect on reducing micropitting. Processes like hard finishing or running-in techniques that smooth the active tooth flank surfaces have a beneficial

impact on micropitting resistance because smoother flank surfaces are more resistant to micropitting [21].

Apart from pitting and micropitting, there are other gear failure modes, like flank breakage, tooth root breakage, ridging, rippling, and scuffing. However, it's important to note that these specific failure modes are not within the scope of the current research and have not been elaborated upon in this section.

1.3.3 Effects of Micropitting on Contact Pattern

Under this related title, it has been tried to put forward a general comment by making use of Ivan Boiadjev's doctoral thesis [2] and other theses made at Gear Research Center FZG. The importance of micropitting in conjunction with gray spots has consistently been highlighted in research on gear mechanisms. It was mentioned as a gray area in previous sections. The "Loss of Drive" failure criterion has historically been the main criterion used to evaluate micropitting in bevel and hypoid gears, as shown in studies by FZG/WIRTH [36], FZG/VOLLHÜTER [33], and FZG/THOMAS [31]. This method involves stopping the test when the test equipment shows significant damage, makes further investigation impossible, or produces conflicting results. As stated by HSEL/GOEBBELET [11], the micropitting criterion for spur gears is based on "1% micropitting area relative to the flank area of all teeth" or "4% of a single tooth's surface". FZG/WIRTH [36] also examined the transferability of the "Loss of Drive" criterion from spur to bevel gears and noted that the failure criterion for spur gears cannot be meaningfully applied to hypoid gears due to combined micropitting and pitting, noting that micropitting and gray spot formation often coexist in hypoid gears. It was also shown that the severity of gray spots significantly influences the onset of micropitting damage.

The number of gray spots has a significant impact on the development of micropitting damage. Over time, the depressions brought on by gray spots change how local stress is distributed on the flank, having a significant impact on micropitting susceptibility. Gray spots either cause the stagnation of existing micropitting or the emergence of new ones in flank regions that were not initially under critical stress, or they can prevent micropitting damage by reducing local stress. This complex interplay of damages suggests that it is increasingly difficult to make accurate predictions about micropitting susceptibility based only on initial stress distribution. FZG/WIRTH [36] evaluates all tests in relation to "Loss of Drive" to take into account the mechanism of relief in severely stressed areas. This method, however, yields systematic irregularities and mistakes, especially for gears with various degrees of gray spots. Furthermore, because transmissions in real-world applications are frequently replaced when minor

micropitting damage occurs, the "Loss of Drive" criterion tends to overestimate the durability of gears.

Through an extended calculation approach, the impact of gray spots on micropitting susceptibility is further quantified. This entails using a tooth contact analysis tool to examine pressure distributions in appropriate gear configurations and taking into account locally important factors using the BECAL / HYBOID calculation program. Calculations are done using initial data and data that represents gray-spotted conditions for a variety of runtimes. Gray spots are known to alter pressure distributions, which are observed to change contact patterns. The endurance of gears against micropitting is subsequently impacted by this. The study also introduces an enhanced micropitting failure criterion that takes into account the formation of gray spots. The criterion modifies the critical threshold for micropitting susceptibility as the severity of the gray spots increases by computing the allowable micropitting area based on the level of gray spots. The suggested method enables a possible evaluation of micropitting susceptibility and offers insightful information for gear design and durability testing [2].

Furthermore, considering the following study: "New calculation method of the micropitting load carrying capacity of bevel and hypoid gears" by J. Pellkofer, M. Hein, T. Reimann, M. Hombauer, and K. Stahl [26], the content takes into account this new calculation method for micropitting load carrying capacity. In the experimental studies, hypoid gear micropitting took place more quickly than it did on bevel gears under the same load. Also, the bevel gear variant only demonstrates micropitting in regions close to the dedendum flank area, whereas the hypoid gears demonstrate micropitting throughout the entire flank. For the test gear set with axial offset of 31.75 mm, pitting failures started to happen more quickly compared to the other hypoid test gear variations with a smaller axial offset. In contrast to the other testing variants with hypoid offset, it was apparent that the micropitting structure had changed [26].

The findings underline the need for more comprehensive failure criteria that consider the combined influence of gray spots, contact pattern shifts, and micropitting on gear durability, enabling improved gear design and more accurate durability assessments. In conclusion, the research on the effect of micropitting on contact patterns emphasizes the complex relationship between gray spot formation, shifting contact patterns, and micropitting damage.

The outputs of these studies made important contributions and inspirations to the current study on analyzing the effect of micropitting on shifting of contact pattern.

1.4 Calculation Methods of Load carrying capacity of Bevel & Hypoid Gears

ISO 10300-2:2014 [12] is one of the commonly used standards to assess the safety of bevel and hypoid gears against pitting. The relevant section of the ISO standard contains all the factors on surface durability that can be quantified and gives the fundamental formulas to be used in calculating the surface load capacity of not only straight and helical gears, but also zero and spiral bevel gears, as well as hypoid gears. Although there are many calculation methodologies other than this ISO standard, the programs and studies used in the following sections of the thesis refer to the methodologies and formulas in the ISO standard [12]. Finally, this ISO standard is updated according to the requirements, but the above-mentioned version has been examined in this study.

To start explaining the content of the standard: If there is always enough lubricant in the mesh, this section of ISO 10300 is applicable to bevel gears that are lubricated with oil. The evaluation of further types of gear tooth surface damage, such as plastic yielding, scuffing, scratching or any other type not defined, is not directly applicable to the formulas in this section of ISO 10300. The formulas in this section of ISO 10300 are limited to bevel gears with virtual cylindrical gears that have transverse contact ratios of $\varepsilon_{va} < 2$.

There are two different procedures given in this ISO standard. And the procedures named B1 and B2 are the two basic procedures for determining the surface durability of bevel and hypoid gears. Methods B1 and B2 use the same mathematical basis, but the calculation approach is different for each. Apart from these two methods, calculation with BECAL and similar programs can be recognized as Method A. There is also a less detailed method known as Method C. Lastly, Method A is the most detailed calculation method but is only available for experts with specific software. Method B1/B2 is the standard capable calculation method.

The ability of a gear tooth to withstand pitting should be tested using both approaches by comparing the following stress values:

The contact stress σ_H is expressed by the contact stress formula and is related to the of the tooth geometry, the precision with which it was manufactured, the stiffness of the bearings, gear blanks and housing, and the working torque.

Permissible contact stress σ_{HP} depending on the endurance limit for contact stress, $\sigma_{H,Lim}$ and the impact of the working circumstances under which the gears operate.

Based on the contact (Hertzian) stress, which distributes the load along the lines of contact, pitting resistance is calculated. This stress has to be calculated for the pinion

and wheel simultaneously, however for hypoid gears, the drive side flank and the coast side flank must be calculated individually.

$$\sigma_{H-B1} = \sigma_{H0-B1} \sqrt{K_A K_V K_{H\beta} K_{H\alpha}} \leq \sigma_{HP-B1} \quad (1.1)$$

K_A = Application Factor, The computation should employ the nominal tangential force and an application factor, K_A , if credible experiences, load spectra derived by practical measurement, or full system analyses, are not available. This application factor accounts for any dynamic loads that are delivered externally and are greater than the nominal operating pinion torque, T_1 . It should be taken into account that several prime movers produce temporarily peak torques that are significantly higher compared to those predicted by the nominal ratings of either the driven machinery or prime mover when establishing the application factor. System vibration, critical speed, acceleration torques, overspeed, abrupt changes in system operation, braking, and negative torques are just a few of the numerous potential sources of dynamic overload that should be considered.

K_V = The dynamic factor, K_V , accounts for other factors like design, manufacture, transmission error, dynamic response, and resonance in addition to the impact of gear tooth quality on speed and load. The dynamic factor is the product of the transmitted tangential tooth load divided by the transmitted tangential tooth load and connects the overall tooth load, which also includes internal dynamic effects, to the transmitted tangential tooth load. There are two groups of parameters for the internal dynamic load of the gear tooth: design and production.

$K_{H\beta}$ = Face load factors: In order to consider reflection of the non-uniformly distributed load along the face width, the face load factors, K_H and K_F change the rating equations for the gear flank and for the tooth root. The ratio of the highest load per unit face width to the average load per unit face width is known as K_H .

Accuracy of gear tooth manufacturing, tooth contact pattern, and alignment, spacing of the gears in their mountings, elastic deflections of the gear teeth, bearings, shafts, housings, and foundations, which support the gear unit, resulting from either internal or external gear loads, bearing clearances, and Hertzian contact deformation of the tooth surfaces are all factors that affect the amount of non-uniform load distribution.

$K_{H\alpha}$ = Transverse load factors: In the case of specific gear dimensions, the precision of the gear and the magnitude of the total tangential force determine how the total tangential force is distributed among various pairs of meshing teeth. The impact of the load distribution on the contact stress is considered by the factor K_H .

The nominal value of the contact stress can be illustrated by:

$$\sigma_{\text{HO-B1}} = \sqrt{\frac{F_n}{l_{\text{bm}} \rho_{\text{rel}}}} Z_{\text{M-B}} Z_{\text{LS}} Z_{\text{E}} Z_{\text{K}} \quad (1.2)$$

where F_n is the nominal normal force of the virtual cylindrical gear at mean point:

$$F_n = \frac{F_{\text{mt1}}}{\cos \alpha_n \cos \beta_{\text{m1}}} \quad (1.3)$$

As specified in the ISO standard [12];

Alpha can be α_{nD} (generated for drive side) or α_{nC} (generated pressure angle for coast side)

l_{bm} is defined as the distance along the contact line at the centre of the action zone.

ρ_{rel} is the relative curvature radius which is vertically acting to the contact line.

$Z_{\text{M-B}}$ is the mid-zone factor that considers how to convert the contact stress at the mean point to the contact stress at determinant position.

Z_{LS} is the load-sharing factor which considers the load sharing between at least two teeth.

Z_{E} is the elasticity factor that is used to add the effect of material's Elastic modulus and Poisson's ratio.

Z_{K} is the bevel gear factor which takes into account for the impact of the bevel gear geometry.

After contact stress was calculated as above, it has to be compared with permissible contact stress and has to be smaller than that: Permissible contact stress can be calculated as below:

$$\sigma_{\text{HP-B1}} = \sigma_{\text{H,lim}} Z_{\text{NT}} Z_{\text{X}} Z_{\text{L}} Z_{\text{V}} Z_{\text{R}} Z_{\text{W}} Z \quad (1.4)$$

As given in ISO standard [12];

$\sigma_{\text{H,lim}}$ is defined as the allowable stress, which is influenced by material properties, any possible heat treatment, surface properties and so on.

Z_{NT} is the life factor that represents the impact of how many cycles of working is required.

Z_X is the size factor that is provided by the module and accounts for the impact of tooth size.

Z_L, Z_v, Z_R are the lubricant film factors which considers how the gear is lubricated.

Z_W is the work hardening factor which is based on the hardening of a softer wheel when it is coupled with a pinion that has been surface-hardened.

Z_{Hyp} is the hypoid factor, which takes surface durability into account while considering the impact of longitudinal sliding.

If there is a variation on the values of the permissible contact stress for wheel and pinion, the estimated safety factor for contact stress must be verified independently for both:

$$S_{H-B1} = \frac{\sigma_{HP-B1}}{\sigma_{H-B1}} > S_{H,min} \quad (1.5)$$

Calculation of contact stress factors

Mid-zone factor, Z_{M-B} : The mid-zone factor, takes into account the variation in relative curvature radius between the critical point of the pinion's load application and the mean point. It can be calculated with the analytical formulas below:

$$Z_{M-B} = \frac{\tan \alpha_{vet}}{\sqrt{\left[\sqrt{\left(\frac{d_{va1}}{d_{vb1}}\right)^2 - 1 - F_1 \frac{\pi}{Z_{v1}}} \right] \cdot \left[\sqrt{\left(\frac{d_{va2}}{d_{vb2}}\right)^2 - 1 - F_2 \frac{\pi}{Z_{v2}}} \right]}} \quad (1.6)$$

where d_{vb1} and d_{vb2} are base circles of pinion and wheel; while tip circles are shown with d_{va1} and d_{va2} , with the respective order. F_1 and F_2 factors which depend on $\varepsilon_{v\beta}$, can be selected from the table below:

Parameters	F_1	F_2
$\varepsilon_{v\beta} = 0$	2	$2 (\varepsilon_{v\alpha} - 1)$
$0 < \varepsilon_{v\beta} < 1$	$2 + (\varepsilon_{v\alpha} - 2) \varepsilon_{v\beta}$	$2 \varepsilon_{v\alpha} - 2 + (2 - \varepsilon_{v\alpha}) \varepsilon_{v\beta}$
$\varepsilon_{v\beta} \geq 1$	$\varepsilon_{v\alpha}$	$\varepsilon_{v\alpha}$

Table 1.4.1: Factors for Z_{M-B} [12]

Load sharing factor: The sharing of load between minimum two pairs of teeth is taken into consideration by the Z_{LS} load sharing factor. This means that this component establishes the greatest amount of the entire load that can have an impact on a single tooth. It is assumed that each contact line's load distribution in the zone of action is elliptical. When all contact lines are concurrently in mesh, the area, A , of each semi-ellipse indicates the load on that particular contact line, and the overall area over all contact lines represents the load on the entire gear set.

$$Z_{LS} = \sqrt{\frac{A_m^*}{A_t^* + A_m^* + A_r^*}} \quad (1.7)$$

A_t^* = is the region above the contact line of the tip,

A_m^* = is the region above the middle contact line

A_r^* = is the region above the root contact line

The detailed explanation how to calculate these areas can be found in the relevant ISO standard [12].

Bevel gear factor: The empirical factor Z_K explains the variations between bevel and cylindrical gears in a way that is consistent with actual experience. Bevel gears can be rated using the same permissible contact stress figures as cylindrical gears thanks to a stress adjustment constant.

Elasticity factor: The contact stress is affected by the material-specific variables E (modulus of elasticity) and (ν) (Poisson's ratio), which are taken into account by the elasticity factor, Z_E . It can be easily calculated by the formula below:

$$Z_E = \sqrt{\frac{1}{\pi \left(\frac{1-\nu_1^2}{E_1} + \frac{1-\nu_2^2}{E_2} \right)}} \quad (1.8)$$

Permissible contact stress factors and Size factors: Statistics showing a drop in the stress value at which fatigue damage develops with an increment in component size are accounted for by factor Z_x . This is due to how gear size affects material quality (impact on forging process, structural variations) and how smaller stress gradients affect subsurface faults (theoretical stress analysis). The material quality, heat treatment, and module in the case of surface hardening are the key influencing factors

with regard to the size factor; the depth of the hardened layer in relation to the size of the teeth.

For both the pinion and the wheel, the size factor, Z_x , must be established individually. However, it has not yet been determined what suitable gear tooth size factors are. Therefore, for most gears, the size factor is set to one in this clause ($Z_{x1,2} = 1$).

Hypoid Factor: A series of bevel gears with progressively higher relative hypoid offset values were tested. They demonstrate that from zero offset to typical offset levels, the permanent transmissible torque increases, but at very high offset values, it reduces once more. On bevel gears without offset, the Hertzian pressure brought on by the corresponding permanent transmissible torque reaches its maximum; nevertheless, as offset increases, this pressure rapidly diminishes. The only possible explanation is that lower allowed contact stresses on the flank are caused by faster sliding speeds. This decreasing effect is thought to be caused mostly by increasing contact temperatures and degrading lubricant film developments.

The following components of mean point velocities must be taken into account in order to achieve this effect: the addition of sliding velocities which are vertical to the contact line, $v_{\Sigma,vert}$, which is beneficial for the oil film, and the sliding velocity parallel to the contact line $v_{g,par}$, which is unfavorable for the temperature and the thickness of the oil film. In the case of hypoid gears, both components rise with the value of the offset, although $v_{g,par}$ does so more so than $v_{\Sigma,vert}$ in bevel gears without offset. Therefore, compared to cylindrical gears and bevel gears without offset, hypoid gears exhibit different temperature and oil film behavior, which is shown by the ratio of the two components. The hypoid factor, Z_{Hyp} , is a component of method B1's surface durability rating calculation to take this effect into account.

Hypoid factor can be calculated by this formula:

$$Z_{Hyp} = 1 - 0,3 \left(\frac{v_{g,par}}{v_{\Sigma,vert}} - 0,15 \right) \quad (1.9)$$

Finally, the overview of ISO 10300-2:2014 has been concluded by providing a basic knowledge of the standardized techniques for calculating surface durability. It is important to note that while the presentation has covered important elements, some complex equations and elements crucial for precise gear analysis have been omitted.

The ISO 10300 standard opens the door to excess of additional considerations, such as material characteristics, lubrication dynamics, and a number of equations that collectively improve the accuracy of gear analysis. Even though it was focused on a few particulars, there are more factors overall that merit investigation.

The research paper by Drechsel et al. [7] introduces a sophisticated calculation approach that is consistent with the ideas in ISO 10300-2:2014 [12] while going above and beyond by offering an extended method for figuring out the capacity of bevel and hypoid gears to carry pitting loads.

By incorporating a calculation method that more accurately considers the complex geometry of bevel and hypoid gears, Drechsel et al.'s work offers an innovative point of view. Compared to the standard ISO 10300-2:2014 [12] method, which concentrates on just one representative point on the path of contact, this extended approach involves meticulous calculations along the entire path of contact of a virtual cylindrical gear geometry. The extended method accomplishes this by providing an accurate estimate of the pitting load carrying capacity.

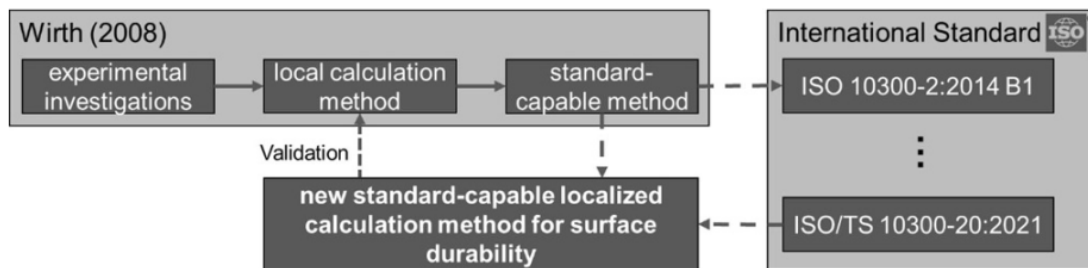


Figure 1.4.1: Illustration of the relationships between the calculation techniques for the load carrying capacities of bevel gears explained in the paper by Drechsel et al. [7]

While Drechsel et al.'s paper serves as a prime example of how the field continuously evolves through innovative approaches that enhance the accuracy and applicability of gear analysis, this thesis focused largely on ISO 10300-2:2014 [12].

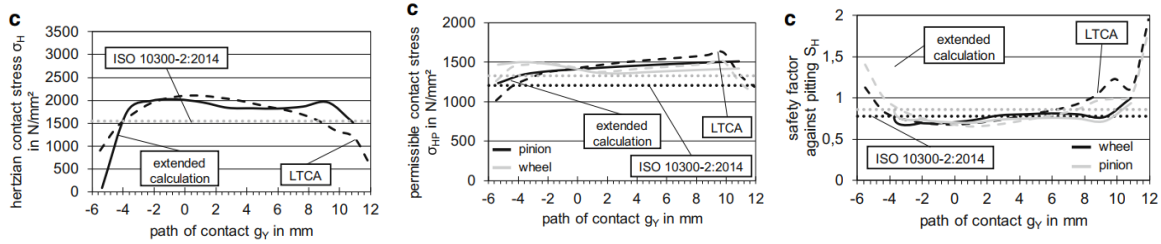


Figure 1.4.2: Comparison of the extended approach, ISO 10300-2:2014 and LTCA methods for Hertzian contact stress, permissible contact stress, and safety factor against pitting for G31.75 Gear Set [7]

In summary, the exploration of ISO 10300-2:2014 [12] and subsequent discovery of the study by Drechsel et al. [7] highlight the value of having a fundamental understanding of standards while also recognizing the ongoing developments that continue to expand the field of gear analysis. This related relationship between well-established standards and cutting-edge research serves as a reminder that both traditional principles and cutting-edge methodologies must be incorporated for a thorough understanding of the field.

1.5 Experimental Investigations in Gear Research

The experimental investigations carried out by Höhn, Stahl, and Wirth [10] have significantly contributed to understanding of new methodologies for calculating the load capacity of bevel and hypoid gears. Their research involved designing and conducting experiments with two distinct types of bevel gears: one tailored for pitting tests and another for tooth root tests. This approach aimed to isolate and analyze pitting phenomena independently from tooth root breakage effects. Information in this section is based on references [10, 14].

The designed gears for tooth root tests exhibited offsets of $a = 0$ mm, 15 mm, and 31.75 mm, coupled with a relatively modest module ($m_{mn} = 2.2 \dots 2.5$ mm). In contrast, the gears for the pitting tests featured offsets of $a = 0$ mm, 15 mm, 31.75 mm, and 44 mm, employing a larger module ($m_{mn} = 3.5 \dots 4.2$ mm). The gear wheels shared a consistent outer diameter of 170 mm, with a composition of 18CrNiMo7-6, characterized by case hardening and finish grinding [10].

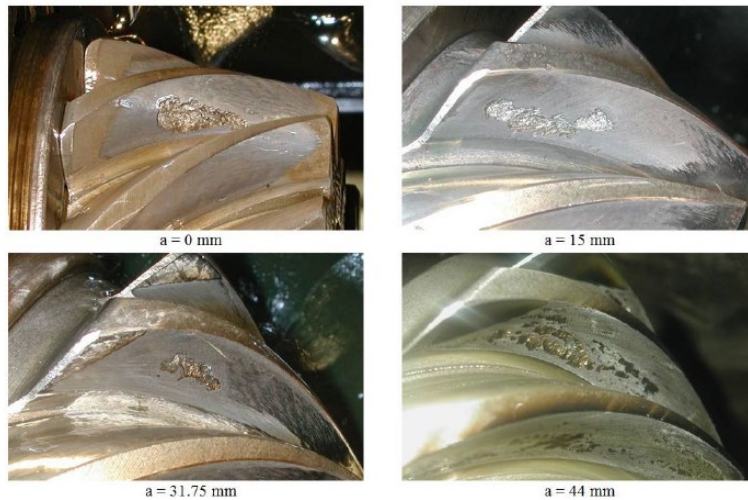


Figure 1.5.1 : Typical pitting at the pinion flanks on the investigated test gears [10]

Findings from the pitting tests revealed occurrences of pitting and micropitting across different test gear geometries. Notably, the area of micropitting on the flank exhibited proportional growth in size and frequency as the offset increased. This pattern of pitting was visually captured in Fig. 1.5.1, displaying typical pitting on the pinion flanks for all four test gear configurations.

The research underscored the interconnectedness between micropitting induced flank form deviations and the subsequent load distribution on the flank throughout its operational life. This phenomenon led to fluctuations in load conditions, which, in turn, influenced the occurrence of pitting. Specifically, in tests conducted at torques approaching the gear set endurance limit, micropitting exerted a heightened influence due to extended operational periods [10].

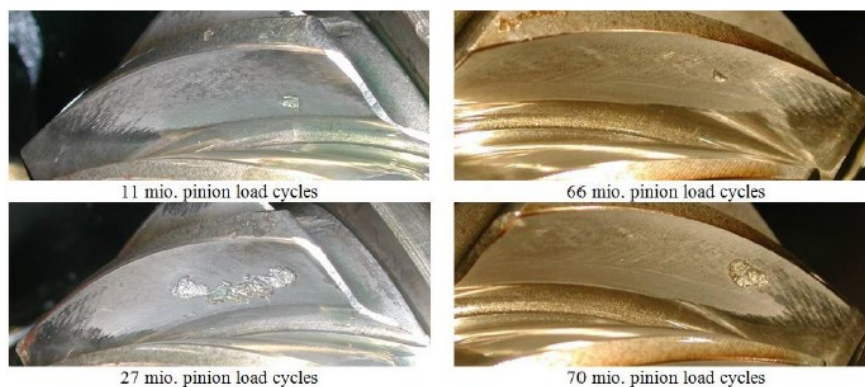


Figure 1.5.2: left: micro pitting and pitting on pinion flank, right: initial pitting at the addendum of the pinion ($T_1 = 300 \text{ Nm}$, $a = 15 \text{ mm}$) [10]

Furthermore, variations in geometry offset ($a = 0$ mm, $a = 15$ mm, $a = 31.75$ mm, and $a = 44$ mm) yielded differential micropitting distributions, impacting both pitting behavior and overall gear functionality. Notably, the research highlighted that micro pitting influenced the initiation of pitting at the addendum of the gear teeth, diverging from the established pattern in helical gears.

The experimental data successfully facilitated the determination of the endurance limit for pitting across various test variants. Importantly, the analysis also showcased the pivotal role of factors such as Hertzian stress, component elasticity, and geometry offset. The loaded tooth contact analysis (LTCA) tool, BECAL, developed by the FVA (*Forschungsvereinigung Antriebstechnik*), played a key role in assessing the maximum stresses on gear flanks. Specifically, the maximum stress on the flank of $a = 44$ mm variant for the endurance limit exhibited a marked reduction compared to the non-hypoid variant.

Therewithal, another research that was made by the same individuals introduces a novel local calculation method for assessing pitting in bevel and hypoid gears. As mentioned, this method is based on the outcomes of a loaded tooth contact analysis performed using BECAL. (See chapter 5.) To derive local strength values, ISO 6336 specifications for helical gears are utilized due to their established statistical reliability. A specific criterion is devised for pitting evaluation, which involves comparing the Hertzian pressure at a specific contact point with the helical gear strength values from ISO 6336 [10, 14].

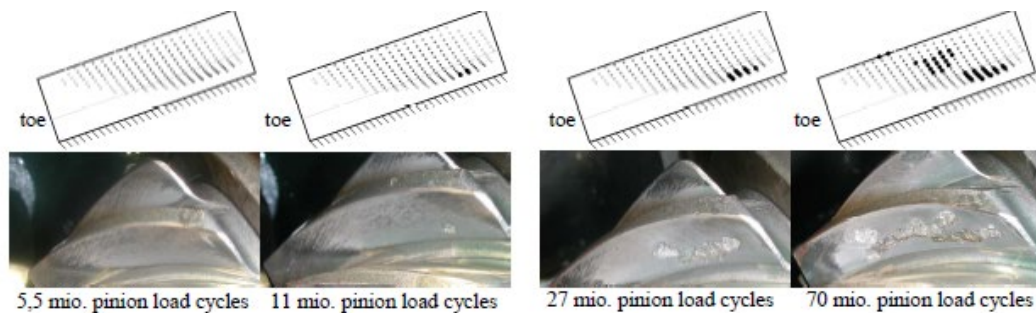


Figure 1.5.3 : Calculated and Experimentally Investigated Results of Pitting [10]

The study reveals that considering local sliding conditions is essential to accurately assessing the entire flank behavior. The research acknowledges that positive slip regions in helical gears exhibit higher pitting resistance. This insight is incorporated into the new calculation method through the "slip factor". Additionally, the impact of hypoid-specific sliding lengthwise along the contact line is quantified using the "hypoid factor". A local pitting safety factor is calculated by considering local contact stress and permissible contact stress.

The recalculation of pitting tests demonstrates a commendable agreement between predicted and actual pitting areas on flanks. The method not only correctly predicts the initiation of pitting but also reasonably anticipates pitting dynamics. The slip factor is introduced to address the relationship between relative sliding and permissible contact stresses on the flank. It compensates for the fact that ISO 6336 strength values are solely applicable to negative slip scenarios.

Furthermore, hypoid gears involve lengthwise sliding due to nonintersecting axes, a factor does not present in helical gears or bevel gears without offset. The influence of this lengthwise sliding on pitting resistance necessitates consideration when applying helical gear strength values to hypoid gear calculations. The "hypoid factor" is introduced to account for this influence empirically. This factor covers various phenomena, including temperature effects on lubricating film thickness, material strength, thermal stress distribution, and fracture mechanics on the surface.

To summarize, the proposed local calculation method for pitting in bevel and hypoid gears integrates slip and hypoid factors to account for specific sliding conditions. The method demonstrates its applicability through recalculated pitting tests and provides insights into accurately predicting and understanding pitting dynamics in various gear configurations.

In conclusion, the experimental investigations conducted by Stahl et al. have provided insights into the intricate relationships governing gear design, offset, micropitting, and load capacity. In light of the above work, in the following chapters of this thesis, the findings from experiments will be examined in more detail, the results will be explained, and this will contribute to a broader understanding of the behavior of bevel and hypoid gears [10, 25, 26].

1.6 Strength Rating Methods and Review for Bevel and Hypoid Gears

A general review is given in this section. The information in this chapter 1.6 retrieved from the [1, 17] references. Standards such as AGMA and ISO, carry out the strength rating of bevel gears using virtual cylindrical gears, with only a few particular bevel gear factors changed. Calculating allowable stresses and, ultimately, safety factors are part of rating methodology of these standards. Additionally, the integrated S-N curves allow for a lifetime prediction and take into account an increased permissible stress during limited life. A contact analysis is crucial for determining the stresses bevel gears must withstand. Through this approach, researchers could take into account changes to the gear flanks, such as crowning or twisting, and the associated motions. Because acceptable stresses are determined via contact analysis, neither safety nor the longevity

of the equipment are made known. When using both strategies, standards need to be flexible enough to take into account the primary stress influencing factors. The ISO 10300-2:2014 standard, which takes these considerations into account, has more flexibility than the AGMA 2003: D19 standard.

Additionally, the values for bending stress reported by AGMA 2003: D19 are quite distinct from those discovered using contact analysis. The accuracy of rating bevel gears is substantially improved by combining the two calculating approaches. It starts by determining the displacements for a sample pair of bevel gears. Then, using the stress information gained through contact analysis, researchers establish the pertinent parameters for the rating standard.

Macro geometry of the bevel gear is then improved by changing important variables in accordance with predetermined computations. For each of these solutions, researchers can assess several failure modes, such as root bending, pitting, scuffing, and flank fracture. Theoretically, bevel gears can be rated using a variety of methods, including rating standards and loaded tooth contact analysis (LTCA). The results that each of these approaches generates, their level of accuracy, and the amount of time needed for calculations all vary. They are therefore used at different stages of the design process.

Although some details were not given before, the non-detailed comparison of the methods can be seen in Figure 1.6.1 below.

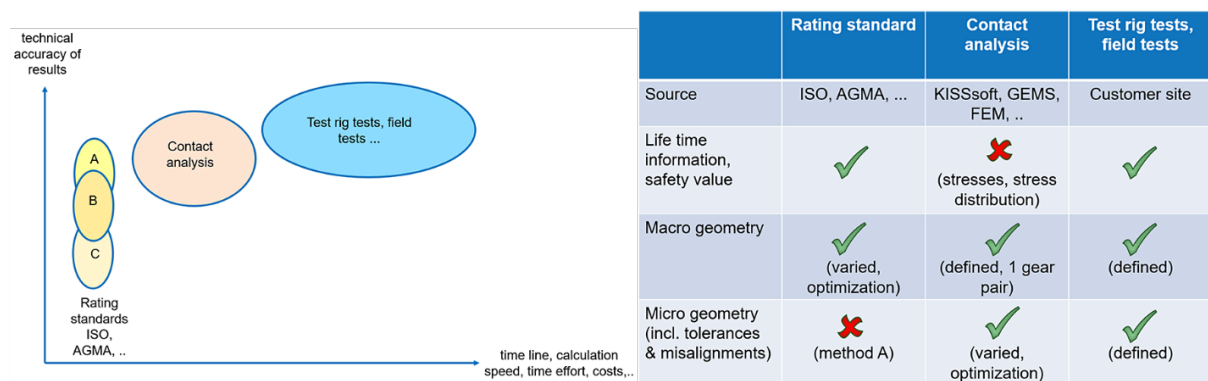


Figure 1.6.1 : Result types (right) and available methods for rating strength (left) [1]

Different results can be obtained using different methodologies. So, for instance, only rating standards or test rig trials can yield lifetime results. Contrarily, the LTCA offers the highest level of stress accuracy because it can take into account specifics like manufactured modifications and precise misalignments. A system design analysis

provides the misalignment values and results for the three-dimensional position of the two meshing members as a result of shaft, bearing, and housing deflections [1, 17].

1.6.1 Rating Standards and Methods

ISO 10300: The relevant standard has been described in detail in previous sections, but for brevity, this section will provide a final review. The ISO 10300 rating standard is used by the International Organization for Standardization (ISO). For bevel and hypoid gears, it currently includes the evaluation of tooth bending, pitting, and scuffing. Currently in new editions have the rating calculations for the failure modes flank fracture and micropitting [1, 17]. The engineer can change a number of parameters to the current bevel-gear design and application using ISO 10300.

The main purpose of ISO 10300 is to achieve a factor of safety against pitting or other failures.

AGMA 2003: The American Gear Manufacturers Association offers the latest version of the rating standard known as AGMA 2003: D19. It includes calculations for pitting and root bending stress. However, this standard has not been used or studied in detail in this study.

Rating by Gleason Q-factor: The Q-factor enables the bending stress to be rated. It was created by Wells Coleman and is applied in an approach comparable to that of the AGMA calculation. It contains the Pd, Ks, F, D, and J parameters. Coleman improved this version in 1981, and Gleason now uses it with the ability to account for hypoid gears.

Loaded Contact Analysis: A loaded contact analysis (LTCA) can be used to calculate the stresses for bevel and hypoid gears using specialized tools that use like Finite Element or Boundary Element methods. With the help of this analysis, the engineer is able to take into account each individual flank modification, such as crowning, twisting, etc., that is required to achieve the best possible configuration a variety of load conditions. The displacements between the pinion and ring gear are also taken into account [1, 17].

Based on the machine settings and tool geometry, the loaded and no-load TCA both account for the precise flank topology produced during the manufacturing process. This enables the engineer to assess the gear set strength, rolling capability, and NVH behaviour.

The rating standards call for a specific amount of adaptability to fine-tune the key parameters and produce accurate results near to the LTCA. The reaction forces and stiffness of the shafts, bearings, and housing structure cause the pinion and wheel gear

to be out of alignment when the system is under load. The parameters, which are accumulated from the pinion and wheel-gear deflections, define the misalignments.

The process of combining both calculation methods significantly improve the accuracy of bevel gear design and simulation. The rating standard can be adjusted to produce stress results based on the numbers for stress that the LTCA produced. The resulting lifetimes and safety factors are calculated along with the allowable stresses.

The ISO standard enables the engineer to modify a few parameters for the LTCA comparison. There are some (but fewer) adaptation options for the AGMA standard as well [1].

Ultimately, Loaded Tooth Contact Analysis (LTCA) offers a comprehensive understanding of tooth contact characteristics. This is achieved by considering tooth deformation and shaft deflection caused by loading, which play a crucial role in determining the true geometry of the contacting tooth surfaces. Moreover, LTCA analysis was performed in this study with the software BECAL. However, the numerical infrastructure of the method has not been discussed in detail.

2. Back-to-Back Test Rig at Gear Research Center (FZG)

The Institute of Machine Elements, also known as the "Gear Research Center (FZG)", provides facilities for inspecting and testing machine elements, including gears, bearings, synchronizations, and couplings [8]. The experiments of this study were carried out at the FZG at the Technical University of Munich.

One of the primary research focus areas of this research center is the load-carrying capability of gear drives. Additional significant parts of research for automotive applications have emerged, including rolling element bearings, multidisc clutches, and synchromesh systems. The focus of research efforts at FZG is on the consideration of fatigue life, efficiency, friction, and vibration behavior of gears and transmission elements [8].

As stated, the work done for this thesis focuses on the specific Back-to-Back Hypoid Test Rig at the Gear Research Center (FZG), which is used for the experimental research of gear failure that also has analytically developed calculation methods. Similar to the researches done in FZG, various institutions such as the "Laboratory for Machine Tools and Production Engineering (WZL), RWTH Aachen University", "Research Association for Drive Technology (FVA)", "Gear Research Institute (GRI), Penn State", "The Gear and Power Transmission Research Laboratory, The Ohio State University", "School of Mechanical Engineering, University of Shanghai for Science and Technology" and "Tokyo Institute of Technology" are also engaged in different studies related to gears. These academic institutions contribute to the fields of mechanical gear system design, production, and performance analysis. These studies form a scientific foundation for the development of more efficient and reliable gear systems for industrial applications. In addition to the back-to-back hypoid test rig, several other specialized test systems are available for research purposes at different institutions. These testing facilities support a wide range of gear engineering research questions.

Other test rigs available at FZG, for example, include: the Dynamic Test Rig, which has a 140 mm gear center distance, and focuses on investigating dynamic forces in spur

and helical gears. Utilizing a hydrostatic load device, the Load Spectra Test Rig applies torque and examines operational load-carrying capacity. The FZG Efficiency Test Rig investigates tooth geometry and flank surface properties under load and in no-load situations, as well as dissipation, efficiency, heat balance, and frictional behavior of lubrication and lubricants. Additionally, there are specialized test rigs that each serve a particular research need, such as the Worm Gear Test Rig (electrically loaded), Internal Gear Test Rig, Three-Shaft Test Rig, and the Drag Torque Test Rig [8]. Together, these adaptable testing facilities help researchers to learn more about gear systems and gears.

2.1 Introduction to FZG Back-to-Back Test Rig for Bevel and Hypoid Gears

This section provides a thorough review of particular details related to the test rig. The related information below is retrieved from the [25].

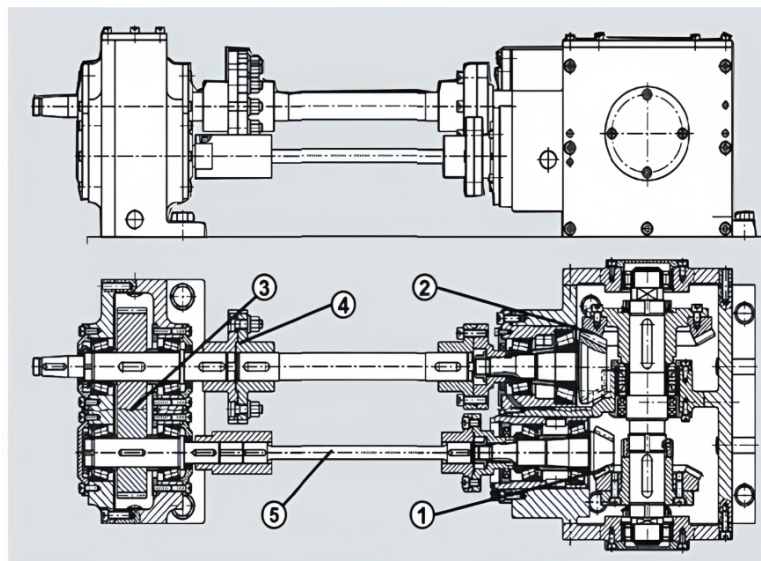


Figure 2.1.1: FZG Back-to-Back Hypoid Test Rig [25]

The closed cycle test rig used in the research project consists of the following components:

- the test gear set (1)
- transmission gear set (2)
- spur gear set (3)
- mechanical load clutch (4)
- torsional shaft (5)

The tests were performed on a hypoid back-to-back test rig, which functions according to the closed power circuit model. Two hypoid gear sets—the test gear set (1) and the transmission gear set (2)—are used in this rig, and they are joined to a spur gear set (3) by parallel shafts and a mechanical load clutch (4).

As the working principle of the testing mechanism, a particular torque value is imputed from the mechanical load clutch (4) and the corresponding cycle is repeated until any type of failure of testing gears set, is measured. The rig have, a second hypoid gearbox (2) with larger dimensions and a cylindrical gear stage to load the test bevel or hypoid gearbox. The test rig is utilized for hypoid gear oil tests as well as the evaluation of tooth root and tooth flank load-carrying capacity. The FZG scuffing test for cylindrical gears served as a model for the development of test procedures for scuffing, pitting, and other wear behaviors.

Specifications of the test rig [8]:

Axial offset: $a = -15, 0, 15, 25, 31.75, 44$ mm

Max. testing power: $P_{\max} = 300$ kW

Outer reference diameter of the gear: $d_{e2} = 170$ mm

Speed range: $n_1 = 100 \dots 4800$ 1/min

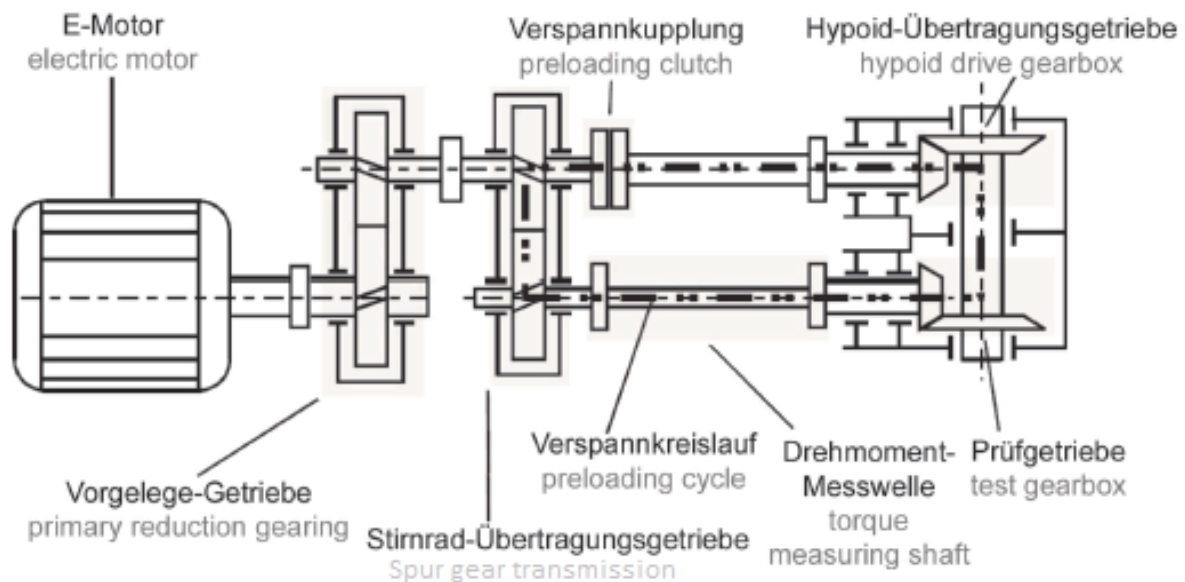


Figure 2.1.2: Bevel and hypoid gear test rig scheme [8]

In this setup, the components of the hypoid back-to-back test rig's power losses are introduced by an electric drive unit. With the support of resilient gearbox and tapered

roller bearings, the test pinion is securely fastened inside of it. This enables axial adjustments for the wheel and pinion. This adjustability allows adjustments to J and H values while ensuring the test gear set has the best possible contact patterns and backlash.

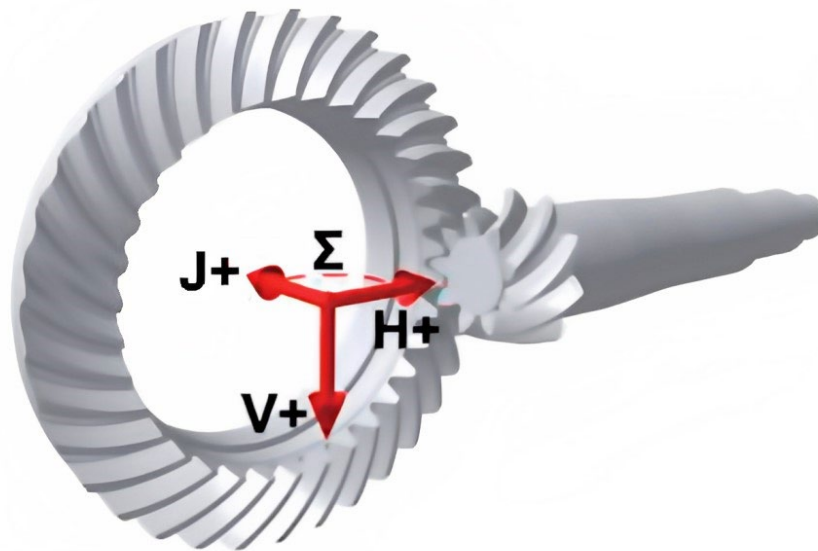


Figure 2.1.3: Representation of Misalignments [25]

Figure 2.1.3 demonstrates how a bevel gear set misalignments are defined. The load clutch halves are twisted against one another to apply load, and several screws hold them together (4). Utilizing strain gauges mounted on the torsional shaft (5), the load level is measured.

The load torque measurement technology is calibrated using predetermined standard weights prior to starting the test run. During the experiments, this calibration guarantees precise load level measurements [25].

Experiments with many different torque values on test rigs with both G0 and G31.75 offsets were conducted in FZG laboratories for this thesis. However, in the following chapters and from this point on, the focus will be solely on the G31.75 Hypoid test rig and its experiments.

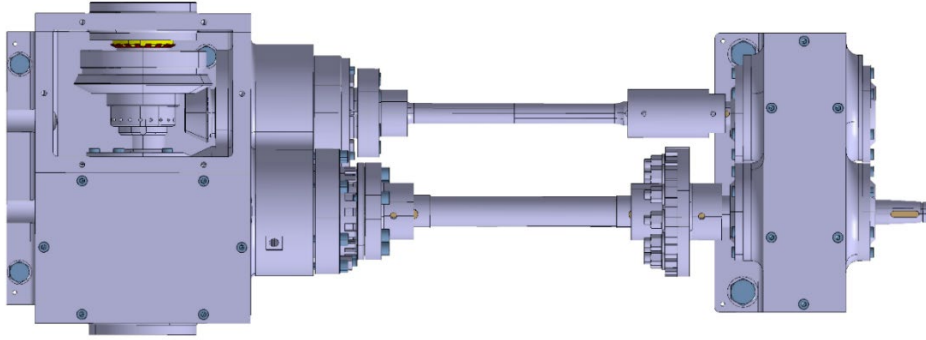


Figure 2.1.4: 3D CAD Drawing of the Test Rig G31.75

The technical drawings of the test rig are also provided in Appendix B.

	Unit	Shell Spirax S6 AXME 75W-90	Mobilube HD 80W-A	Castrol Optigear 100	Klüber Klübersynth GH 6
Lubricant base	-	Synthetic Base Oil	Mineral Oil	Mineral Oil	Fully Synthetic Oil
ISO-VG	-	75W-90	SAE 80W	100	150
kinematic viscosity at 40°C	mm ² /s	115	75	105	150
kinematic viscosity at 100°C	mm ² /s	15.2	9.5	11.5	29
Density at 15°C	g/ml	0.878	0.893	0.893	1,005

Table 2.1.1: Lubricant Properties [36, 37]

Shell Spirax S6 AXME 75W-90 lubricant was used for experimental tests in this thesis. Oils with different physical properties can be used to examine the effect of oil parameters on pitting formation and contact pattern shifting. In previous studies, Mobil Mobilube HD 80W-A and Castrol Optigear 100 was used for pitting. The lubricant details are summarized in Table 2.1.1 [36, 37]. Additionally, the oil temperature is crucial. The lubricant film thickness and, subsequently, the capacity to carry loads that cause scuffing decrease as a result of the viscosity being reduced by increasing temperature [36].

Gear type			Pinion G0	Wheel	Pinion G15	Wheel	Pinion G31.75	Wheel
Number of teeth	$z_{1,2}$	mm	9	34	9	34	34	9
Hypoid offset	a	mm	0		15		31.75	
Mean normal module	m_{mn}	mm	3.57		3.8		4.03	
Normal pressure angle	α_n	°	20.0		18.5		15.9	
Spiral angle	$\beta_{m1,2}$	°	33	33	38.66	27.31	44.99	21.01
Face width	$b_{1,2}$	mm	26	26	27.05	26	31.13	26

Table 2.1.2: Test Gear Parameters [7]

During the thesis process, relevant test rig procedures were systematically performed in the laboratory. To record and assess the test results, the flank surfaces of the gears were photographed at the end of each cycle.

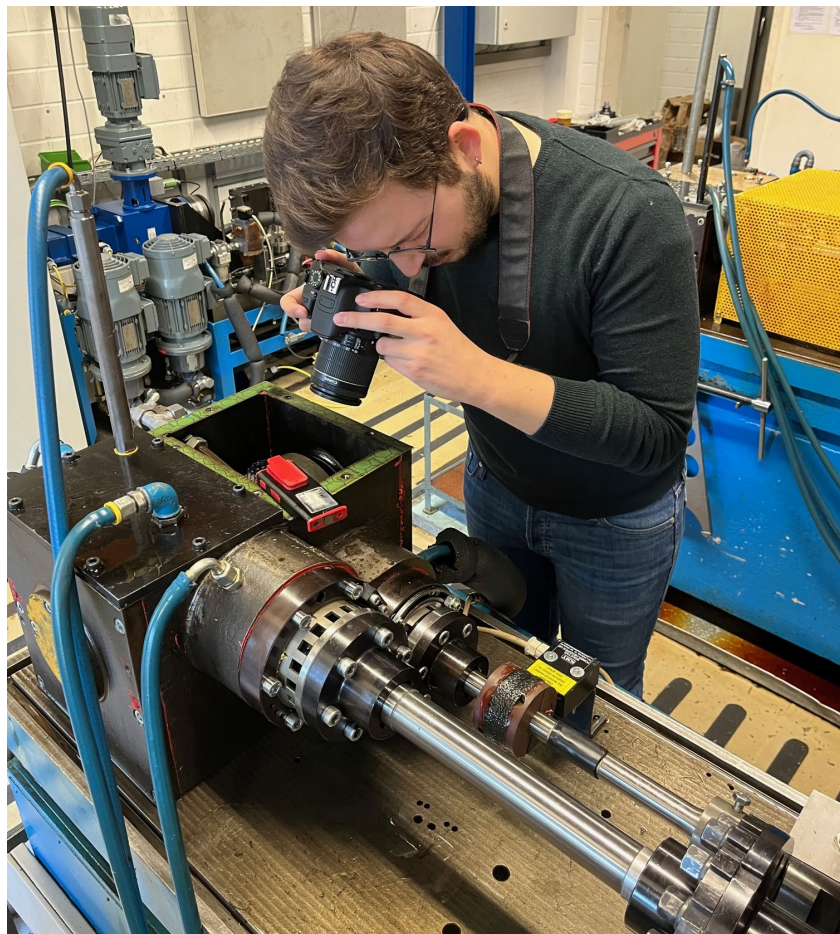


Figure 2.1.5: Photographing Procedure

These procedures included the disassembly of the test gear unit, gearbox cover, crown wheel, pinion shaft (torque measuring shaft), and pinion bowl, as well as pinion demontage. Additionally, assembly processes encompassed the test gear unit, crown wheel flange, and mounting of the pinion in the pinion pot. Conservation of the non-active flank, assembly of the pinion cup and ring gear in the test stand, contact pattern adjustments, measurements of backlash, and preparing the test stand for operation were also executed as required.

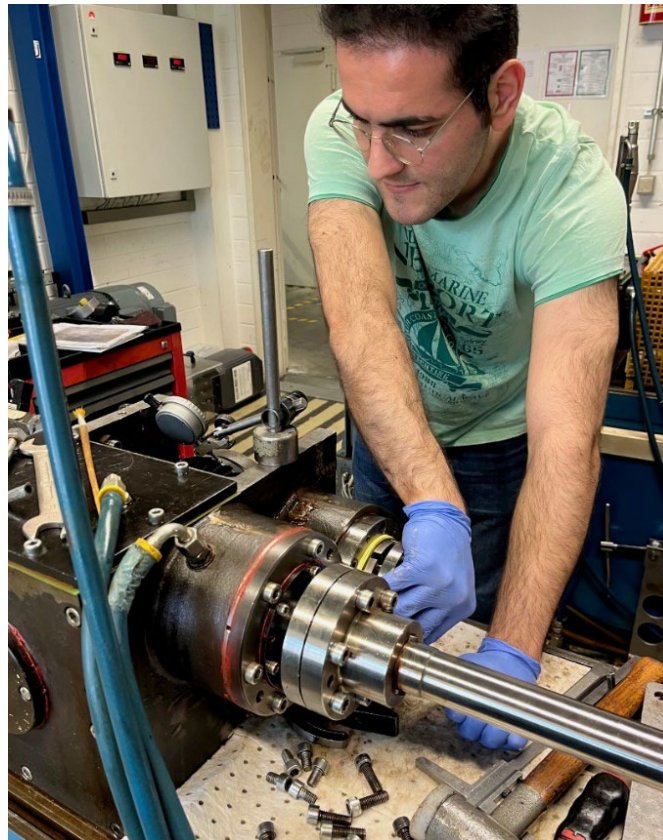


Figure 2.1.6: Gear Set Assembly Process / Backlash Measurement

Additionally, to check the contact pattern in the tests, the flanks were coated with contact pattern paste, and the resulting contact pattern was checked. If necessary, the installation dimensions were corrected to enable a more favorable contact pattern. After adjustment, the contact pattern was documented photographically, and the paste was removed.

As stated, pitting and micropitting formation were reported by photographs, and classical experimental procedures were applied. Furthermore, the reports of experiments conducted consistently documented torque and performed cycles. The evaluation of the studies conducted at the FZG test rig and a comprehensive analysis of them will be discussed in the subsequent sections.

3. Experimental Investigations at Back-To-Back Hypoid Test Rig

3.1 Theoretical Suggestions Regarding the Influence of Micropitting on Contact Pattern

According to the previous studies on micropitting examined in the literature review section (1.3.3), it is suggested that there is a probability of shifting of the contact pattern due to the existence of micropitting on the flank surface. There can be an alteration in the distribution of stress along the tooth contact as a result of the accumulation of micropitting damage on gear flanks. Therefore, the initially clearly defined contact pattern may witness a considerable change, which may influence the load-sharing capability and possibly quicken the development of micropitting. The complexity of gear durability assessment is highlighted by the dynamic interaction between contact pattern shifts brought on by micropitting and the overall micropitting damage. Therefore, there are significant theoretical assumptions regarding the reasonable influences of micropitting on the shifting of contact patterns.

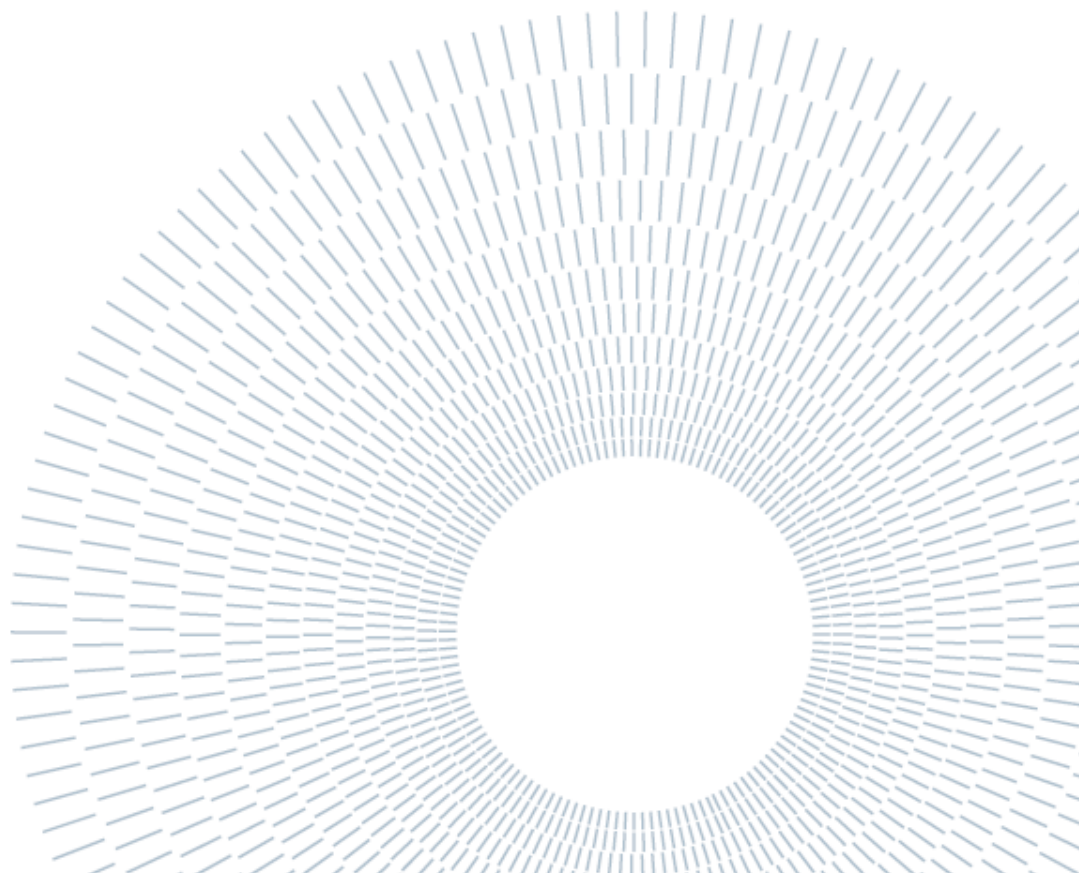
3.2 Description of the Fatigue Test

Over the entire period of the thesis, experimental fatigue tests were carried out on Back-to-Back Hypoid Test Rig at Gear Research Center (FZG) simultaneously with all theoretical, modelling workings.

Initially, disassembly of the test rig for removing failed gear set, is followed by a sufficiently precise installation of new pinion and wheel. Specific painting methods are used in order to fully arrange the contact pattern in the center of gear flanks. Axial positions of both gears, meanwhile backlash and other relevant parameters are noted following the assembly procedure of pinion and wheel. After the assembly of all other components of test rig, such as the testing gearbox, pinion shaft, sensors; the test rig is given two initial pre-testing at low torque levels (100 Nm and 200 Nm) each of which lasts one hour. These initial testing procedures at lower loadings have advantages in terms of checking for any possible installation faults, unexpected errors, and prevention of them in advance. Moreover, initially emerging contact patterns can be noticed on gear flanks and be checked how perfectly they are accumulated on the center.

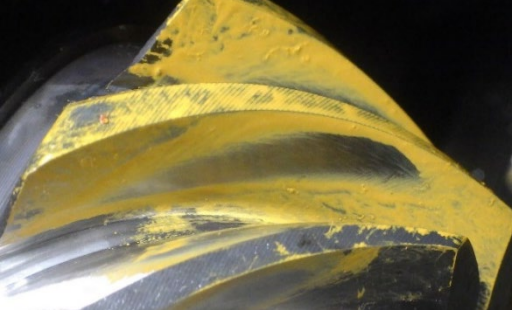
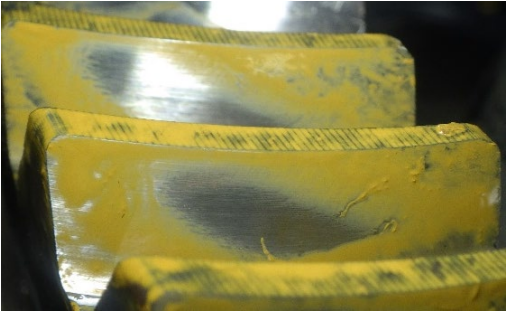
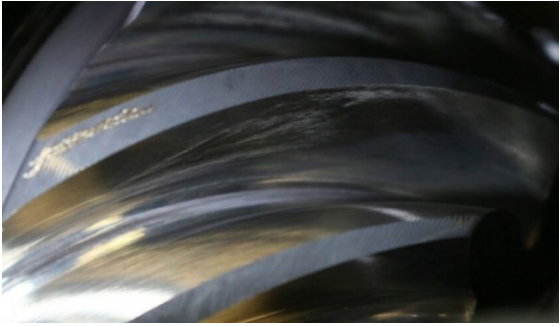
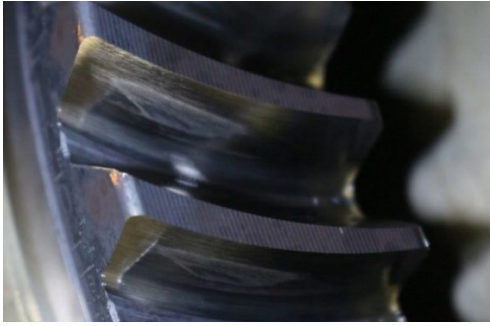


Followingly, the aimed fatigue test can be started at any particular torque value. As the complete failure of the gear set takes millions of cycles, nearly every day or at similar intervals, the test cycle is stopped temporarily to check the teeth of gear set regarding any occurrence of pitting or micropitting or any other possible damage. Following the appropriate photographing of teeth of both gears, the test cycle is restarted at the same torque level. This procedure is repeated until the final failure of gear set.

Noting that, before running the test cycle, the relevant oil is added to the gearbox and is heated to above 45 degrees. The level of it is always adjusted just slightly higher than axis of pinion. The control system of the test rig regulates the oil temperature to maintain it between 45 °C and 90 °C.



3.3 Experimental Test Results

In this section, the results of experimental fatigue test results at the certain torque (400 Nm) are illustrated. Test outputs, in terms of photographs after installation, initial pre-testing at low loading levels, as well as after numerous certain load cycles are shown below.

	Pinion Flank Photo (400Nm)	Wheel Flank Photo (400Nm)
Initial Contact Pattern (No loading)		
Initial Test Run (200Nm)		
LW2.500.000		









LW27.250.000		
LW48.750.000		
LW56.750.000		
LW86.132.000		

Table 3.3.1: Results of experiments on G31.75 Test Rig with 400 Nm torque





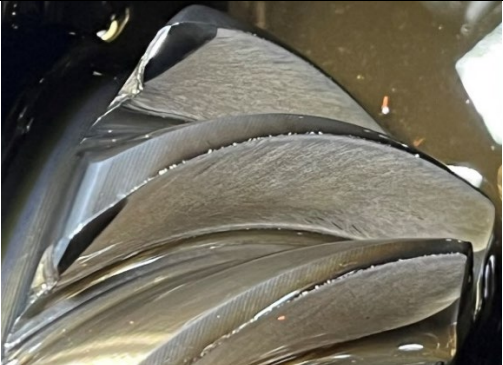

	Pinion Flank Photo(400Nm)		Wheel Flank Photo(400Nm)
LW56.750.000		LW62.073.000	
LW75.073.000		LW75.073.000	
LW78.073.000		LW81.073.000	

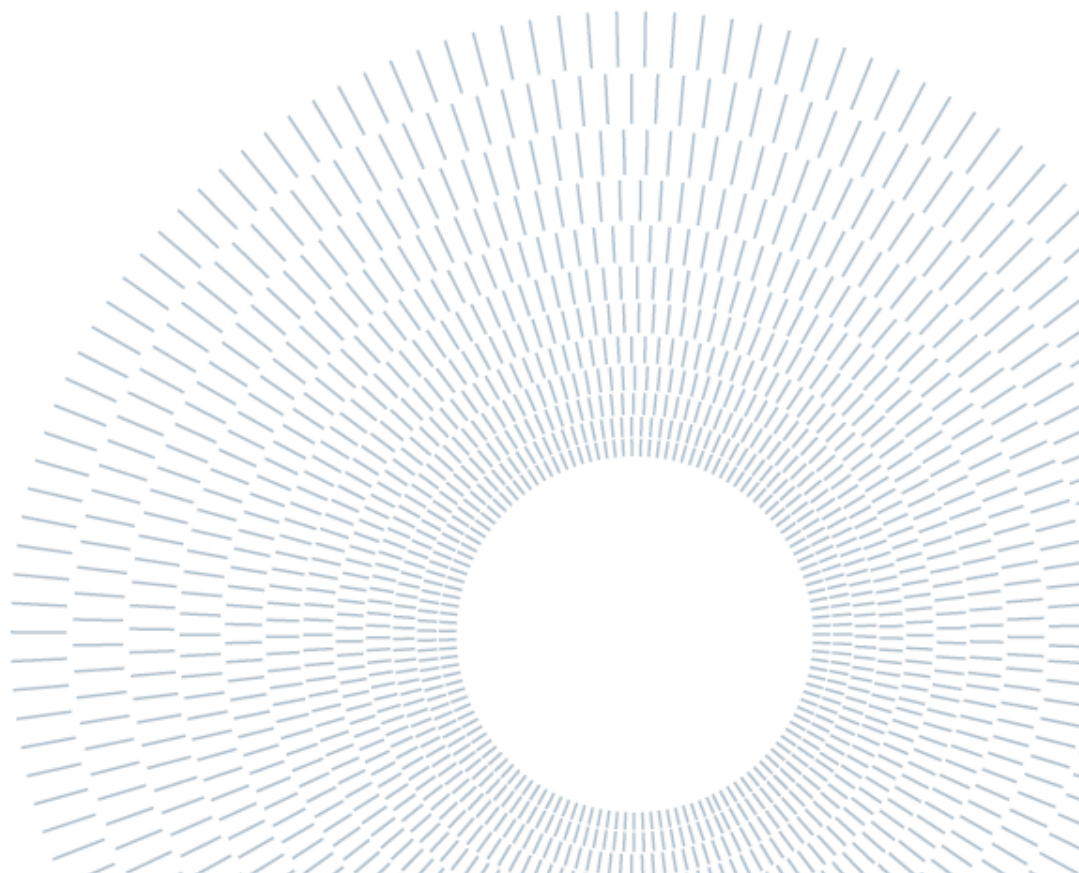
Table 3.3.2: Some Critical Results (in addition to the Table 3.3.1)

It can be definitely observed from images of 400 Nm experimental test results that on the pinion flank surface, where there is an emergence of micropitting after a certain load cycle, there is a significant shifting of the contact pattern. The pitting failure occurs towards the heel of the tooth. On the other hand, on the wheel flank surface, where there is substantially less micropitting, contact pattern occurs in the middle of the flank surface. This experimental results also finds that the existence of micropitting can be the highly dominant effect on the shifting of contact pattern on the flank surface. Therefore, experimental findings are totally consistent with theoretical assumptions,

mentioned in 3.1. In case of micropitting on flank surfaces of gear set, pitting failure occurs at any shifted position rather than the center of gear flank surfaces. As a result, the existence of micropitting can be clearly considered as the dominant factor on the scatter of the experimental results of Back-to-Back Hypoid Test Rig.

In addition, the identical experimental procedure was carefully repeated, and the same steps for the torque level of 250 Nm were strictly followed. Both tests were carried out in the controlled and calibrated environment of the FZG laboratories, in accordance with the research methodology. In this particular iteration, the attention was focused on analyzing the same effects under different loading. Significantly, the outcomes of this replication closely mirrored earlier findings, supporting the validity and reliability of initial predictions. A systematic reiteration of these comparable results is considered unnecessary within the scope of this discussion as a result of the observed consistency, which gives up valuable space for the exploration of more novel aspects of the research. As a result, the findings and results of experiments with a 250 Nm torque value are not reproduced here with supporting photos.

As a new aspect of the research, two different factors are considered and analyzed with relevant methodologies. Although, obvious proof regarding the influence of micropitting on shifting of contact pattern, was found and presented, there might be still other factors which can possible lead to dispersion of experimental results. In the following chapters, new possible factors are discussed in detail.



4. Simulation Modelling of FZG Hypoid Test Rig

This section outlines the utilization of the SMT Masta Program to model and simulate various scenarios for the determination of dominance of defined factors on experimental results within the Back-to-Back Hypoid Test Rig. The outputs of the modelling in this software will be used as inputs at the following steps. The whole method to analyze the influence of particular factors, can be illustrated graphically below:

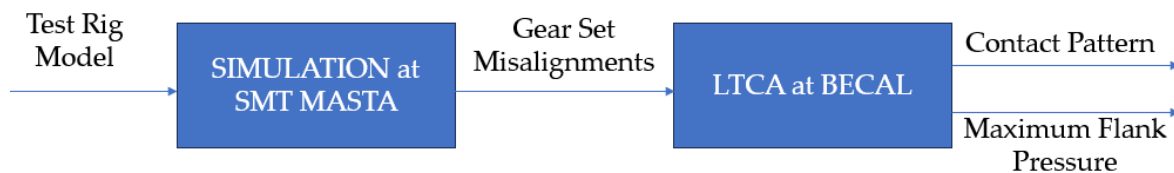


Figure 4.1: Graphical Description of the Analysis of Influences of Factors

The software can provide a variety of analyses, such as NVH, deflection, durability, and FE, and can be used to precisely design and optimize driveline systems and gearboxes. It boasts extensive libraries for common components, makes it simple to integrate various drivetrain configurations, and supports LTCA for precise gear contact analysis. The benefits of Masta virtual environment for investigating design changes and its compatibility with various industry standards are emphasized in the text. Additionally, it describes how KIMoS is used to model gear sets and how it helps with gear design, analysis, and manufacturing optimization. Besides highlighted are the connections between manufacturing processes and Klingelberg contribution to the digital infrastructure used in gear manufacturing.

4.1 General Definition of Modelling Principles of SMT MASTA Software

The SMT Masta Program was used to model the FZG Test Rig and then simulate different test scenarios. For this purpose, this program and its features are described below. The "Masta" software offers a number of attractive advantages. The information in this section has been sourced from reference [28]. Different types of driveline systems and gearboxes can be modeled with SMT Masta. It enables the precise and fast design of transmission systems, whether from scratch or based on imported concepts. Once modeled, different types of analysis and optimizations can be performed, including NVH, deflection, durability, and FE. FE models can be imported using common file formats from the main commercial FE model providers, ANSYS, Nastran, and Abaqus. The results for the full FE model can be extended to display stresses, deflections, mode shapes, and energy content in MASTA.









Button	Mode	Functionality
	Product Database	Allows storage and versioning of MASTA designs in a shared database allowing multiple user collaboration.
	Advanced System Deflection	Perform quasi-static analyses of system deflection and transmission error taking into account varying misalignment through the entire system.
	Modal Analysis & NVH	Assess the potential of system excitation by the gears. Perform Coupled Modal or Gear Whine/Harmonic Excitation analyses.
	Rotor Dynamics	Analyse the dynamic response to unbalanced masses including calculation of the speed dependent modes of the system taking into account gyroscopic effects. Generate critical speed maps for varying bearing stiffnesses.
	Parametric Study Tool	Enables the analysis and reporting of the impact of varying the properties of a component within a design for a particular load case or duty cycle.
	Cylindrical Gear Manufacturing	Simulation and optimisation of cylindrical gear manufacturing processes including gear cutter simulation, fillet optimisation, process simulation
	Bevel Gear Manufacturing	Simulation of spiral bevel and hypoid bevel gear manufacturing processes.
	Benchmarking	Enables recording of measured data from a target transmission & then comparison against a model built in MASTA.

Figure 4.1.1: Some analysis modules on MASTA [28]

MASTA also provides a comprehensive understanding of the lifetime of a mechanical component throughout the customer duty cycle, facilitating early identification of potential failure modes during product development. The program also enables rapid prediction of key performance metrics during the design phase. Its virtual environment allows easy exploration of changes in transmission layout, component selection, design, materials, and manufacturing processes. MASTA also has many different libraries. Comprehensive database featuring over 44,000 bearings in the catalog. With these libraries, standard machine elements and parts such as cylindrical

gears, shafts, bearings, clutches, synchronizers, splines, and other couplings can be easily adapted to the model. At the same time, bearing related parameters such as preloading and stiffness can be adjusted [28].

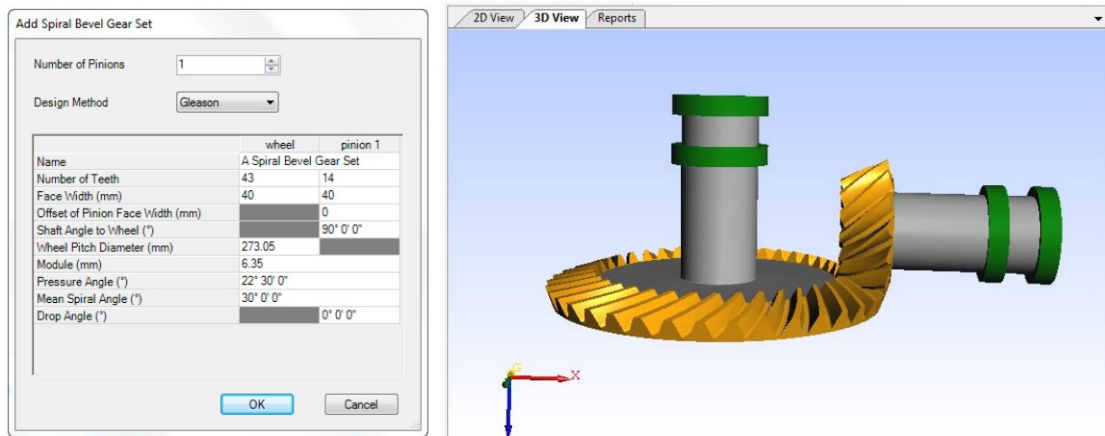


Figure 4.1.2: Gear Import Module and Gear Pair 3D Visualization [28]

With MASTA, many different options are available when modelling a system from scratch. For example, a gear set can be input directly into the KiMOS program, or parameters from methods such as Gleason, AGMA can be input into the program. This way, the macrogeometry of the gear can be readily incorporated into the program.

Gleason: Design is based on the published Gleason document, “Spiral bevel gear system”, Gleason Works, Rochester N.Y. U.S.A. 1964.

AGMA: Based on, “Design manual for bevel gears”, AGMA standard, ANSI/AGMA 2005-D03.

While AGMA leans toward defining tooth proportions on the mean section of the gear, Gleason tends to concentrate on defining these proportions on the outer section of the gear. Notably, there are variations between these two standards in the suggested tooth proportions. Additionally, there are different ways to specify tooth thickness; AGMA 2005-D03 does this by using the Circular Thickness Factor. The distribution of backlash between gears is another area of contrast: Gleason reduces the pinion's tooth thickness by attributing all the backlash to the pinion. In contrast, when calculating the tooth thickness, AGMA 2005-D03 equally distributes the backlash among the gears. These differences highlight the different philosophies that Gleason and AGMA adopted for their respective standards. But instead of these two methods, we imported the parameters to MASTA via KiMoS. The reasons for this and the details of KiMoS are explained in detail in the following sections [17, 28, 32].

Apart from that, a 2D drawing can be used in MASTA even though it is in different file formats. With the help of these 2D technical drawings, models can be easily created in MASTA with the correct dimensions. The program automatically detects lines and similar elements in 2D models.

In particular, "Masta" supports full system simulations for various transmission and drivetrain configurations and seamlessly integrates production simulation into the design process, reducing process development time and associated costs. The unique and modern architecture of software, developed from scratch in C#, significantly increases stability, making it a highly reliable benchmark solution for current and future operating systems.

At the same time, this program has the capability to do LTCA. To start with, MASTA Loaded Tooth Contact Analysis is used to calculate the loaded contact conditions that occur between meshing gears under various loading scenarios. The contact lines are purposefully divided into separate strips as part of this computational process, which employs a strip model. A finite element (FE) model that accurately captures the geometric characteristics of the gears is used to calculate the bending stiffness for each of these strips. The analysis also accounts for the determination of local contact stiffness at the points of contact, which is accomplished through the use of Hertzian contact equations.

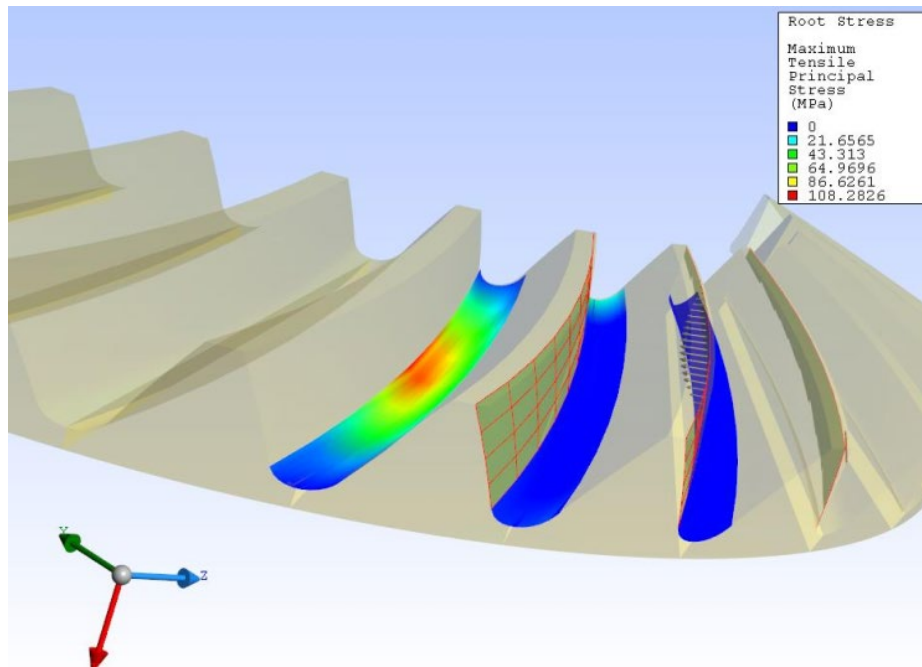


Figure 4.1.3: MASTA LTCA 3D View [28]

This process helps to determine crucial elements like transmission error and root stress. The inputs necessary for this calculation include a number of different parameters, such as the gear macro geometry, the finishing machine settings, the degree of mesh misalignment (as determined by the MASTA System Deflection Calculation), and the input torque. The loads on each individual strip are determined by performing a force balance analysis, which enables the determination of crucial factors like load distribution, contact patch characteristics, transmission error, and root stress distribution throughout the gear system. It is significant to note that this analysis is predicated on a number of assumptions. The neglect of friction in the contact zone, the exclusion of the effects of lubricants on contact pressure distribution, and the assumption that any displacements caused by tooth or contact deflection remain sufficiently minute to prevent the displacement of contact points from their theoretical no-load positions are a few examples. As long as the normal orientation of the tooth surface at the point of contact is maintained, the analysis also considers displacements resulting from tooth or contact deflection to be negligible. This analysis method makes a contribution to the improvement of gear system performance by providing a way to gain understanding of the complex interactions and loading circumstances experienced by meshing gears. Despite MASTA having these features, the LTCA will be conducted using BECAL. This program and its features will be explained in the following sections.

Lastly, MASTA creates reports to effectively present analysis results and facilitate easy configuration of designs and analysis features. These reports consist of organized collections of tabular data, graphs, and images that can span one or more columns.

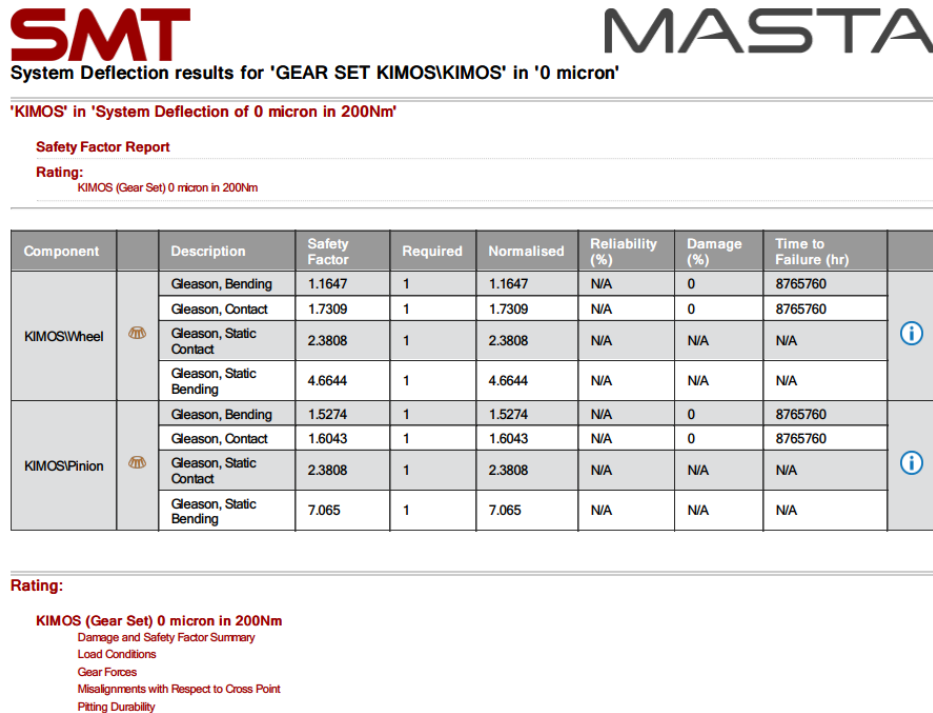


Figure 4.1.4: Example for MASTA Report

Reports can also be accessed through a dedicated Reports in most MASTA operating modes, and some modes offer an additional CAD Reports. Reports come with pre-configured defaults that can be easily customized. This customization allows users to add additional information, change the order of data reported or entered, or tailor the output to fit specific formatting requirements. This flexibility is particularly useful for maintaining standardized presentation formats or adapting output to match historical reports or other software output to facilitate comparisons.

4.2 Simulation Model of The FZG Hypoid Test Rig

Regarding the numerical modeling of this real experimental testing rig, it is not necessary to model the whole test cycle in the SMT MASTA software. Only sections connected to the testing gear set are enough to be modeled. Therefore, a testing pinion with its shaft, testing wheel, simplified slave wheel, the shaft connecting testing wheel to slave wheel, housing with bearings are sufficient to be included. The input load which is applied from the starting of the pinion shaft (shown with an abstract red ring in Fig 4.2.1), is transferred from pinion to wheel, and then transferred to slave wheel through connecting shaft. Output load is measured on the pitch diameter of the

simplified slave wheel. The location of output load is shown with an abstract red ring in Fig 4.2.1.

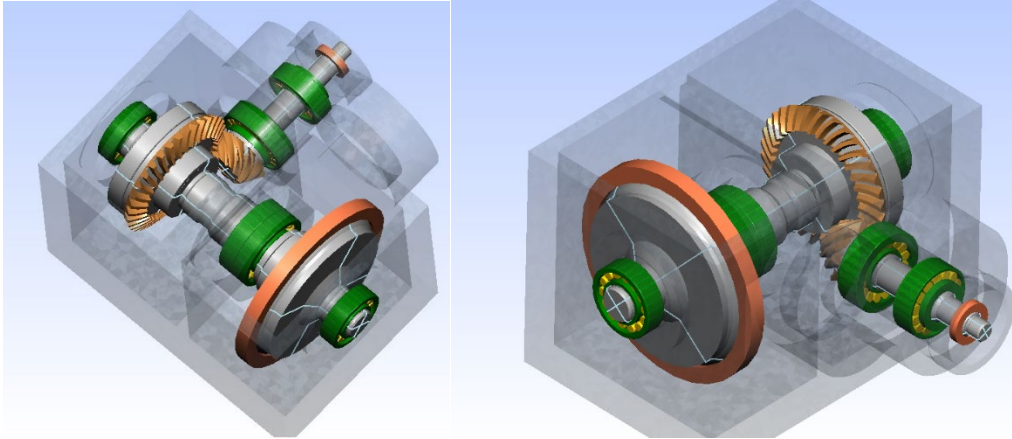


Figure 4.2.1: 3D view of modeled testing mechanism

Pinion and wheel tooth models can be directly imported to the MASTA software by the .xtl file. These parameters were created with KIMoS. Spiral bevel gears can be designed, optimized, and produced with using KIMoS (Klingelnberg Integrated Manufacturing of Spiral Bevel Gears) for a variety of gearing systems. By simulating the manufacturing process and the resulting combination of tooth flanks, the operational performance of the gear set may be thoroughly evaluated and improved. This includes integrating theoretical nominal tooth flank measurements, theoretical machine settings, tool data, and optimized machine settings, all of which are carefully maintained in one or more large databases that contain all relevant data records [19, 20].

Within KIMoS, the parameters offered in the XML data are crucial for the design and analysis of bevel gear sets. Standard mechanical engineering equations and ISO standards are used to calculate these parameters, along with the application's particular requirements and limitations. Comprehensive geometry dimensioning for a variety of common bevel gear manufacturing processes is provided by the KIMoS software. According to accepted industry standards, it makes macrogeometry inspection easier. A thorough analysis of gear performance is possible thanks to the software's ability to simulate the manufacturing process and contact conditions. The software enables load-free running quality optimization through tooth contact analysis.

To find potential conflicts, KIMoS also performs interference analysis. Under operational load, the software also performs tooth contact analysis while taking into

account the actual tooth form. In the end, KIMoS makes it easier to provide data for production and quality control purposes, ensuring a reliable and effective gear design and manufacturing process.

Please be aware that the calculations and methodologies can change depending on the engineering practices and gear design standards applied in the sector [19, 20].

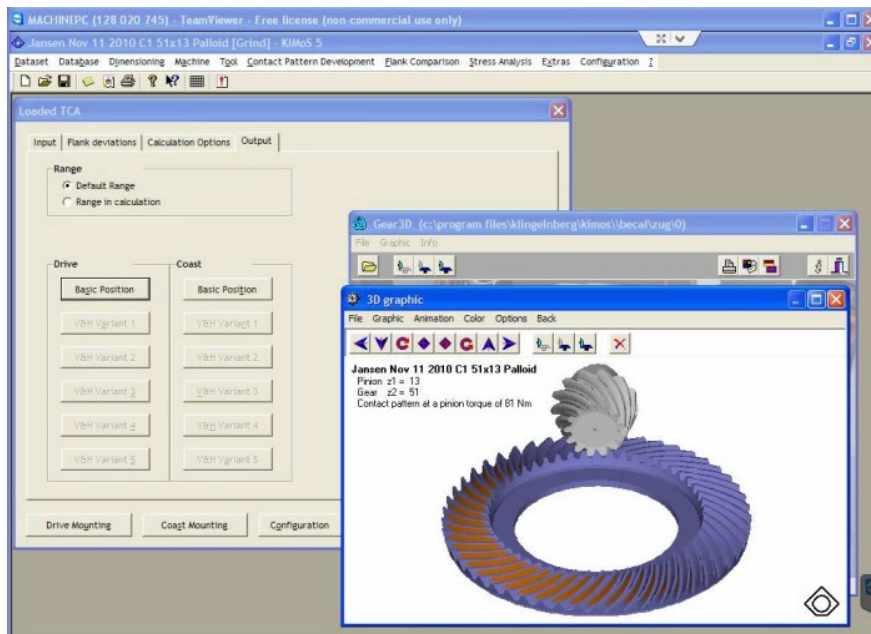


Figure 4.2.2: Contact Pattern Visualization on KIMoS [20]

To elaborate further, complete geometrical information of the component is included in Klingelnberg system along with details on the tool and the manufacturing motion of a virtual cutting machine for both soft and hard machining. The KIMoS program system from Klingelnberg automatically supplies these data, which serve as the foundation of every production step's digital infrastructure.

As a result, every machine and program system involved in the process has been horizontally integrated, and a central database contains digital twins and the technological parameters that determine the geometry for every stage of the manufacturing process. In a cross-sectional simulation, Klingelnberg calculated how the tool penetrates the component. And using its software, Klingelnberg was able to digitize the development of the tooth flanks for the first time. The KIMoS program was refined by the creators until the design tool generated a tooth flank geometry that was an electronic replica of the master gear. But in addition to the nominal data for the digital twin, this electronic template also included the "machining specification" – the precise geometry of the gear cutting tool and the motion needed to create the tooth

flanks. Considering all these reasons, KIMoS parameters were preferred and used instead of other methods [9, 19, 20].

G31.75	sym.	Bevel stage		unit
		Pinion	Gear	
Number of teeth	z	9	34	-
Shaft angle	Σ	90		$^{\circ}$
Axial offset	a	31.75		mm
Normal module (tooth center)	m_{mn}	3.988		mm
Normal module	m_{mn}	3.988	3.988	mm
Mean helix angle	β_m	-44.932	20.975	$^{\circ}$
Reference cone angle	δ	24.822	63.155	$^{\circ}$
Tip angle	δ_a	24.822	63.155	$^{\circ}$
Root angle	δ_f	24.822	63.155	$^{\circ}$
Normal pressure angle traction	α_{nz}	17.393		$^{\circ}$
Normal pressure angle thrust	α_{ns}	22.318		$^{\circ}$
Spiral angle pitch direction		left	right	-
Face width	b	31.132	26	mm
Mean reference cone distance	R_m	60.387	81.381	mm
Outer tooth depth	h_e	9.071	9.071	mm
Addendum modification coeff.	x_{hm}	0.455	-0.455	-
Tooth thickness modification factor	x_{sm}	0.039	-0.058	-
Mean normal chordal thickness (KIMOS)	S_{nm}	7.911	4.522	mm
Mean normal circular thickness (ISO 23509)	s_{mn}	7.889	4.49	mm
Mean normal chordal thickness (ISO 23509)	s_{mnc}	7.881	4.49	mm
Mean transvers circular thickness (ISO 23509)	s_{mt}	11.144	4.809	mm
Mean transverse chordal thickness (ISO 23509)	s_{mtc}	11.07	4.809	mm

Table 4.2.1: Gear Geometrical Dimensions for G31.75

Due to the direct import of the XML file which was created by KIMoS, it is not needed to manually import the geometrical gear parameters to SMT Masta. All the main geometrical dimensions of the gear set can be found in the Table 4.2.1.

Different strategies can be followed for modeling other components in the Test Rig. Shafts can be drawn inside the program by adding variations of diameters and corresponding axial length values in each section of the shaft.

At the same time, these components can be easily drawn in the program using 2D drawings. Regarding bearings, they can be standardized in the catalog of the program and can be easily selected and added to the exact position.

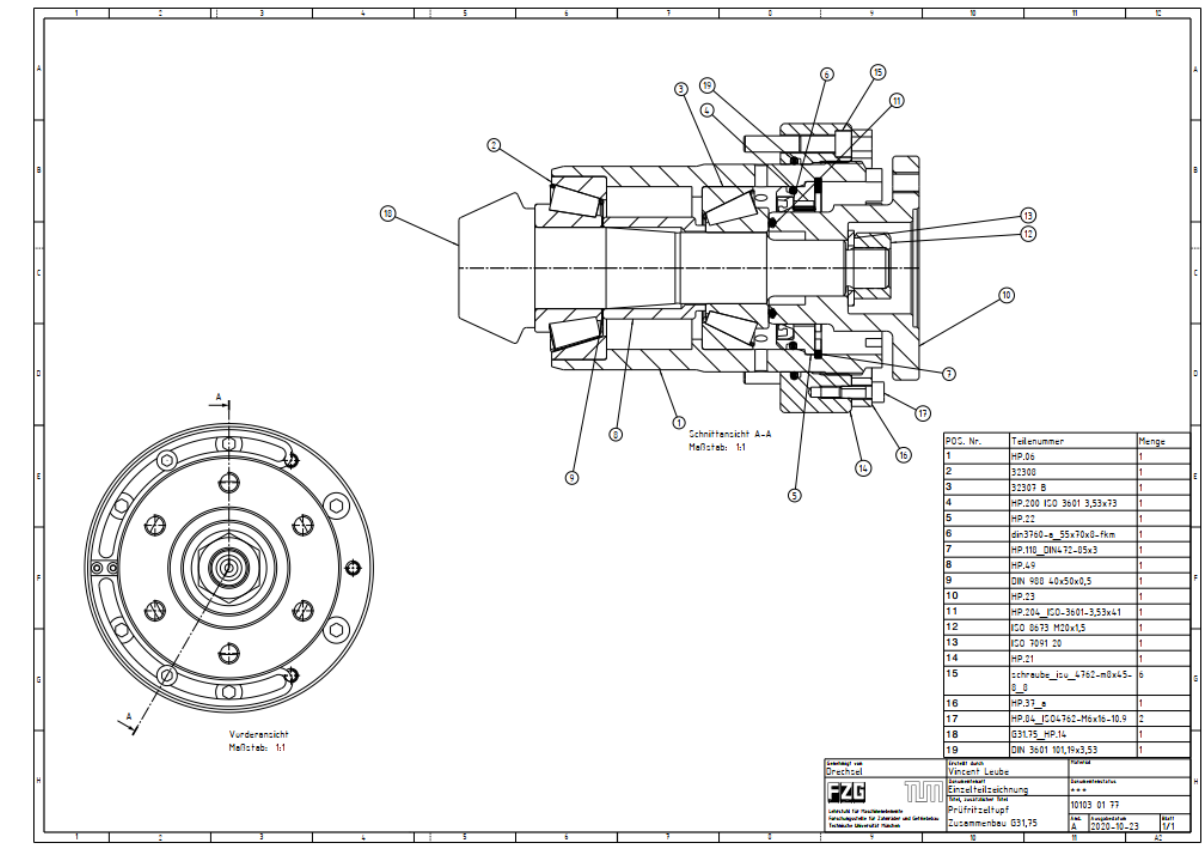


Figure 4.2.3: Test Pinion Housing of G31.75

For example, the pinion shaft in the 2D drawing above was imported into MASTA in DWG format and modeled in MASTA. Similarly, 2D drawings in DWG format were used for other components.

On the other hand, housing geometry is meshed in another FEA software and imported into MASTA. The housing had a careful refinement phase before the meshing process began, during which unnecessary details that weren't necessary for the Finite Element Analysis (FEA) were systematically removed using CATIA software. In the following analyses, this simplified housing representation was used. Ansys and Abaqus were used to carry out the FEA techniques. In order to identify potential differences in outcomes, a systematic strategic approach was used to evaluate the impact of various mesh types. It is important to note that this methodology was thoroughly examined, and despite the thorough investigation of meshing alternatives, no appreciable differences were found among the tested mesh configurations

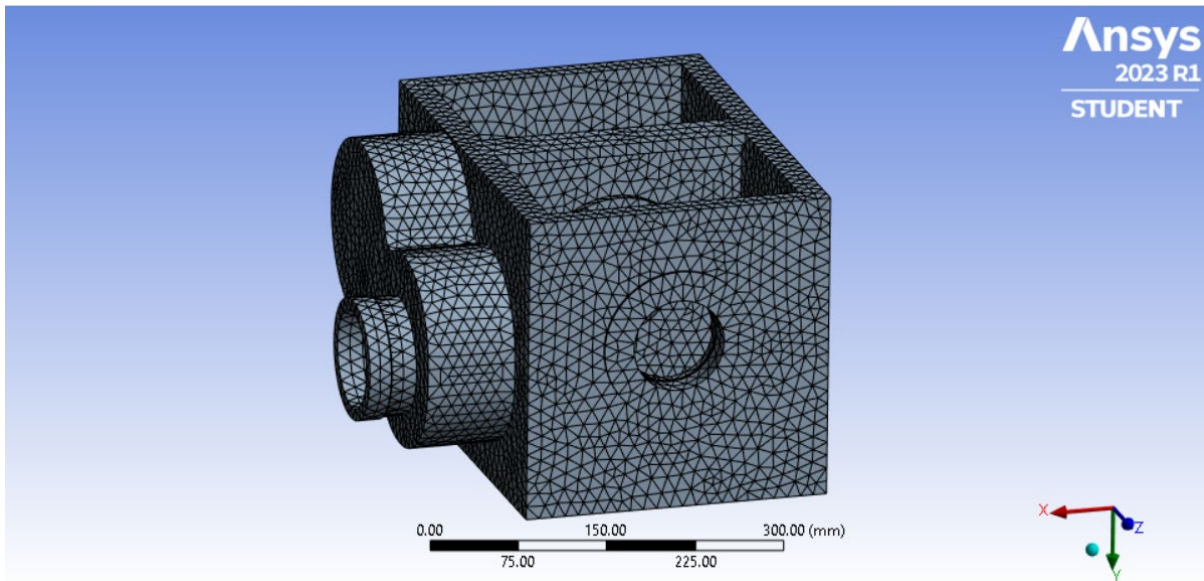


Figure 4.2.4: Meshed Housing(G31.75) in ANSYS

Statistics	
<input type="checkbox"/> Nodes	122411
<input type="checkbox"/> Elements	76270

Figure 4.2.5: Mesh Statistics

Due to the mesh element restriction in ANSYS Student version, a larger number of elements could not be used, but as mentioned before, it does not make a significant difference in the results.

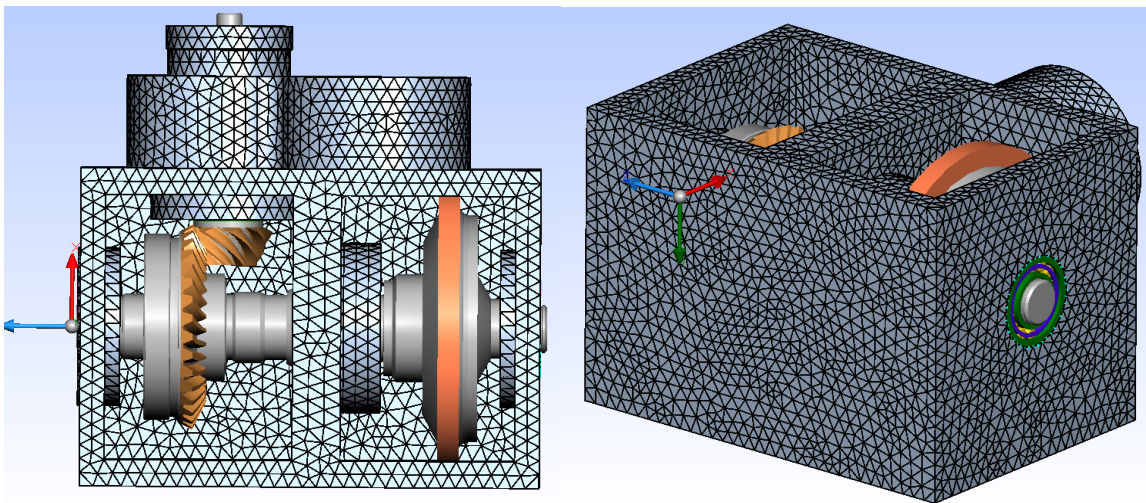


Figure 4.2.6: Meshed Housing (G31.75) in MASTA

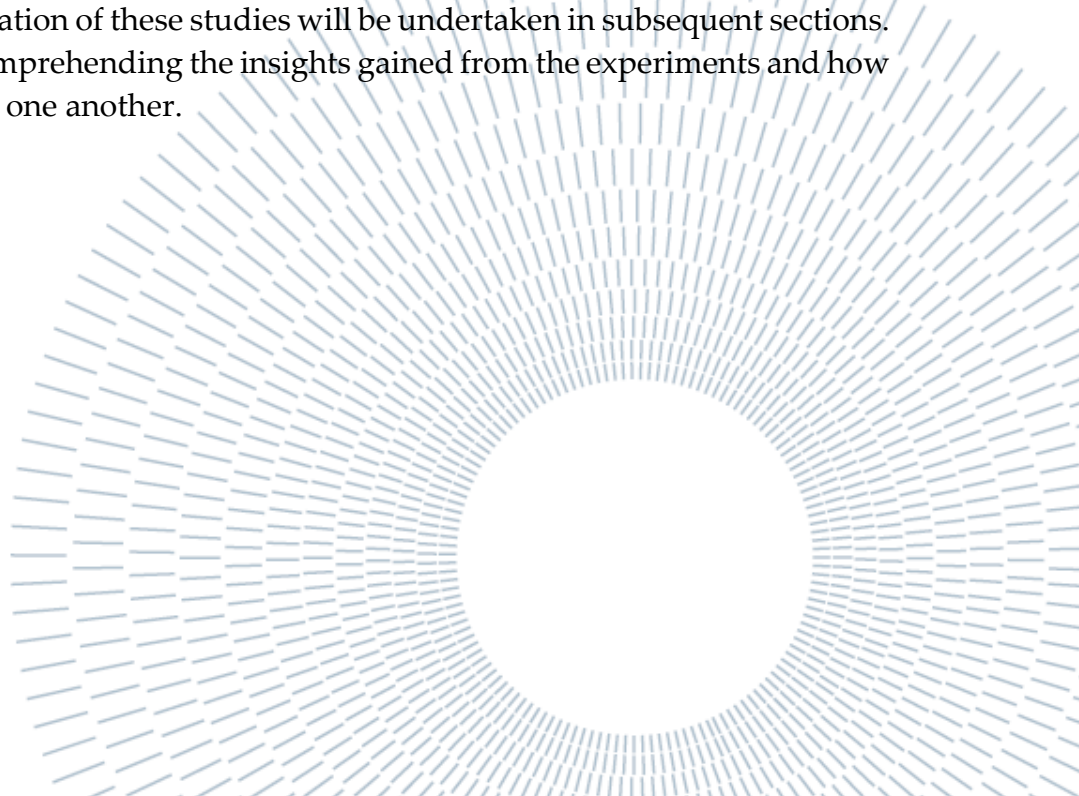
The next step involves automatically setting up condensation nodes and connecting them to the MASTA model after the ANSYS model has been imported. The workflow for analysis and simulation will be streamlined as a result of the integration of ANSYS and MASTA, which will increase the effectiveness of the entire engineering process.

The connection between the MASTA internal model and the Finite Element (FE) model provides a variety of adaptable customization options. These links can be modified by engineers to meet the specific needs of the analysis. The options include a variety of possibilities, including attaching to an existing condensation node set up in an external FE package, establishing new axial nodes, generating nodes at particular angles or diameters for focused analysis, and even creating a flexible node ring to accommodate intricate contact points.

MASTA automatically chooses the regions on the imported FE model that are linked to the internal model by default. The initial integration process is made simpler by this thoughtful default setting. However, MASTA also gives users access to controls that let them customize these connections based on their knowledge and preferences.

It is possible to combine the strength of finite element analysis with the capabilities of MASTA internal modeling thanks to the integration between ANSYS and MASTA. In addition to improving simulation accuracy, this integrated approach gives engineers the freedom to delve deeper into particular parts and how they interact with the larger mechanical system. But it is important to note that the full stiffness matrix obtained in ANSYS has been reduced again with MASTA according to the required requirements.

The introduction of virtual modeling for the test rig has transformed the field of laboratory testing by making it possible to simulate real-world experiments in a digital environment. This makes it easier in identifying uncertainties as well as how certain variables affect the final results. Following the interpretation of LTCA analyses with BECAL, further exploration of these studies will be undertaken in subsequent sections. This step will aid in comprehending the insights gained from the experiments and how each detail aligns with one another.



4.3 Simulation Results of Model

The input load, which is applied at the starting of pinion shaft, is selected as one of two main input parameters of the simulation. It is given in terms of torque quantity and values are changed from 100 Nm to 700 Nm in order to analyze the relevant output parameters of the test rig under different torques. Meanwhile, bearings on the pinion shaft, are loaded with various preloading amounts and the preloading quantity is selected as another input parameter. SMT MASTA software allows applying different preloading values to any type of bearing selected from bearing library, in terms of μm . There are two bearings on the pinion shaft. Both bearings are loaded with the same preloading at every step and the value is changed between 0 μm and 200 μm in order to identify the influence of preloading of bearings on results.

Regarding the outputs of the simulation model, the misalignments of the gear set can be directly obtained from the simulation report. In SMT MASTA software, misalignments of gear sets are classified with four main components, as shown on Fig 4.3.1. The first two are related to axial displacement of wheel and pinion. Subsequently, wheel radial displacement which is defined as the displacement of it in perpendicular direction to pinion, can be considered the next misalignment component. Finally, the shaft angle which is identified as the angle between pinion and wheel axes, is the other misalignment type. These misalignments are aimed to be used as input parameters for LTCA analysis on the BECAL program in the following steps.

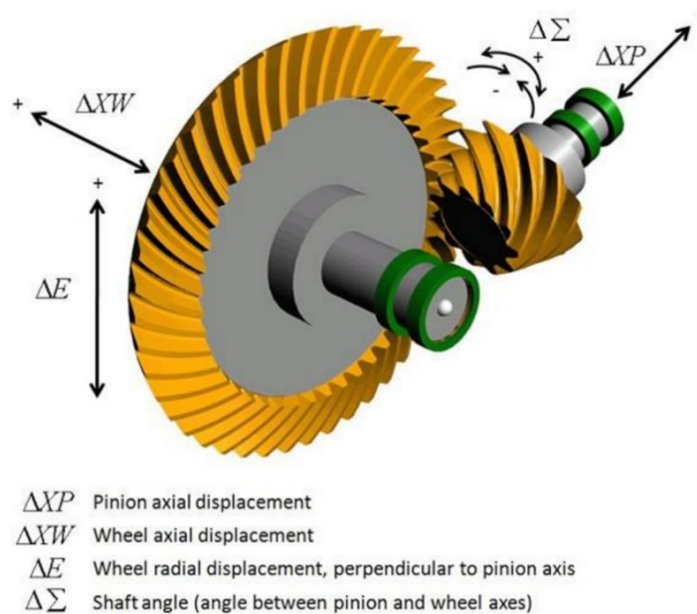


Figure 4.3.1: Misalignment Representation on MASTA [28]

For all torque steps and preloading values at every torque level, all four misalignment values are exported from simulation results and plotted in order to identify the influences of variation of input torque and variation of preloading on pinion shaft bearings on misalignments of gear set. Except for shaft angle, other three misalignments are obtained in terms of μm , while the shaft angle can be received with degree and then be converted into mrad. The reason why mrad is preferred for unit of shaft angle, is that shaft angle values have to be imported into BECAL program in terms of this unit. All four plotting can be seen in Fig 4.3.2.

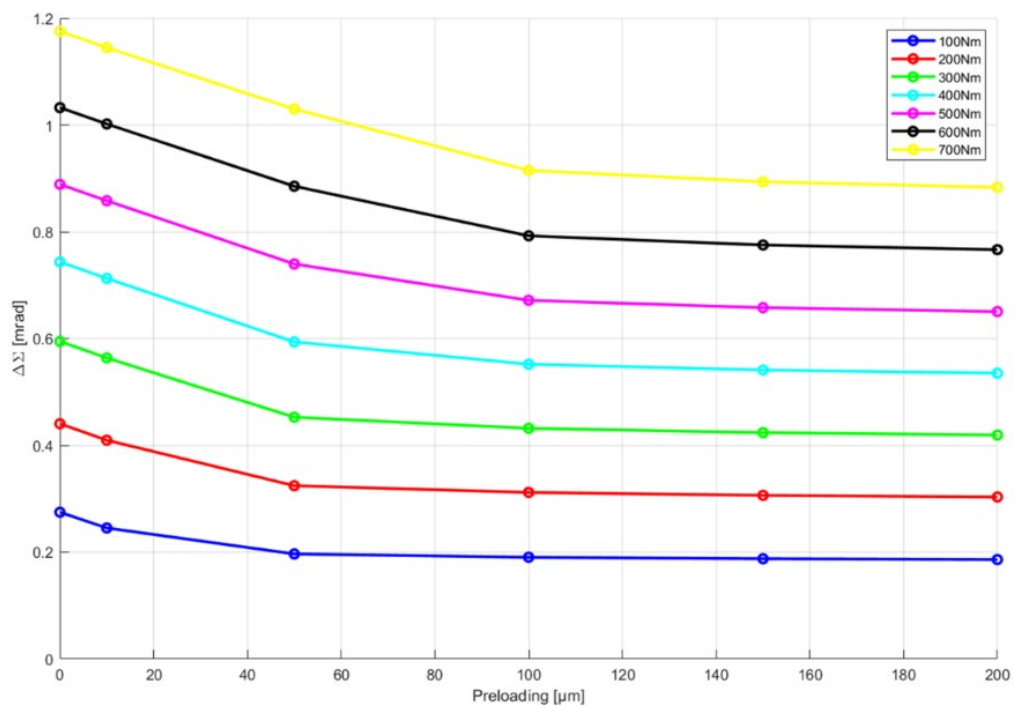


Figure 4.3.2: Variation of Shaft angle with respect to different preloading values on pinion shaft bearings, under varying input torque quantities

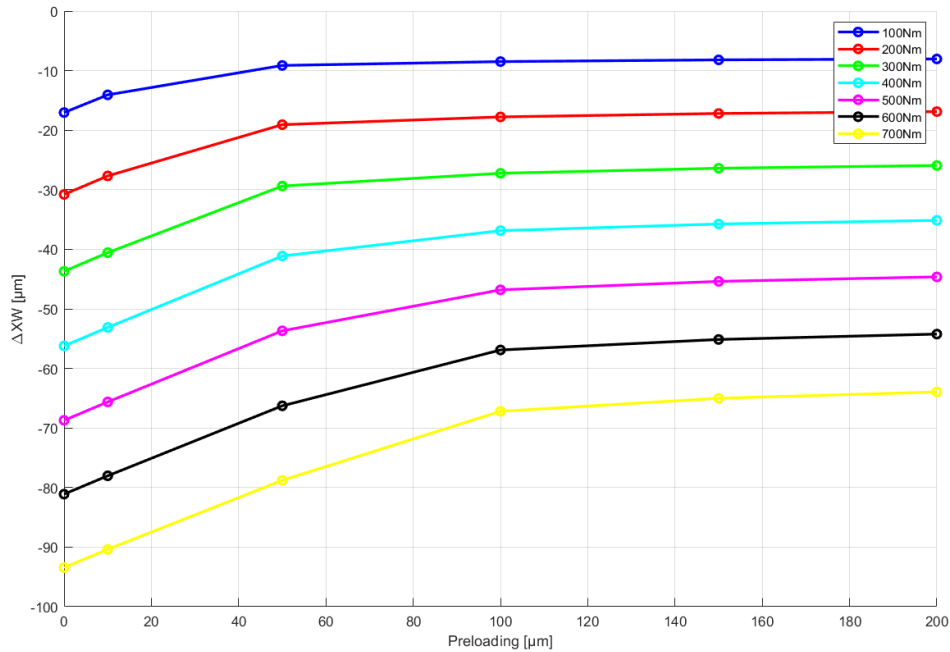


Figure 4.3.3: Variation of Wheel axial displacement with respect to different preloading values on pinion shaft bearings, under varying input torque quantities

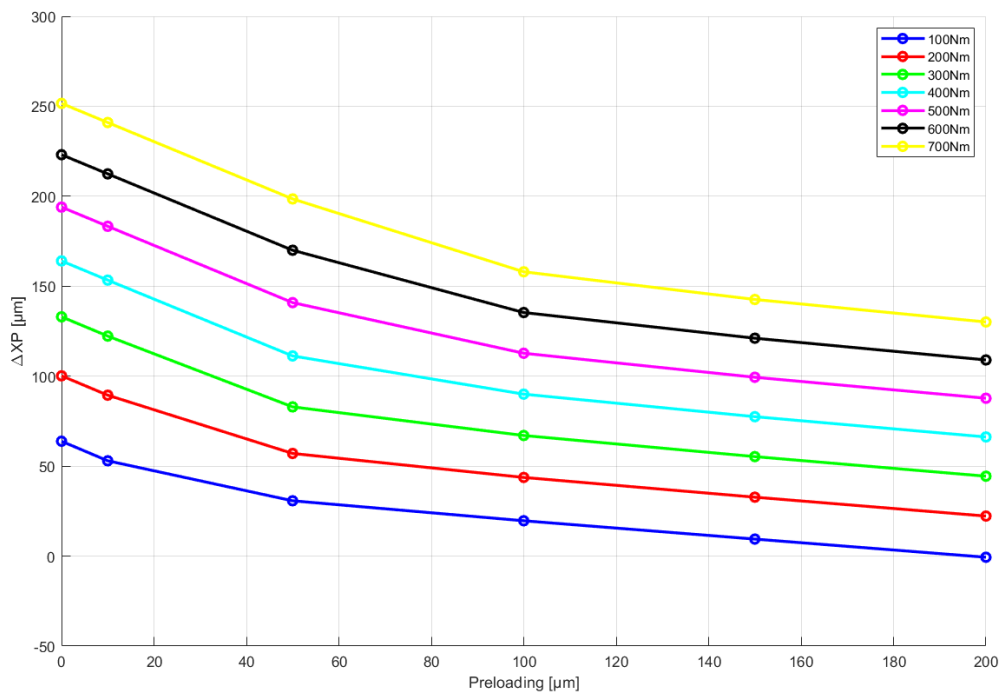


Figure 4.3.4 : Variation of pinion axial displacement with respect to different preloading values on pinion shaft bearings, under varying input torque quantities

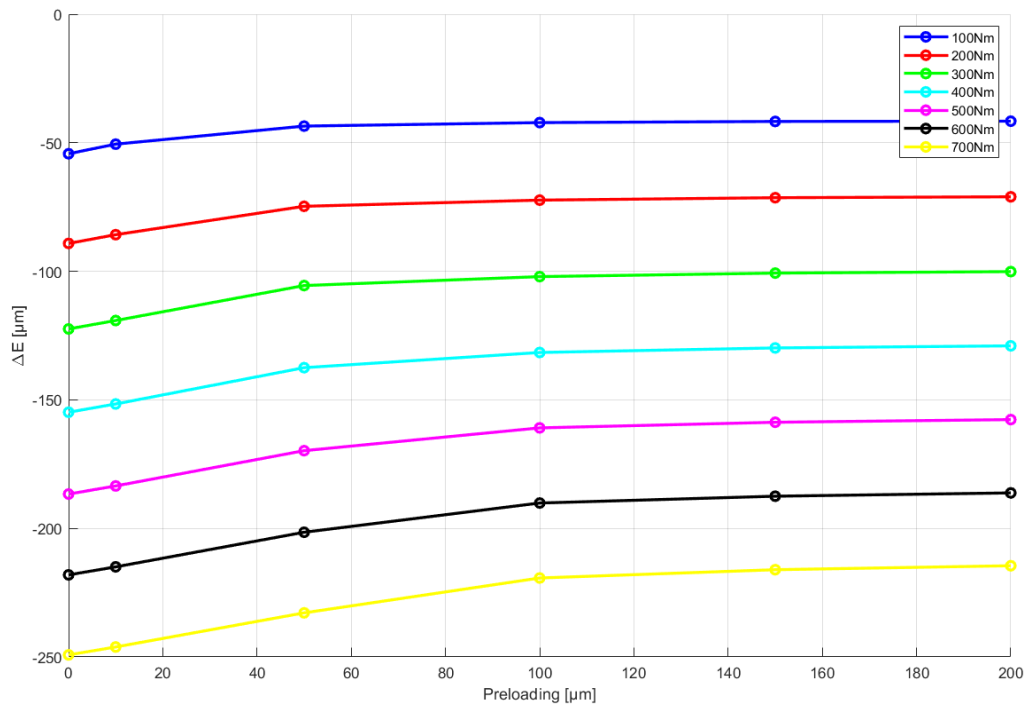


Figure 4.3.5: Variation of Wheel radial displacement with respect to different preloading values on pinion shaft bearings, under varying input torque quantities

According to simulation results, it can be observed that under all loading and preloading conditions, and particular gear spiral hands (RH for wheel and LH for pinion), pinion axial displacement is positive, whereas that of wheel is negative. Meaning that, pinion is separated from wheel in its axial direction, while wheel is displaced axially towards the pinion. Regarding wheel displacement, it is always negative and leads to displacement of wheel in downward direction.

Analyzing the trend of misalignments, it can be observed that for increasing input torque values, absolute values of all four misalignment components become greater and greater. Obviously, loading the system with higher torques will lead to higher deflection of wheel and pinion in both radial and axial directions. On the other hand, the increase of preloading on pinion shaft bearings results in decrease in all misalignments. This trend can be explained by increased rigidity of pinion shaft and pinion under higher preloading of bearings. However, after certain preloading of bearings, every misalignment gets converged at a particular value and does not decrease as sharply as initially. This concludes that excessive increase of preloading on bearings does not contribute to rigidity of gear set contact pattern after one point.

Regarding the validation of the simulation results, reference can be made to other simulation outputs obtained at FZG studies carried out about 10 years ago. While plotting those results and one currently obtained simulation output set at a particular

preloading on pinion shaft bearings, it can be noticed in Fig. 4.3.6 that the trend of variation of misalignment with respect to input torque is completely similar (linear increase). This highly identical results further confirms that current simulation results can be considered sufficiently reliable for LTCA analyses.

Furthermore, the change in misalignments with respect to input torque can be obtained for various preloading values on pinion shaft bearings. As it is observed in Fig. 4.3.7, all variation trends are linearly climbing, while higher preloading contributes to lower misalignment of gear sets.

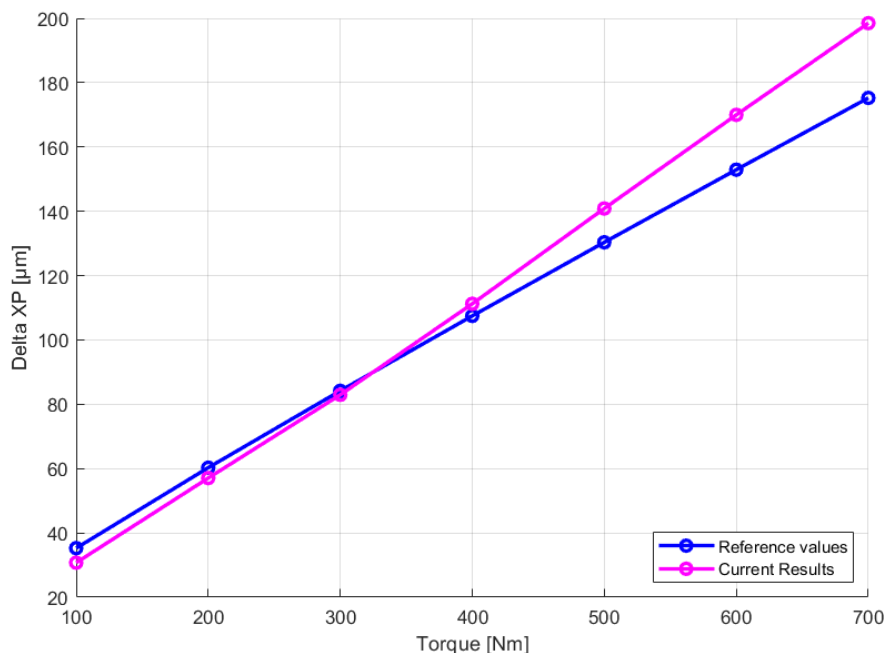


Figure 4.3.6: Comparison between reference results and current simulation results

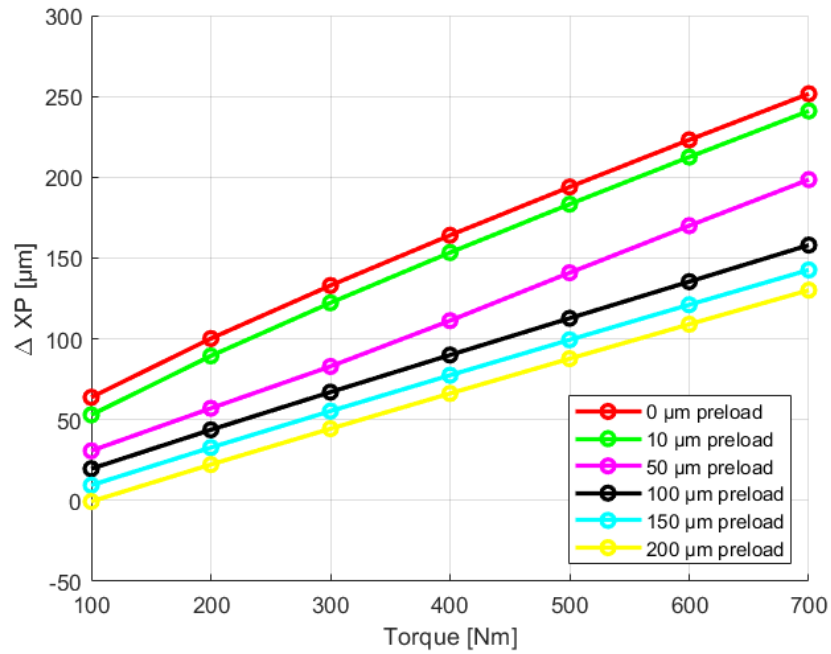
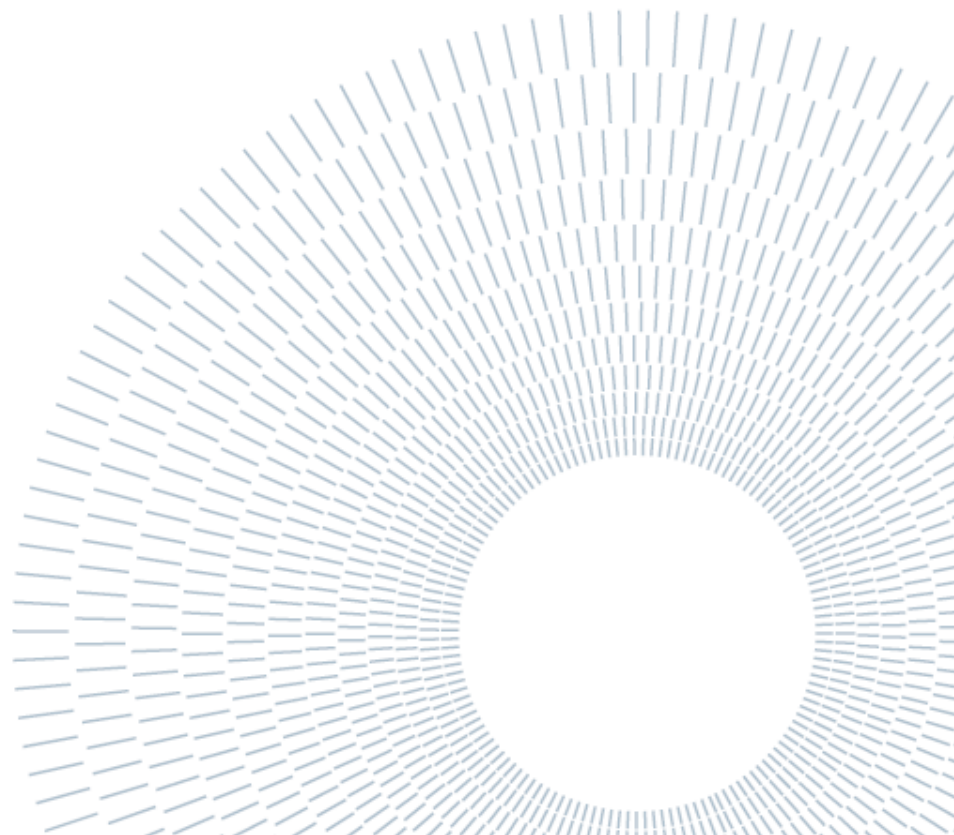


Figure 4.3.7: Variation of pinion axial displacement with respect to input torque on pinion shaft bearings, under varying preloading on pinion shaft bearings



5. Loaded Tooth Contact Analysis

Problem Definition: In the context of this study, the problem at hand revolves around the intricate interplay of factors influencing gear system behavior, particularly focusing on the shifting of contact patterns in bevel and hypoid gears. In line with this objective, the modeling efforts in Chapter 4 have been conducted, and the endeavors undertaken for further research are explained within this section. Loaded Tooth Contact Analysis (LTCA) refers to a computational method employed in engineering to analyze the behavior of gear systems under operational conditions. In LTCA, the interactions between meshing gears teeth are investigated while considering the loads, torques, and deformations those gears endure while in use. This analysis offers perceptions into important aspects of the gear system, such as contact patterns, stress distribution, and deflections, assisting in the assessment of gear performance, durability, and reliability. Engineers can optimize gear designs, anticipate potential problems, and guarantee the best gear system performance by simulating the dynamic interactions of gears under load.

In summary, this section of the thesis seeks to comprehensively address the impact of variables such as torque fluctuation, preloading on pinion shaft bearings on location of contact pattern, ultimately aiming to enhance the understanding of gear performance and reliability in diverse operational scenarios.

5.1 Introduction to BECAL (BEvel gear CALculation) Software

For bevel gear calculations, the Common ISO, DIN, or AGMA standards, ship classification society specifications, and FVA calculations are used in simple methods. The objective of bevel gear design is to increase load capacity while also increasing efficiency and power density. To fulfill these requirements, BECAL (BEvel gear CALculation) was established by the TU Dresden, Institute of Machine Elements and Machine Design (IMM) and Institute of Geometry for the Forschungsvereinigung Antriebstechnik e.V. (FVA). A complex tooth contact simulation of hypoid, spiral, and helical bevel gears is implemented in BECAL to analyze load capacity and gear design. At IMM, BECAL is continuously developed and maintained. With the help of member contributions and public funding, the FVA organized a annual budget of 17 million euros, allowing them to undertake research projects in collaboration with renowned German universities, chairs, and research institutions. According to information from

the FVA, The calculations implemented in the FVA-Workbench were developed, analyzed, and validated through research projects conducted by the Research Association for Drive Technology (FVA) [30].



Figure 5.1.1: BECAL FVA [18]

Different methods have been developed for different purposes in FVA Research Projects, some of these projects are as follows [18]:

- FVA 223 XX Numerical stress calculation on CAD models in BECAL (CAD2BECAL)
- FVA 223 XVIII Calculation of backlash under load of bevel and hypoid gears in BECAL
- FVA 223 XXI Test evaluation and documentation for I4.0
- FVA 732 II Local tooth root stress in RIKOR
- Lapping simulation
- FVA 223 XVI Integration of the stiffness of complex wheel bodies in the load distribution calculation
- FVA 223 XV Measurement of the contact pattern on bevel gears
- FVA 223 XIV Processing of measurement data in FVA Workbench
- FVA 223 XIII Integration of ISO 23509 in BECAL and FVA Workbench
- FVA 223 XII Simulating the increasing damage of micropitting and pitting for bevel and hypoid gears

- FVA 223 XI Investigations and extensions regarding the complex BECAL stress and strain model

As a result, BECAL is a software that is continuously developed according to the desired and targeted purposes. The module utilized for this thesis is the "Bevel mesh: Advanced gear calculations" within the BECAL software.

5.2 Processing of Simulation Results on BECAL LTCA Analysis

For importing the simulation results from the previous step into the BECAL program, only a single notepad file was used. It was modified for all possible input torque and preloading combinations. Other files, regarding description of material parameters, microgeometry of flank surface and so on, are maintained the same for all different BECAL analyses. The description of each part of the modified input file is explained below:

To begin with, misalignment values right after installation process, are introduced in the initial rows. The classification of gear set misalignments at BECAL software, is consistent with those at MASTA. Therefore, the same four components of misalignments are taken into consideration at BECAL too. It is assumed that contact pattern is perfectly accumulated in the middle of the flank surfaces of gear set components after installation of wheel and pinion. Therefore, all four misalignment values are set to zero. Meanwhile, for perfect consistency of LTCA analysis results from BECAL and experimental test outputs, the relevant installation techniques are used for the maximum accumulation of contact pattern on the middle of flank surfaces. There is a detailed description of these in the relevant chapters of the thesis.

```
$ Einbaumasabweichung ( Installation Misalignments )
Axiale_Verschiebung_Ritzel ( Pinion Axial Displacement ) = 0.00000
Axiale_Verschiebung_Rad ( Wheel Axial Displacement ) = 0.00000
Achsversetzungs-Abweichung ( Wheel Radial Displacement )= 0.00000
Achswinkel-Abweichung ( Shaft Angle )|= 0.00000
```

Figure 5.2.1: Becal Input 1

Subsequently, in "Load dependent Misalignments", it is required to input all torque values in adjacent order with corresponding misalignment values. Therefore, torque values from 100 Nm to 700 Nm are introduced sequentially and all four misalignment values under different torque quantities, are entered. This process is repeated for all preloading combinations, as misalignments change for varying preloading values

under the same input torque. The shaft angle is inputted in terms of mrad, while μm is used for the other misalignments. Below, the introduction of misalignment values under no preloading on pinion shaft bearings, is illustrated as an example.

```

$ Belastungsabhaengige_Relativlage_Zug (Load dependent misalignments)
Variationen_Anzahl ( variation Number)= 7
Drehmoment_Treiber (Torque) = 100.0 200.00 300.00 400.00 500.00 600.0 700.00
Axiale_Verschiebung_Ritzel ( Pinion Axial Displacement ) = 0.0638408 0.1001909 0.1329931 0.1640496 0.1939592 0.2230772 0.2515987
Axiale_Verschiebung_Rad ( Wheel Axial Displacement ) = -0.0170433 -0.0307970 -0.0436898 -0.0562207 -0.0687171 -0.0811100 -0.0934450
Achsversetzungs-Abweichung ( Wheel Radial Displacement ) =-0.0542793 -0.0891615 -0.122418 -0.154815 -0.186641 -0.218078 -0.2492
Achswinkel-Abweichung ( Shaft Angle ) = 0.0157 0.0252 0.0341 0.0426 0.0509 0.0592 0.0673

```

Figure 5.2.2: Becal Input 2

Following this, operating data values are introduced to the file. In all analyses, the circumferential speed of the test cycle is selected as 4500 rpm which is identical to parameter of real experimental testing. Regarding torque value, all LTCA calculations were carried out for 400 Nm, due to that one real experiment was already done for 400 Nm and results were appropriately documented before starting LTCA analyses. It was aimed to compare LTCA analysis and real experimental test results for 400Nm. In case of lack of sufficient comparison, it might be feasible to carry out LTCA results for other torque values and compare with corresponding test results. The more detailed information about all operating data can be found below in Fig 5.2.3.

```

$ Betriebsdaten (Operating Data)

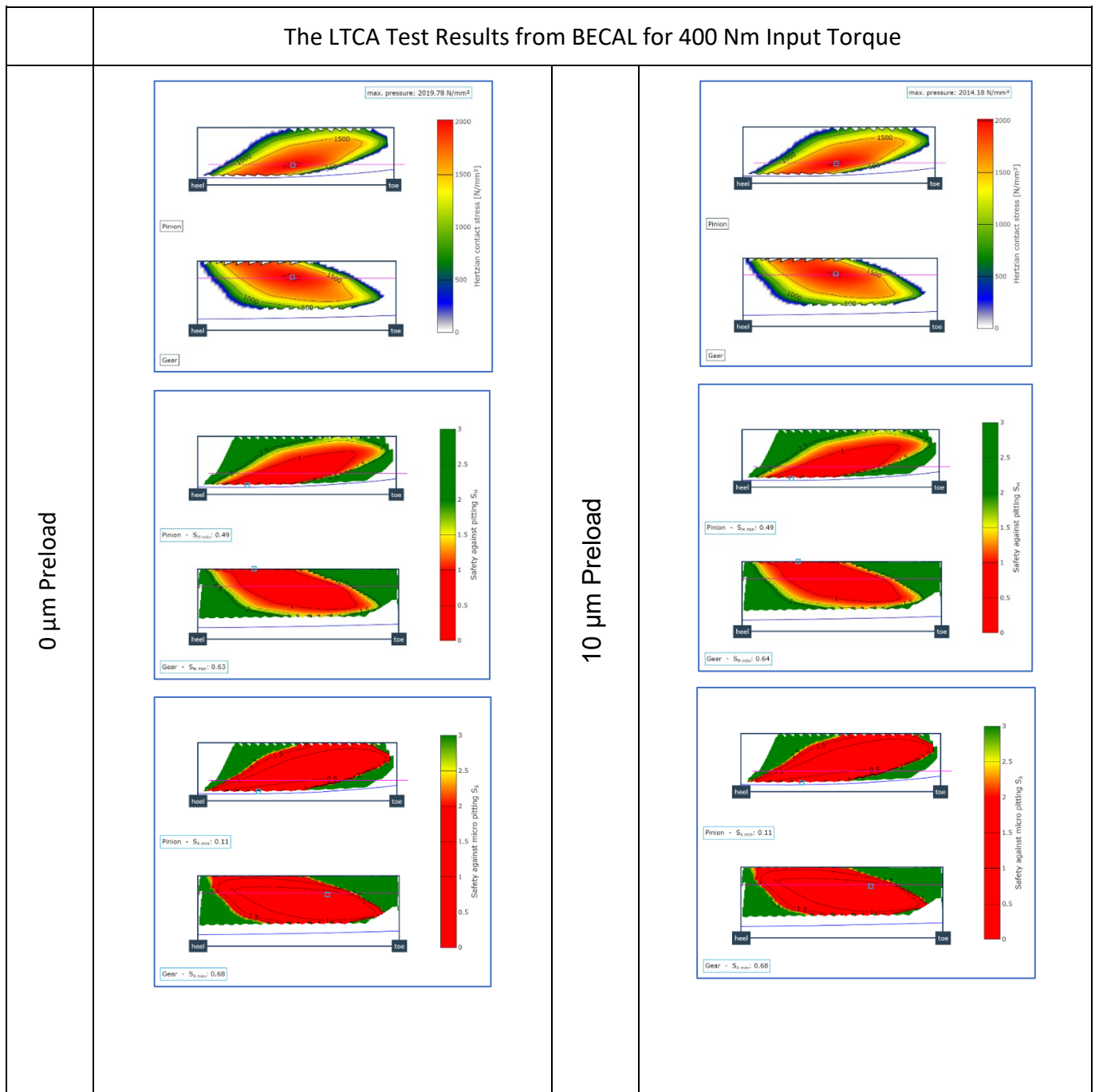
Betriebsart (Operating Mode) = 2
Lastwechselzahl_Zug (Number of Load Cycles) = 50000000.00
Drehzahl_Zug (RPM) = 4500.00
Drehmoment_Zug (Torque) = 400.00
Treibart_Zug (Drive Type) = 1
Betriebsstunden_Zug (Operating Hours) = 1.00

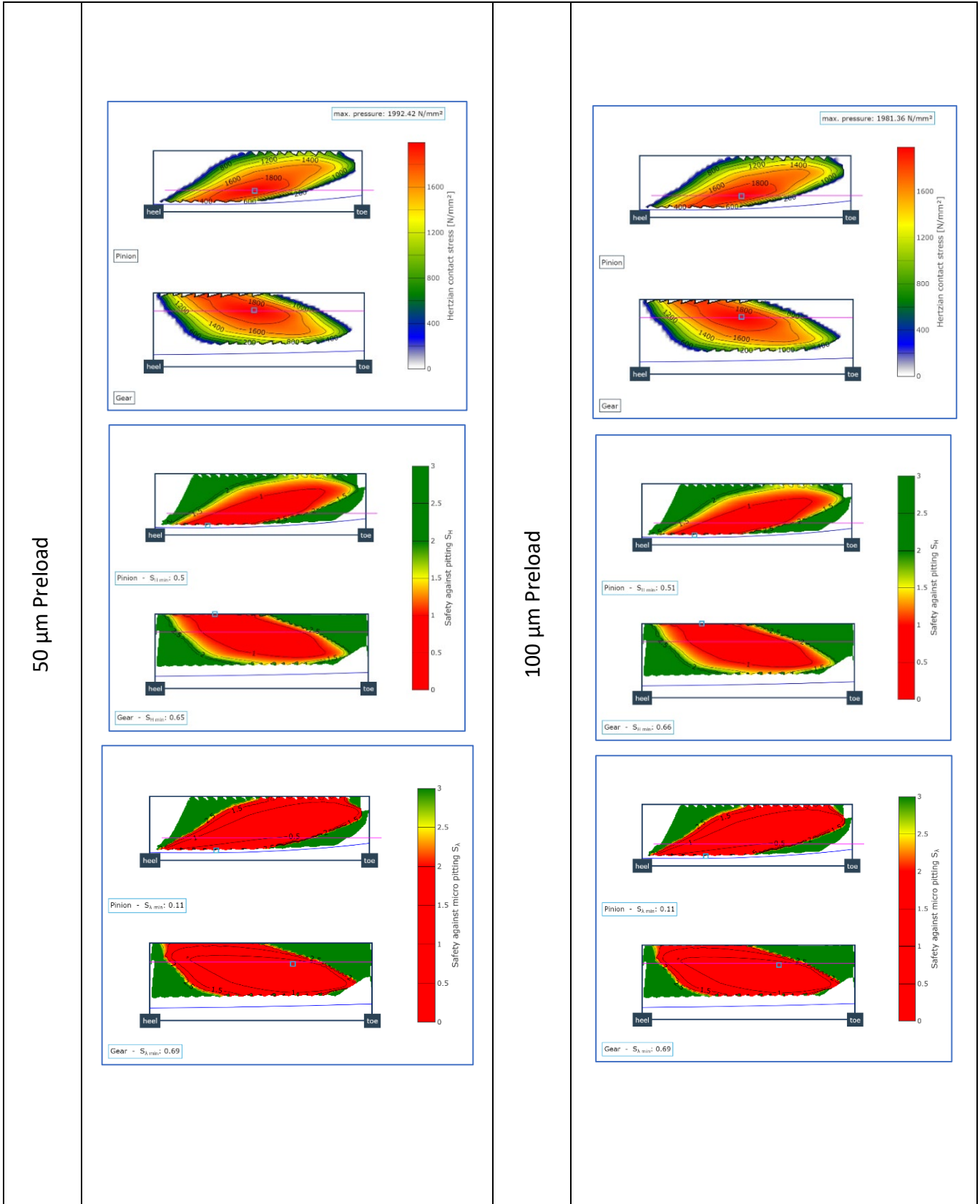
```

Figure 5.2.3: Becal Input 3

5.3 LTCA Results

After performing LTCA analyses with the BECAL software, a number of notable findings are made available. Some findings and conclusions have been drawn from these table. Details are provided in the following section.





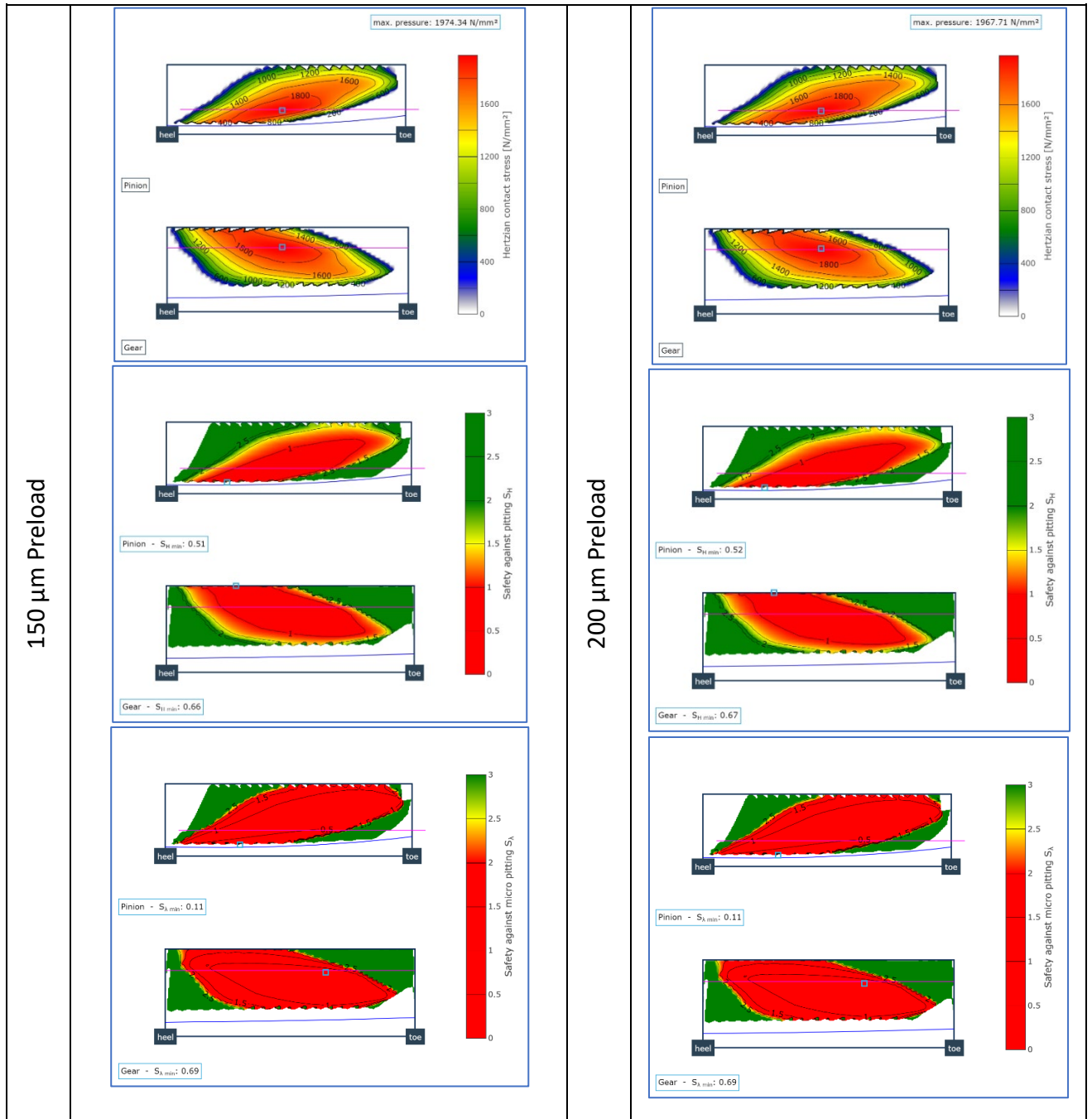


Table 5.3.1: BECAL 400 Nm test results for different preload values

The results that give values for various output parameters, providing a thorough understanding of the behaviour of the gear system. The distribution of flank pressure (contact pattern) and safety margins for macropitting and micropitting are also shown in the following visual representations, such as graphs and charts. These visuals give

an understanding of how the gear behaves under various preloading conditions, assisting in a thorough evaluation of its performance and reliability under various operational circumstances.

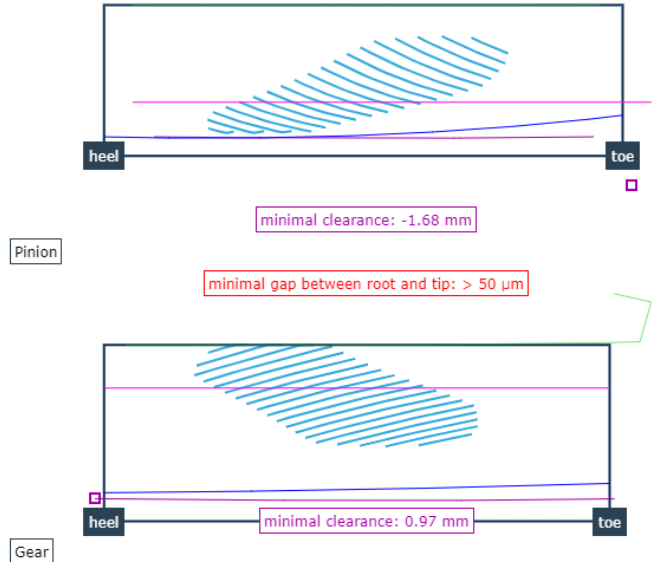
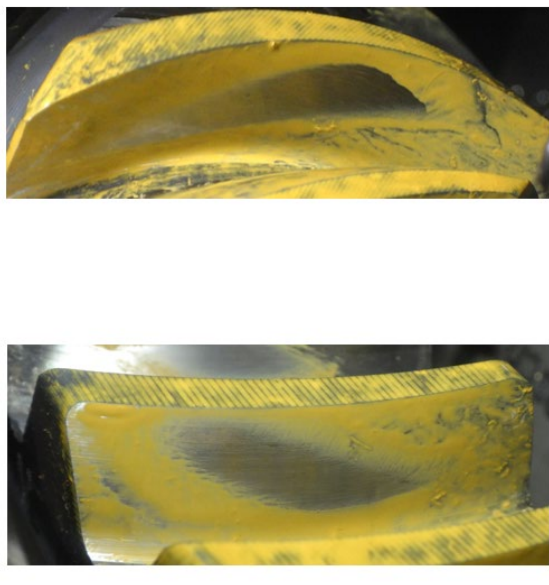
<p style="writing-mode: vertical-rl; transform: rotate(180deg);">BECAL Contact Pattern</p>	 <p>Pinion</p> <p>minimal clearance: -1.68 mm</p> <p>minimal gap between root and tip: > 50 μm</p> <p>Gear</p> <p>minimal clearance: 0.97 mm</p>
<p style="writing-mode: vertical-rl; transform: rotate(180deg);">Actual Contact Pattern</p>	 <p>Pinion</p> <p>Gear</p>

Table 5.3.2: BECAL Result & Actual Contact Pattern

Experimental test results presented in section 3, can be used in validation of LTCA analysis results at BECAL. Table 5.3.2 illustrates both experimental (actual) results before occurrence of micropitting and LTCA results in terms of contact patterns.

Comparing these two sets of outputs, the distribution of flank pressure on gear flanks are considerably identical to each other on both results, for pinion and wheel. Therefore, it leads to validation of BECAL outputs and makes their usage feasible for conclusion regarding the influence of two defined factors on experimental results.

5.3.1 The Effect of Variation of Preloading on Pinion Shaft Bearings on Contact Pattern

At the end of LTCA analyses, the distribution of flank pressure on the flank surface, and the precise location of the contact pattern can be received. Moreover, the maximum contact pressure value can be obtained on its exact location. The maximum flank pressure values are varying with different preloading on pinion shaft bearings. This variation trend can be plotted as shown in Fig 5.3.1. According to this plotting, there is a sharp decrease for smaller preloading values on the largest flank pressure, whereas it is followed by a continuous convergence for higher preloading values.

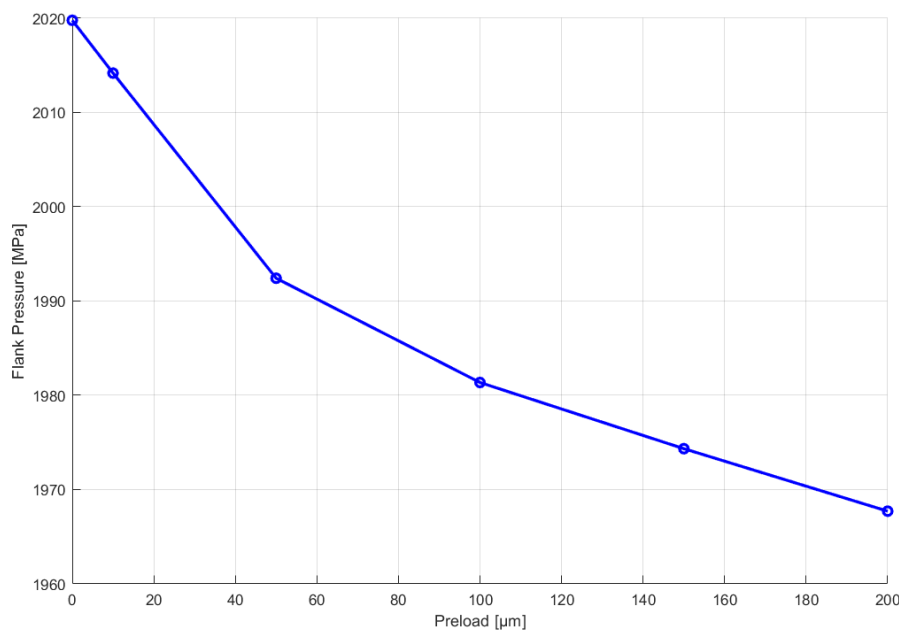


Figure 5.3.1: The maximum flank pressure variation with respect to preloading on pinion shaft bearings

According to the Fig 5.3.1, under the same input torque (400 Nm), there is not a huge difference in the highest pressures on flank surface for different preloading values. Meanwhile, it can be noticed that the total variation of preloading on pinion shaft bearings from 0 to 200 μm , contributes to only an approximately 52 MPa change in maximum flank pressure from 2020 MPa to 1968 MPa. It corresponds to only 2% of the

average value of all maximum flank pressures. Moreover, while observing the contact pattern distribution on the flank surface for different preloading conditions, there is not an easily noticeable shift in contact pattern location. In other words, even if the exact location of them are not completely identical for all preloading cases, there is only a negligible variation in the contact pattern location, which cannot be noticed by eye looking and can be easily ignored. This concludes that variation of preloading on pinion shaft bearings cannot be considered as the dominant effect on shifting of contact pattern on flank surface. In the next chapters, other possible impacts will be taken into account.

5.3.2 The Effect of Slight Torque Fluctuation on Contact Pattern

In the real experiments, there is a continuous torque drop in the cycle from the beginning to final cycles of the entire test duration. This continuous torque decrease which is affected by several misleading effects, does not allow to experimentally test the gear set under the certain constant torque value. In other words, the slight fluctuation on input torque quantities are considered the possible influence on the shifting on contact pattern. Therefore, LTCA analyses are calculated in the similar way for 390 Nm and 410 Nm in order to analyze the effect of ± 10 Nm variation of input torque on contact pattern. Similarly, the maximum flank pressures are directly achieved from LTCA results and plotted with respect to various preloading values. The variation of maximum flank pressure with respect to preloading values under three different input torque, can be observed below:

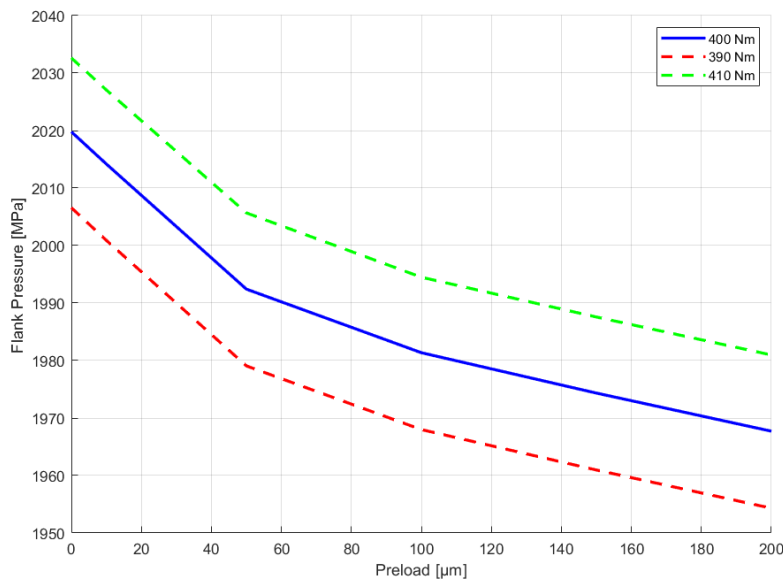


Figure 5.3.2 : Flank pressure variation with respect to preloading on pinion shaft bearings for different torque values

From the Fig 5.3.2, it can be calculated that for all preloading values, 10 Nm torque fluctuation corresponds to a modest 13 MPa flank pressure variation. This small deflection in flank pressure is roughly 0.6% percent of average value of maximum flank pressure values. From the engineering point of view, it can be explained that for all preloading conditions, the gear set is elastically loaded and there is almost no effect of preloading on elastic region.

In Table 5.3.3, the exact location of contact pattern for three different torque values (390 Nm, 400 Nm, 410 Nm) are seen for several preloading conditions on pinion shaft bearings. Due to negligible difference in position of contact patten on flank surface, it can be commented that there is not a significantly high effect of slight torque fluctuation on shifting of contact pattern. As a result, an non-uniform change in torque quantities, cannot be taken into account as a substantial influence on not accumulation of contact pattern on the middle of the flank surface.

Preloading on Pinion Shaft Bearings (μm)	390 Nm	400 Nm	410 Nm
0			
10			
50			

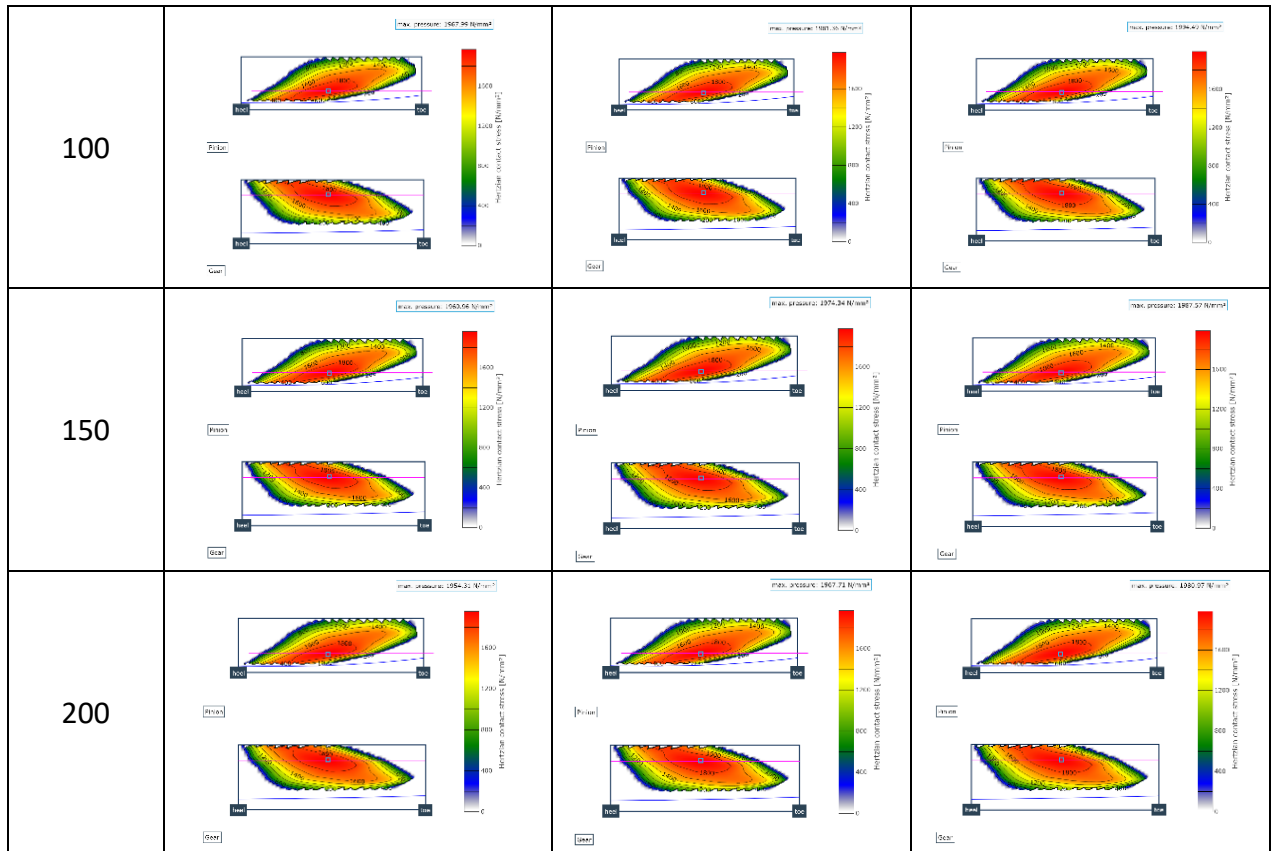


Table 5.3.3: Preloading on Pinion Shaft Bearings (μm)

6. Sensitivity Analysis of the Torque Measurement System of the FZG Hypoid Test Rig

Although the input load and slight fluctuations of it were not considered the primary factor on the scatter of the experimental results, according to the LTCA results; there can still be a concern regarding applied torque. In other words, there might be a need to check whether the applied torque to the test cycle by the appropriate tools is identical to the displayed torque on the measurement system. Therefore, it is needed to carry out a relevant sensitivity analysis to determine how accurate the torque measurement system is. As a result, the following study aims to address the complex issues related to precision and accuracy in torque measurements in the field of torque measurement calibration, particularly within the framework of DIN 51309 [3] standards. This investigation's main goal is to strategically use a lever-mass system to rigorously quantify the complex uncertainties related to calibration results. This study attempts to meticulously separate and comprehend the influential factors that contribute to measurement errors by carefully arranging the loading and unloading of a torque measurement system using meticulously calibrated weights. Critical elements like resolution, repeatability, reproducibility, interpolation, and zero-point deviations are all included in these variables. Also, the study seeks to develop a thorough understanding of the measurement uncertainties present with GUM in the calibration process, ultimately resulting in improved torque measurement accuracy in a variety of applications. The details provided in this section are from reference sources [3, 4, 5, 6, 15, 16, 22, 23, 24, 27, 29, 34, 35]. However, the foundation for the studies and data in the whole section 6 can be traced back to Weber, M. (2019), who conducted doctoral research on calibration and measurement uncertainty in a hypoid efficiency test rig [35].

6.1 State of Art of the Calibration Procedure

6.1.1 Definition of Calibration

The International Vocabulary of Metrology [16] defines calibration as a process that, under specific circumstances, first establishes a relationship between corresponding indications with associated measurement uncertainties and quantity values with measurement uncertainties provided by measurement standards. This data is then employed in a subsequent phase to create a relationship that enables the acquisition of a measurement result from a display.

The calibration of the torque measurement system on the FZG hypoid test rig was substantially inspired by the process outlined in DIN-51309 [3] standards. More information on this will be provided below. The calibration of torque measuring instruments for general applications, such as dynamometers, is included in the scope of this standard in addition to the static calibration of torque measuring instruments for materials testing equipment [3].

6.1.2 General Information on Torque Measurement Instrument Calibration

To calibrate the torque measurement equipment, calibration torques (M_k) are applied. The values shown throughout this process are noted. The following requirements for safety must be followed: [3]

- Each input component used to connect the torque measurement device to the calibration equipment, has to be sufficiently safe to transmit, at least 1.5 times the maximum torque to be calibrated.
- The encod axial length change, including all adapters, cannot be greater than 1 mm.
- When the maximum moment is applied and interference, such as transverse forces or bending, is overlaid, only adaption parts may be employed whose maximum stress stays below 1.2 times the stress without interference.

An overload test must also be carried out before the calibration procedure is started. The encoder must be loaded with at least the nominal torque plus 8% to 12% during this test. Over the course of one to one and a half minutes, this load must be delivered at least four times [3].

6.1.3 Preparations

Before calibration, a number of preparations are required.

Before putting the unloaded transducer in the calibration setup, if at all possible, a reading should be taken from it. The torque transducer needs to be vertical in order to calculate the transducer zero value I_s . One can infer information about the transducer's history and its stability over time from the time history of the zero value of the transducer [3].

The transducer display must be set up in line with the relevant specifications. Prior to calibration, the display device's zero stability must be examined. Logging of all variable settings is required. The indicator must be wired so that an increase in clockwise torque results in an increase in the positive display value [3].

It has to be checked that the temperature difference between the environment and the measurement system is equal before calibrating. The power supply must be applied in order to attain this equilibrium. The ambient temperature, the time, and the time must all be noted in the log before and after each set of readings. The temperature must range from 18°C to 28°C and must be constant within a range of 1K. It is imperative to prevent at all costs temperature gradients brought on by supply media such as cooling water or compressed air since they are not acceptable [3].

6.1.4 Performing the Calibration

There are two methods for calibrating torque measurement systems:

- As a typical lever-mass system, a purely static calibration with distinct torques
- As is customary for calibration using reference torque transducers in comparison operations, continuous (quasi-static) calibration involves a continuous process without dwell time

The calibration results from the two approaches could differ as a result of creep effects. As a result, the method selection should be based on how the measurement system will be used. In both situations, the calibration of the left- and right-hand torques is done separately [3].

During static calibration, the chosen time intervals may have an impact on the calibration outcome. The torque transducer's creep is the main cause of this. By contrasting the observed values immediately following the conclusion of the preload with those following a later three-minute waiting time, it is possible to determine the impact of creep. It's also known as "short-term creep" [3].

Each transducer must be calibrated in a number of installation places in accordance with standards. The transducer is mounted and rotated around the measuring axis in

each of the various installation locations. It is best to use three separate orientations, each rotated by 120° . If geometrical reasons, such as a square mounting, limit the possibility of this orientation, then, four locations, each rotated by 90° , are also acceptable. Regarding two mounting positions, just accuracy classes 1, 2, and 5 are permitted for calibration with that, and an angle of 90° or 120° must be present between the positions.

Preloading and load series make up calibration at each installation point, as shown in Fig. 6.1.1. Three times, with the full-scale value to be calibrated, the preload is applied in the initial mounting position. Full scale value is preloaded just once in all other installation places. Prior to each load, the zero value must be logged. 30 seconds is advised as the preload holding period during static calibration [3].

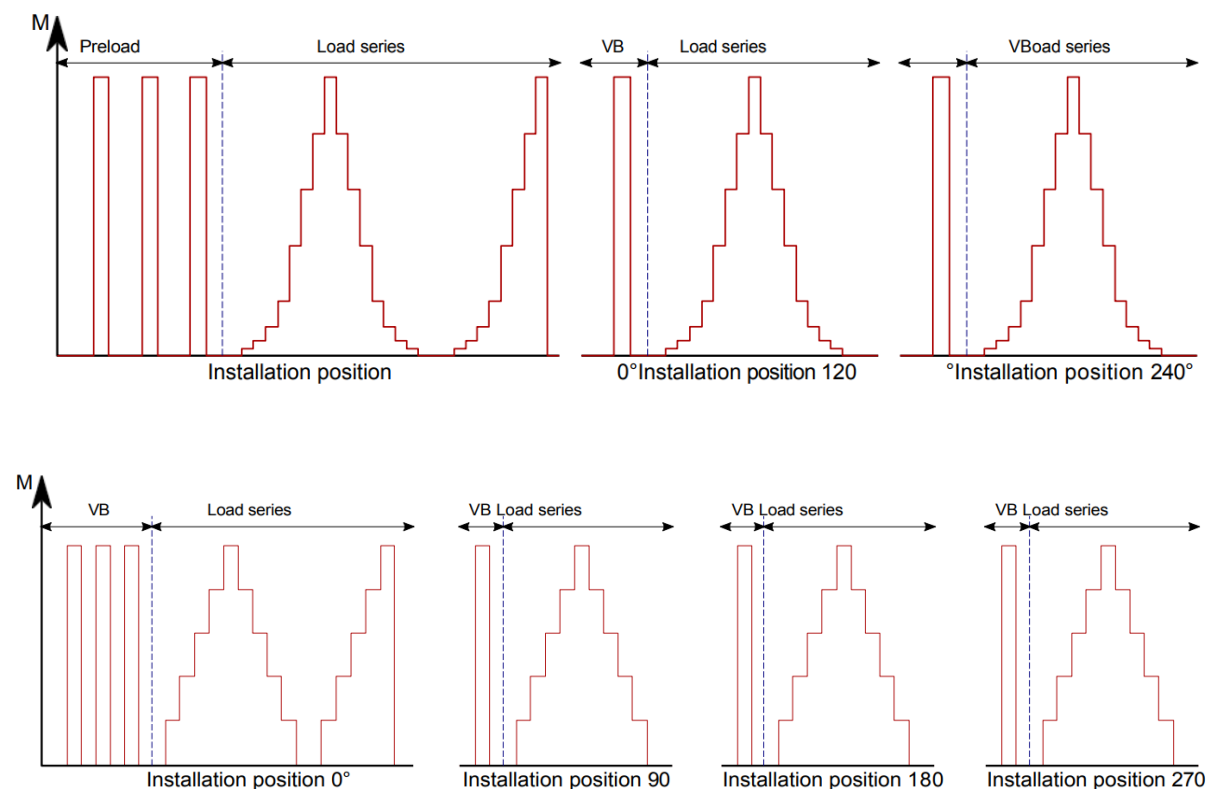


Figure 6.1.1: Calibration procedures for various installation positions, accordance to DIN 51309 [3]

Two increasing load series and one decreasing load series must be installed in the first installation position for accuracy classes 0.05 to 0.5. The second ascending series can be skipped for classes 1, 2, and 5. Only one upward and one downward series are needed in any other installation positions [3].

In addition to the zero-load step specified by DIN 51309 [3], a specific minimum number of torque steps per load series is necessary depending on the accuracy class that is intended. Table 6.1.1 can be used for this. A torque measurement device can also be calibrated separately for various torque ranges.

Class	Number of load steps	Load steps in % of M_E
0,05 0,1	8 (sensibly distributed over the measuring range)	e.g. 10 %, 20 %, 30 %, 40 %, 50 %, 60 %, 80 %, 100 % or 2 %, 5 %, 10 %, 20 %, 40 %, 60 %, 80 %, 100 %.
0,2 0,5	5	20 %, 40 %, 60 %, 80 %, 100 %
1 2 5	3	20 %, 60 %, 100 %

Table 6.1.1: Steps for torque calibration in accordance with DIN 51309 [3]

It is ideal to maintain a constant time gap between neighbouring stress levels. Additionally, during discrete calibration, the measured value may only be accepted once the display has stabilised. Exact adherence to the time sequence is crucial when display changes occur due to creep [3].

6.1.5 Steps for Evaluation

For each calibration torque and each installation position, a separate display value $I_j(M_k)$ is determined and then, it is corrected by the zero value. There are two ways to know for the determination. Before each series of measurements, the display value can either be set to zero or modified during the assessment process following the measurement. For this, the formula (6.1) is utilised.

$$X_j(M_k) = I_j(M_k) - I_{0,j} \quad (6.1)$$

where $X_j(M_k)$ is display value corrected by the zero value, I_j and I_0 are display in loaded condition and display in unloaded state before start of measurement series, respectively.

There are two instances that are distinguished while assessing the calibration.

Case I: It is defined “Case I” if there are just growing loads in the operation. In this instance, just the display values of the upward series by averaging over all installation places, are used to create the calibration result according to equation (6.2). Either a cubic or a linear function across the origin is calculated for interpolation in this situation. Under all conditions, the interpolation error $f_a(M_K)$ is used. However, neither the classification of the transducer nor the calculation of the relative standard measurement uncertainty account for the reversal span h [3].

$$\begin{aligned}
 Y(M_K) &= \frac{1}{n} \sum_{j=1}^n (I_j(M_K) - I_{0,j}) \\
 &= \frac{1}{n} \sum_{j=1}^n X_j(M_K)
 \end{aligned} \tag{6.2}$$

$Y(M_K)$ is defined as “Calibration result at calibration torque M_K without hysteresis (case I)”, while $I_j(M_K)$ and I_0 are “display value in loaded condition” and “display in unloaded condition before start of measuring series” relatively. Regarding n , it is “number of upward rows for different installation positions” and X_j is “display values corrected by the zero value of the increasing load series”.

Case II: It is defined as the case when it's unclear whether the load is increasing or decreasing. In this instance, both the display value of the upward series corrected by the zero value $X_j(M_K)$ and that of the downward series $X'_j(M_K)$ to be taken into consideration when calculating the calibration result $Y_h(M_K)$ according to the equation (6.3). In this instance, the origin is used to build a linear interpolation function. The display deviation $f_q(M_K)$ rather than the interpolation deviation $f_a(M_K)$ is decided in the case of fixed designated scale. Both the interpolation or display deviation and the reversal span h are taken into account in this classification. The determination of the relative uncertainty interval $W(M_K)$ follows the same rules [3].

In both situations, the calibration result $Y(M_K)$ or $Y_h(M_K)$ is calculated without using the second upward series of the 0° installation position. Separate compensation functions can also be calculated for moments that are increasing and decreasing. Such unique situations are no longer covered by the standard; hence the user is now in charge of the calculation [3].

$$\begin{aligned}
 Y_h(M_K) &= \frac{1}{n} \sum_{j=1}^n \left(\frac{I_j(M_K) + I'_j(M_K)}{2} - I_{0,j} \right) \\
 &= \frac{1}{n} \sum_{j=1}^n \left(\frac{X_j(M_K) + X'_j(M_K)}{2} \right)
 \end{aligned} \tag{6.3}$$

$I_j(M_K)$ is “display in loaded condition with increasing calibration torque M_K in mounting position j ” and $I'_j(M_K)$ is “display in loaded condition with decreasing calibration torque M_K in mounting position j ”. Meanwhile, $X_j(M_K)$ is “display value corrected by the zero value with increasing calibration torque M_K in installation position j ”, while $X'_j(M_K)$ is “display value corrected by the zero value with decreasing calibration torque M_K in installation position j ”.

Equation (6.4) is used to calculate the reproducibility $b(M_K)$ for each calibration torque M_K . It is the range of the upward series display values that has been calculated using various installation positions and then subtracted by zero value.

$$b(M_K) = X_{\max}(M_K) - X_{\min}(M_K) \tag{6.4}$$

X_{\max} and X_{\min} are “maximum and minimum of the display values measured in different positions reduced by the zero value at the calibration torque M_K ”

Equation (6.5), applied to each calibration torque M_K determines the repeatability $b'(M_K)$. It is the span of the upward series display values, calculated at the same mounting position and deducted by the upward series display values' zero value.

$$b'(M_K) = | X_1(M_K) - X_2(M_K) | \tag{6.5}$$

X_1 and X_2 are “the two values obtained in the identical mounting position, reduced by the calibration torque M_K `s zero value”

The second upward row of the 0° position (if existent) is not taken into consideration by either the reproducibility $b(M_K)$ or the repeatability $b'(M_K)$. Additionally, the repeatability precision for classes 1 through 5 is set to the reproducibility precision's value [3].

The zero point is noted before each upward series and after each descending series in order to calculate the zero-point deviation f_0 . About 30 seconds after the unloading process is complete, the zero-point reading should be taken. The second upward series of the 0° position is not used to calculate the zero-point deviation since the downward series is lacking. The largest sum of these value pairs from all installation positions is used to determine the zero-point deviation in equation (6.6).

$$f_0 = \max_j | I_{f,j} - I_{0,j} | \quad (6.6)$$

$I_{0,j}$ is “zero value before each upward series”, while $I_{f,j}$ is “zero value after each downward series”.

According to equation (6.7) the reversal span h , which is solely determined in case II, is the greatest amount of the disparities between the display values of the up and down series [3].

$$\begin{aligned} h(M_K) &= \max_j (| I_j(M_K) - I'_j(M_K) |) \\ &= \max_j (| X_j(M_K) - X'_j(M_K) |) \end{aligned} \quad (6.7)$$

A cubic or linear compensation function is used for the interpolation of torques between the discrete calibration torques M_K . A third-degree polynomial is utilised for case I and an accuracy class higher than 1. On the other hand, a first-degree function is employed for accuracy classes 1 and poorer as well as case II [3].

It is recommended to use the least squares method to calculate the compensating function. The user may also ask for the use of additional minimal requirements in justifiable exceptional circumstances. But this needs to be stated [3].

Equation (6.8) is used to compute the interpolation error, which is the difference between the calibration result, $Y(M_K)$ or $Y_h(M_K)$ and the appropriate compensation function value $Y_a(M_K)$ or $Y_{ah}(M_K)$ [3].

$$\begin{aligned} f_a(M_K) &= Y(M_K) - Y_a(M_K) && \text{(CASE I)} \\ f_a(M_K) &= Y_h(M_K) - Y_{ah}(M_K) && \text{(CASE II)} \end{aligned} \quad (6.8)$$

Only torque metres with displays in units of torque and no option to change the display to accommodate the interpolation, use the display deviation. It is the difference between the calibration torque M_K and the calibration result $Y(M_K)$, according to equation (6.9) [3].

$$f_q(M_K) = Y(M_K) - M_K \quad (6.9)$$

The difference between the measured value immediately after the third preload and 3 minutes after the third preload, divided by the maximum calibration result, is the short-time creep [3, 22].

$$KZK = \frac{I_{3\min} - I_{NVB}}{Y(M_E)} \quad (6.10)$$

6.1.6 Measurement Uncertainty Analysis and Error Estimation

Measurement accuracy is defined as the degree of agreement between the measured value and the true value of a measurand by the International Dictionary of Metrology. "Measurement accuracy" is not a quantity with a specific number attached to it. If a measurement has a lower measurement error, it is thought to be more accurate [4, 16].

The difference between a measurement result and a reference value is referred to as the (measurement) error, also known as measurement deviation. This reference value may be the genuine value of the quantity or a given value with known error that was achieved through calibration. Both the measured value and the uncorrected and corrected measurement results are referred to as measurement errors. The measurement uncertainty, according to the International Dictionary of Metrology [16], is an approximated number used to describe the range of values in which a measurand true value is situated [16].

For addressing measurement errors and uncertainty, numerous protocols and standards have been established in the meantime. Some are created especially for a particular application, while others of these are quite broad and hence suitable to all. Some pertinent practises and standards will be covered in more detail in the subsequent chapter.

6.1.7 Uncertainty of Measurement According to GUM

The "Guide to the expression of uncertainty in measurement" (GUM) [15] has become the accepted method for handling measurement uncertainty. According to SIEBERT and SOMMER [27, 29], any assertions about uncertainty made in standards like DIN or ISO must comply with the GUM. The phrase "measurement uncertainty" is defined as follows in the "Guide to the Expression of Uncertainty in Measurement" [6, 23]:

"Parameter assigned to the measurement result that characterizes the scatter of values that could reasonably be assigned to the measurand" [15].

This parameter includes the standard deviation or a specified multiple of it. It is also possible to provide a range as a half-width with a defined confidence level [15, 23].

Systematic and random measurement errors are not distinguished in the GUM [15]. A distinction is only made based on the method used to calculate the uncertainty. More information about this can be found under the procedure's next steps.

The benefit of using the conventional GUM technique is that nonstatistical information is treated systematically and can be processed step-by-step. Additionally, it is made feasible to create a measurement uncertainty budget and do an automated computation of the uncertainty. For instance, the GUM Workbench software can be used for this purpose [24, 29].

In this context, creating a measurement uncertainty budget is considered to mean representing all of the quantities utilised in a consistent tabular format. Additional attributes like the uncertainty contribution or the sensitivity coefficient can be displayed in addition to the value and name of the quantity.

The steps involved in figuring out the measurement uncertainty can be summed up as follows [6, 15, 23, 29]:

1. Presentation of the knowledge about the measurement and the input variables

The entire body of information regarding the measuring method and the relevant input variables serves as the procedure's foundation. This comprises all variables that affect the measurement outcome and the ensuing measurement uncertainty. This information can be gleaned from experience, earlier assessments, and the outcomes of precise measurements. The input amounts may also contain data from tables, test and calibration certifications, manufacturer specifications and data sheets, as well as information from the literature. It is useful to have variables with a quantitative evaluation because it is simpler to gauge their influence. The measuring task, including the causative variables and the variables to be measured, as well as the

measurement principle, measurement method, and application of the measurement procedure, must also be documented [6, 15, 23, 29].

2. Modelling the measurement

Finding a mathematical relationship $Y=f(X_1, X_2, \dots, X_N)$ from which to map the measurement is the goal of modelling. As a result, the quantity Y to be measured is linked with all pertinent input variables, X_i . This function f must also contain all correction factors that contribute significantly to the measurement uncertainty. Here, a cause-and-effect approach is particularly appropriate. In general, all measurement and calibration operations may be reduced to a straightforward cause-and-effect relationship. Rarely is this not feasible, but it does happen [6, 15, 23, 29].

3. Size Estimation

In this stage, an expected value x_i and accompanying standard deviation u_{xi} are assigned to each input variable X_i . Probability density functions are employed in both of the two methods of determination (A and B) for the quantitative description of the variables.

Here is a more thorough explanation of these two techniques:

- Type A: To calculate the measurement uncertainty, statistical techniques are applied. As an illustration, consider the analysis of a set of observations.
- Type B: A list of all the quantities for which the uncertainties have been calculated using non-statistical methods. Examples include calibration certifications, calibration reports, and manufacturer data on the measurement technology's error limits [6, 15, 23, 29].

4. Combination of the values and uncertainties

In this step of the procedure, the measurement result that is, the estimated value y for the measured variable Y is established with the use of the function f . According to equation (6.11) the expected value x_i is utilised in place of the input variable X_i .

$$y = f(x_1, x_2, \dots, x_N) \quad (6.11)$$

Furthermore, the combined standard deviation u_y of the measurement result y is calculated in accordance with the formula (6.12).

$$\begin{aligned}
 u_y &= \sqrt{\sum_{i=1}^N \left(\left(\frac{\partial^2 f}{\partial x_i} \right)^2 u_{xi}^2 \right) + 2 \sum_{i=1}^{N-1} \sum_{j=i+1}^N \left(\frac{\partial^2 f}{\partial x_i} \frac{\partial^2 f}{\partial x_j} u_{xixj} \right)} \\
 &= \sqrt{\sum_{i=1}^N (c_i^2 u_{xi}^2) + 2 \sum_{i=1}^{N-1} \sum_{j=i+1}^N (c_i c_j u_{xixj})} \\
 &\quad u_{xixj} = u_{xi} \cdot u_{xj} \cdot r(x_i, x_j)
 \end{aligned} \tag{6.12}$$

y = Estimated value for the measurand

u_y = Combined Standard deviation of the measurement result y

u_{xixj} = estimated covariance of the variables x_i and x_j

r = Correlation coefficient

x_i = Expected values of the input variables

u_{xi} & u_{xj} = Standard deviations of the input variables

c_i & c_j = Sensitivity coefficients

The correlation can be disregarded when the input variables are not correlated or are only weakly correlated, or when the correlation has little impact on the total level of uncertainty. Only the linear portion of the Taylor series expansion is used in the calculation of the combined standard deviation, or u_y , which is based on the conventional Gaussian error propagation. For this standard, the GUM technique can only be used to calculate models whose linear approximation at the operational point deviates from the model under investigation by a sufficiently modest amount [6, 15, 23, 29].

5. Calculation of the expanded measurement uncertainty

The extended measurement uncertainty is expressed as the interval's half-width. In Fig. 6.1.2, this is depicted graphically.

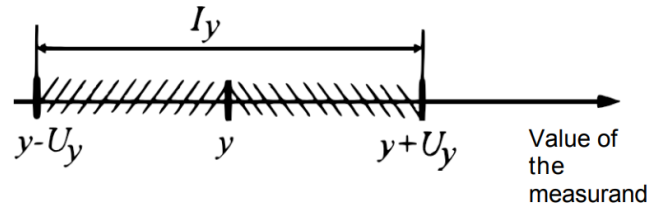


Figure 6.1.2: Expanded measurement uncertainty as value interval

Here, y can be defined as “estimated value for the measurand”, while I_y and U_y are “interval from y ” and “extended measurement uncertainty”, respectively.

This covers a significant portion of all values for which a meaningful assignment to the measurement result is conceivable, with a probability P of more than 95%. According to equation (6.13), the measurement uncertainty U_y is computed by multiplying the combined standard deviation u_y by the coverage factor k_p [6, 15, 23, 29].

$$U_y = k_p \cdot u_y \quad (6.13)$$

The coverage factor k_p often has values between 2 and 3 [6, 15, 23, 29].

6. Indication of the complete measurement result

According to GUM, this is always carried out using the formula in equation (6.14), which is the expected value y plus/ minus Uncertainty U_y [6, 15, 23, 29].

$$Y = y \pm U_y \quad (6.14)$$

7. Establishing and evaluating the measurement uncertainty budget

The creation of a budget for measurement uncertainty is the process's last stage. It offers all the data required to streamline the measurement procedure. The following information needs to be listed in columns:

- Name of the quantity x_i
- The distribution on which the listed quantity is based
- The possible range of values of the variable
- The expected values x_i along with the size-related standard uncertainty u_{x_i}
- The sensitivity coefficients c_i

- The uncertainty contributions $u_{iy} = c_i \cdot u_{xi}$, in order to be able to assess the contributions to the total uncertainty

Process steps 4 to 7 are based on clearly defined mathematical algorithms. As a result, they can be used on a computer with software support. The GUM-Workbench software, for instance, can be used for this [6, 15, 23, 29].

6.1.8 Uncertainty of Calibration According to DIN-51309

The method for determining the measurement uncertainty in the calibration of torque measuring instruments proposed in DIN 51309 [3] is primarily based on that for the calibration of force measuring devices. However, it is reasonable to diverge from this process if it is technically justifiable. This method does not apply to torque measuring tools like torque wrenches, which introduce torque through a one-sided lever and a force operating on it. In these scenarios, additional variables, like the shear force or bending moment, must be taken into account in the uncertainty analysis [3].

The consideration of additional uncertainty components might be taken into account depending on the application of the torque measuring instrument that needs to be calibrated. In these situations, the computation foundation must be recorded. Only the calibration result is outside of this calculation's range of validity. The user must individually consider effects like speed influence, interference brought on by a change in adaptation, long-term stability influence, temperature influence, as in engine test stands, or dynamics influence. It is therefore feasible that the overall uncertainty in real-world applications is much greater than the uncertainty determined here [3].

The calibration torque and other influencing factors have an impact on the calibration result Y in a functional way. The influencing factors in turn result in a modification of the display X_i . Equation (6.15) describes this relationship.

$$Y(M_\kappa) = C \cdot M_\kappa \cdot \prod_{i=1}^n (1 - \delta X_i) \quad (6.15)$$

$Y(M_\kappa)$ = Calibration result at calibration torque M_κ

M_κ = Calibration torque

C = Factor for taking into account a unit of the display deviating from the torque unit

δX_i = Influencing variable on the Display X_i

Important influencing variables are also listed in Table 6.1.2 [3].

δX_1	Influence of the resolution r of the display unit on the zero value
--------------	---

δX_2	Influence of the resolution r of the display unit on the display value
δX_3	Influence of the reproducibility b
δX_4	Influence of repeatability b'
δX_5	Influence of the zero-point deviation f_0
δX_6	Influence of the display deviation f_q or the interpolation deviation f_a
δX_7	Influence of the reversal span h

Table 6.1.2: Important variables influencing the display according to DIN 51309 [3]

The relative standard measurement uncertainty can be calculated by the formulas below. The formulas are different for Case I and Case II:

$$\begin{aligned}
 & \text{CASE I} \\
 w(M_K) &= \sqrt{w_{KE}^2(M_K) + \sum_{i=1}^6 w^2(\delta X_i)} \\
 &= \sqrt{w_{KE}^2(M_K) + 2 \cdot w_r^2(M_K) + w_b^2(M_K) + w_{b'}^2(M_K) + w_0^2(M_K) + w_{fa}^2(M_K)} \quad (6.16) \\
 & \text{CASE II} \\
 w(M_K) &= \sqrt{w_{KE}^2(M_K) + \sum_{i=1}^5 w^2(\delta X_i)} \\
 &= \sqrt{w_{KE}^2(M_K) + 2 \cdot w_r^2(M_K) + w_b^2(M_K) + w_{b'}^2(M_K) + w_0^2(M_K)}
 \end{aligned}$$

$w(M_K)$ = Standard measurement uncertainty

w_r = Relative standard deviation determined by the influence of the resolution r

$w_{b'}$ = Relative standard deviation determined by the influence of repeatability b'

w_b = Relative standard deviation determined by the influence of the reproducibility b

w_{fa} = Relative standard deviation determined by the influence of the interpolation deviation f_a

w_0 = Relative standard deviation determined by the influence of the zero-point deviation f_0

The formulae listed in Table 6.1.3 can be used to compute the relative standard deviation of the individual contributions.

Characteristic value	Relative standard deviation w in %	Distributio n
Resolution r	$w_r = \frac{100 \cdot r}{2 \cdot \sqrt{3} \cdot M_K}$	Type B rectangular distribution
Comparison precision b	$w_b = \frac{100 \cdot b(M_K)}{2 \cdot \sqrt{3} \cdot Y(M_K)}$	Type B rectangular distribution
Repeatability b'	$w_{b'} = \frac{100 \cdot b'(M_K)}{2 \cdot \sqrt{3} \cdot Y(M_K)}$	Type B rectangular distribution
Zero point deviation f_0	$w_{f_0} = \frac{100 \cdot f_0}{2 \cdot \sqrt{3} \cdot Y(M_E)}$	Type B rectangular distribution
Interpolation deviation f_a	$w_{f_a} = \frac{100 \cdot f_a(M_K)}{2 \cdot \sqrt{6} \cdot Y(M_K)}$	Type B triangular distribution

Table 6.1.3: Relative standard deviations of the characteristic values determined from experimentally determined data according to DIN-51309 [3].

Since the calibration result is produced from the difference between the display value and the zero value and the resolution influences the uncertainty of both values, the uncertainty w_r is incorporated twice in the computation [3]. According to equation (6.17), the coverage factor and the relative standard measurement uncertainty in case I lead to the relative extended uncertainty $W(M_K)$ [3].

$$W(M_K) = k \cdot w(M_K) \quad \text{for } k = 2$$

$$W(M_K) = 2 \cdot \sqrt{w_K^2(M_K) + 2 \cdot w_r^2(M_K) + w_b^2(M_K) + w_{b'}^2(M_K) + w_0^2(M_K) + w_{f_a}^2(M_K)} \quad (6.17)$$

In the calibration test of FZG Hypoid test rig, Case I will be used in order to calculate the relative extended uncertainty.

6.2 Calibration of the Torque Measuring System on the FZG Hypoid Test Rig

6.2.1 Introduction of Lever-Mass System

The lever-mass system was used to calibrate the torque measurement system on the hypoid efficiency test rig in line with DIN 51309 [3]. Fig. 6.2.1 depicts this schematically.

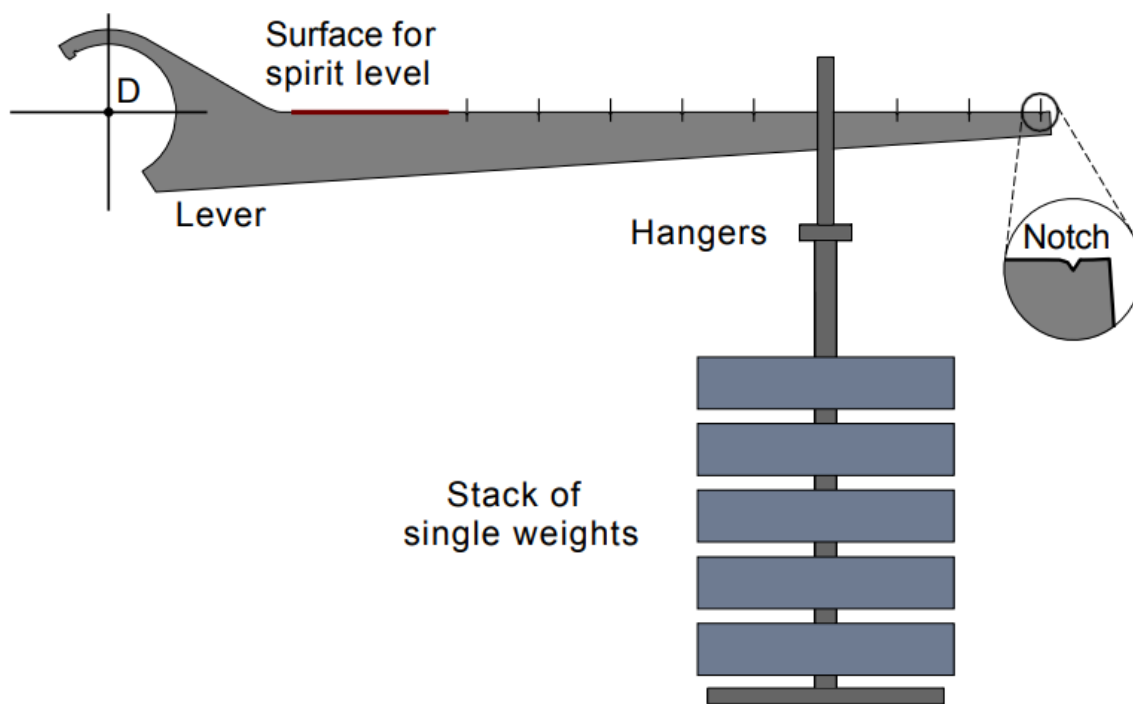


Figure 6.2.1: Schematic view of lever-mass system used to calibrate the torque measurement system

According to the main principle of the lever-mass system type of calibration, each single weight at a particular mass value, is adjacently added to the system in order to load the test rig at several discrete torque values. By adding and removing them at a certain way, test rig is loaded and unloaded, and display values in terms of Nm or Voltage are noted for data processing.

6.2.2 Preparation of Calibration and Calibration Setup

Since the hypoid efficiency test bench is located in an air-conditioned room with opened doors, the temperature is considered unchanged during calibration. The measurement and recording of the temperature at the starting and end of each measurement series, as required by DIN 51309, is waived.

The calibration setup consists of fuser unit, calibration lever, hanger, spirit level, and 9 additional weights with different mass values. The illustration of each component with corresponding function is explained in the following paragraphs.

Initially, the double-lever which is generally used to load the cycle at the desired torque, is attached on coupling and the torque in the cycle is completely unloaded to zero. Subsequently, all screws joining coupling flanges, are loosened and remained the same during the entire calibration test.

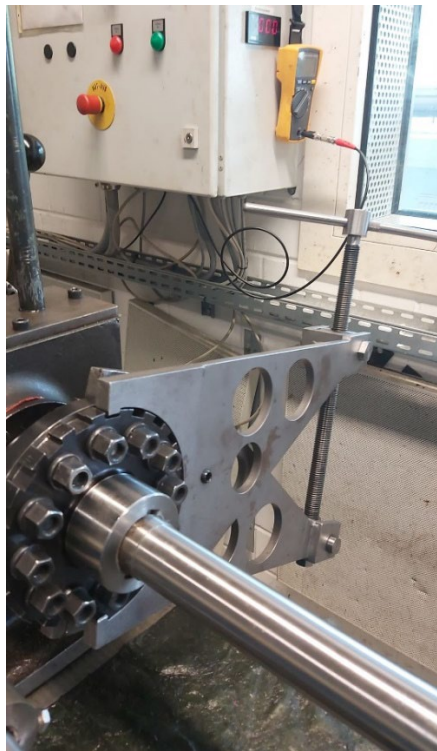


Figure 6.2.2: Attachment of double-lever for unloading the test rig

Followingly, the Fuser Unit, shown in Fig 6.2.3, is attached to coupling flange in order to block the rotation. Its other side is pinned to the base of test rig which is accepted highly rigid to prevent any rotation.



Figure 6.2.3: Fuser Unit

In the next step, the sensor which is mounted in the rear end of pinion shaft in order to measure cycle, was disassembled and calibration lever is attached to that end of pinion shaft. The calibration shaft is used in order to apply various loadings to the system. By considering the notch at the end of calibration lever, from where the hanger is mounted, the moment arm is measured as 0.5 m. The hanger which weights 1.725 kg, is considered as the first added mass and relevant measurement notes are aimed to be taken before and after installation of calibration lever itself. Noting that, the 1.725 kg is not the weight of the calibration lever from its centre of gravity. Instead, it is the transferred weight of its notch point. As all additional weights apply loading by their gravity force from the notch, it is crucial to determine the loading of weight of calibration lever from the same point.



Figure 6.2.4: Calibration Lever

Following this lever, the hanger is mounted from the notch and its function is to carry all additional weights during the test. The lower part of hanger is designed flat and circular in order to easier installation of extra weights, whereas sharp triangular part

is designed in its upper part for proper installation to notch section of calibration lever. Similar to the calibration lever, the hanger, with 4.4 kg, can also be seen as an added extra weight to the system. In this case, it is essential to carry out appropriate measurements before and after the assembly of the hanger itself.



Figure 6.2.5: Hanger

Following the calibration lever and hanger, totally 9 extra weights are used in order to discreetly load the test rig at various torque values. They are installed consecutively in the increasing order during loading, and all at the same time for initial pre-loading. The weights of all calibration weights will be revealed in the following paragraphs.



Figure 6.2.6 :Calibration Weights

The detailed vision of the whole calibration setup is shown in Fig 6.2.7. It has to be mentioned that, for all loading cases with different weights, the calibration lever has

to be maintained perfectly horizontal in order to precisely consider moment arm as 0.5 m. Therefore, for checking its horizontality, the spirit level is used by locating it onto the calibration lever. If needed, horizontality is adjusted by screw motion of the vertical part of fuser unit.



Figure 6.2.7: The Calibration Setup Installed on the FZG Hypoid Test Rig

6.2.3 Carrying out the Calibration

According to DIN 51309 [3] standards, it is crucial that torque measuring system is calibrated in a several installation places.

Each transducer must be calibrated in a number of installation places in accordance with DIN 51309 standards [3]. It is suggested to carry out the test at three different orientations, by rotating the shaft at 120° . Apart from this, testing at four locations by 90° degrees rotation, is also feasible; in case there are some geometric constraints. On the other hand, at FZG hypoid test rig, due to number and geometric dimension on teeth of coupling flange and teeth of fuser unit, there is not any possibility to attach them after rotating 90° or 120° of rotation. Therefore, after carrying out the test at any particular shaft position, it is then rotated 180° and repeated again corresponding to

the relevant test guidelines. Subsequently, also for the third and fourth times, the shaft is rotated 180°.

The weight of all calibration weights, included those of calibration lever and hanger, can be seen in Table 6.2.1. The discrete torque values are selected in such a way that they correspond approximately to the load steps from 0-100 % of the maximum torque.

Calibration Weight Number	Value
Calibration Lever	1.725 kg
Hanger	4.4 kg
m_4	5.2 kg
m_5	6.8 kg
m_6	8.4 kg
m_7	9.8 kg
m_8	11.4 kg
m_9	12.8 kg
m_10	14.4 kg
m_11	15.8 kg
m_12	17.2 kg

Table 6.2.1: Mass values of Calibration weights

To summarize, the shaft must be calibrated at 4 different offset 180° positions when performing the calibration test. The first of the four positions must be calibrated using the basic load spectrum, and all other positions must be calibrated using the reduced load spectrum. According to Figure 6.2.8, the base load spectrum is composed of:

1. A threefold preload using the highest test load,
2. a 3-minute phase of relaxation to assess short-term creep,

3. a staircase with a rising and a lowering load;
4. A second phase of rising loads, then fully unloading.

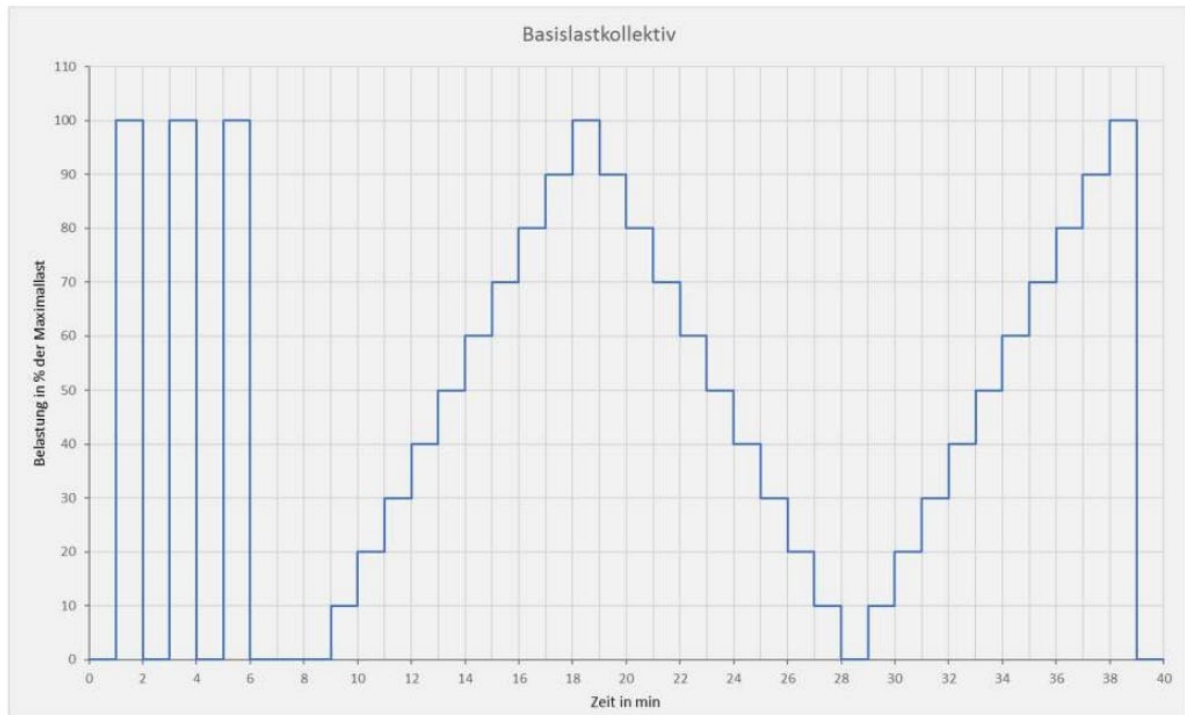


Figure 6.2.8: Basic Load Spectrum

On the other hand, the reduced load spectrum seen in Fig. 6.2.9 has just one preload stage, as opposed to the basic load spectrum's many preload steps. The second step of increasing load is also absent. This saves roughly 15 minutes in terms of time.

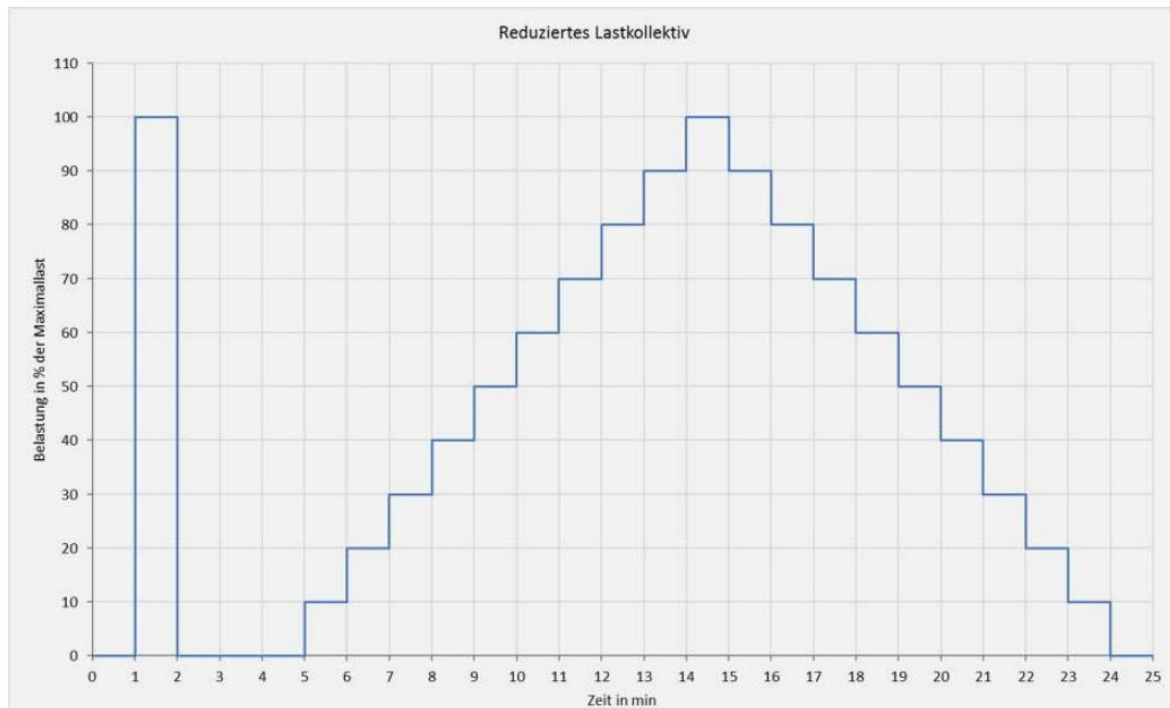


Figure 6.2.9: Reduced Load Spectrum

6.2.4 Data Collection

For data collection, the multimeter was used to measure results in terms of voltage. For all loading cases, it was waited for a minute or even longer in order to properly achieve fully stabilization of measuring device. Noting that, measurement was carried out accurately to three decimal places.

After carrying out all initial preparation steps and proper installation of all calibration test components, the calibration test was performed for position 1 by using basic load spectrum steps. All the measured and noted values are shown in Appendix A.

Subsequently, the shaft is rotated 180° Counter-clockwise direction to reach “Position 2” and fuser unit was attached to flange of coupling in the relevant way again. The same testing procedure was repeated, and results were noted as given in Appendix A. Followingly, for last two positions, exactly the same steps were repeated and relevant measurements were taken which can also be found in the same Appendix.

6.3 Calibration Test Results & Sensitivity Analysis

Following the complete data collection for different calibration torques and shaft positions, the measured values were processed in accordance with DIN 51309 [3] standards. Initially, upward, and downward series of display values at all 4 shaft positions were extracted by correcting with zero value, and then averaged. All measured loading values, as well as averaged one are presented below:

Position 1	Position 2	Position 3	Position 4	Average
0	0	0	0	0
0.071	0.054	0.064	0.063	0.063
0.242	0.224	0.24	0.233	0.23475
0.443	0.425	0.433	0.432	0.43325
0.703	0.687	0.698	0.696	0.696
1.027	1.007	1.018	1.02	1.018
1.407	1.384	1.399	1.398	1.397
1.842	1.827	1.834	1.834	1.8342
2.35	2.321	2.331	2.331	2.3333
2.887	2.867	2.877	2.885	2.879
3.497	3.43	3.481	3.495	3.4757
4.161	3.952	4.192	4.159	4.116
3.502	3.473	3.489	3.486	3.4875
2.895	2.881	2.881	2.878	2.8838
2.337	2.319	2.329	2.327	2.328
1.843	1.828	1.838	1.834	1.8357
1.406	1.391	1.4	1.411	1.402
1.028	1.01	1.02	1.019	1.0192
0.705	0.708	0.705	0.707	0.70625
0.449	0.439	0.435	0.439	0.4405
0.246	0.234	0.235	0.239	0.2385
0.078	0.054	0.068	0.067	0.06675
0.011	-0.015	-0.004	0	-0.002

Table 6.3.1: Measured and averaged display values

After achieving a single upward and downward series of measured values, both were averaged again with themselves in order to obtain a unique display values, in terms of voltage (V) for each discrete torque value. Meanwhile, as figures of all additional weights and length of calibration lever was known, the discrete calibration torques was calculated as well:

$$M_K = m_{total} g L \quad (6.18)$$

Where m_{total} is total weight of all installed weight components in all discrete steps, while g and L are gravitational acceleration and length of calibration lever, respectively.

Subsequently, a linear interpolation operation was carried out in order to obtain a linear curve fitting between display values (V), and calibration torques (Nm). These final quantities and curve fitting plotting are shown below:

Display Value (V)	Calibration Torque (Nm)
0	0
0.064875	8.4611
0.23662	30.043
0.43688	55.549
0.70112	88.903
1.0186	130.11
1.3995	178.17
1.835	234.09
2.3306	296.88
2.8814	367.51
3.4816	445.01
4.116	529.37

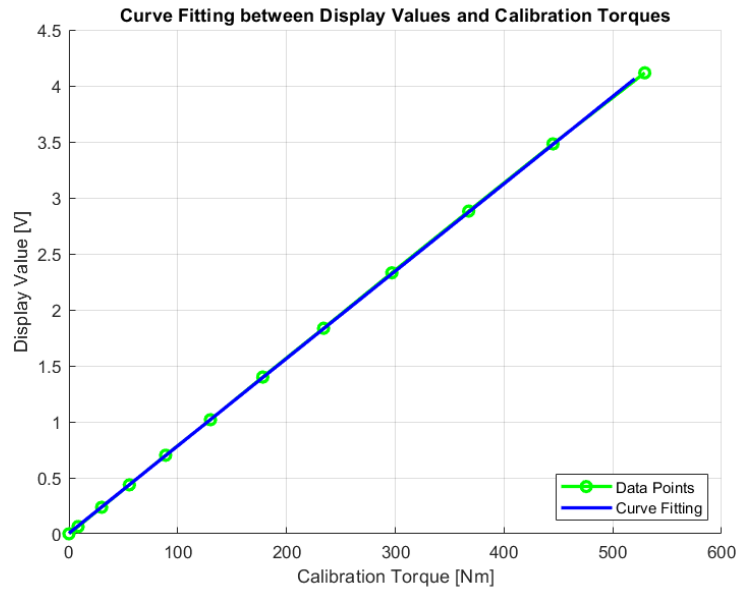


Table 6.3.2: Display values and Calibration Torque values

Figure 6.3.1: Curve Fitting between Display Values and Calibration Torque

Meanwhile, during the entire test procedure, it was noticed that only last (third) active digit is fluctuating. According to the relevant standard, in this case, resolution can be defined as “0.001” which corresponds to third decimal place.

Considering these data points and relevant equations, reproducibility (6.4), zero-point deviation (6.6), interpolation deviation (6.8) can be calculated. All these intermediate quantities are presented below:

r	b	f_a	f_0
0.001	0	0	0.015
0.001	0.017	-0.0059524	0.015
0.001	0.018	-0.002534	0.015
0.001	0.018	-0.0013304	0.015
0.001	0.016	0.0026935	0.015
0.001	0.02	-0.0012622	0.015

0.001	0.023	0.0045311	0.015
0.001	0.015	0.0038197	0.015
0.001	0.029	0.0096074	0.015
0.001	0.02	0.0092905	0.015
0.001	0.067	0.0043975	0.015
0.001	0.24	-0.018946	0.015

Table 6.3.3: Reproducibility, Zero-point deviation, Interpolation deviation,
Resolution

Although discrete calibration torques were calculated before, their standard deviations should also be considered due to deviation on values of additional weights and length of calibration lever. Assuming these deviations as in Table 6.3.4, and using GUM Workbench, relative standard deviations of the calibration torque values, were directly received.

Furthermore, the type of distribution for all torque values depending on standard deviation, and corresponding %95 confidence level k factor were also achieved. All distribution diagrams were presented in detail in Appendix C. Finally, relative standard deviation determined by the influence of calibration torque, w_{KE} can be simply calculated by dividing the relative standard deviations of the calibration torque values to the corresponding k factor for %95 confidence level, as illustrated in Table 6.3.5.

Physical Quantity	Average Value	Standard Deviation
m_lever	1725 kg	0.05 kg
m_hanger	4.4 kg	0.05 kg
m 4	5.2 kg	0.05 kg
m 5	6.8 kg	0.05 kg
m 6	8.4 kg	0.05kg
m 7	9.8 kg	0.05 kg
m 8	11.4 kg	0.05 kg
m 9	12.8 kg	0.05 kg
m 10	14.4 kg	0.05 kg
m 11	15.8 kg	0.05 kg
m 12	17.2 kg	0.05 kg
L	0.5 m	0.005 m
g	9.807595 m/s ²	698e-06 m/s ²

Table 6.3.4: Standard deviations of physical quantities used to calculate calibration
torques

Torque	Value	Relative Standard Deviation	k factor	Type of Distribution	w_{KE} (%)
M_0	0 Nm	0	2.00	95% (Normal)	0
M_1	8.46 Nm	3.1 %	1.77	%95 (Trapezoidal, Form factor = 0.5)	1.7514
M_2	30.04 Nm	1.6 %	2.00	95% (Normal)	0.8
M_3	55.54 Nm	1.3 %	2.00	95% (Normal)	0.65
M_4	88.90 Nm	1.1 %	1.85	%95 (Trapezoidal, Form factor = 0.3)	0.5946
M_5	130.1 Nm	1.1 %	1.77	%95 (Trapezoidal, Form factor = 0.5)	0.6215
M_6	178.1 Nm	1.0 %	1.77	%95 (Trapezoidal, Form factor = 0.5)	0.565
M_7	234.0 Nm	1.0 %	1.77	%95 (Trapezoidal, Form factor = 0.5)	0.565
M_8	296.8 Nm	0.98 %	1.69	%95 (Trapezoidal, Form factor = 0.7)	0.5799
M_9	367.4 Nm	0.97 %	1.69	%95 (Trapezoidal, Form factor = 0.7)	0.574
M_{10}	444.9 Nm	0.97 %	1.69	%95 (Trapezoidal, Form factor = 0.7)	0.574
M_{11}	529.2 Nm	0.97 %	1.69	%95 (Trapezoidal, Form factor = 0.7)	0.574

Table 6.3.5: Calibration torque values with relative standard deviations

Using all formulas at Table 6.1.3; all relative standard deviations determined by the several influences, can be easily calculated. Finally, collecting all those relative standard deviations in equation 6.17, the relative extended uncertainty $W(M_k)$ can be finally obtained. All these quantities are introduced below:

$(w_{KE})\%$	$(w_r)\%$	$(w_b)\%$	$(w_{f0})\%$	$(w_{fa})\%$	$W(M_k)$
0	0	0	0	0	0
0.017514	0.44497	0.075645	0.1052	1.8729	0.16025
0.008	0.122	0.021959	0.1052	0.22291	0.047128
0.0065	0.066077	0.011894	0.1052	0.062163	0.027282
0.0059459	0.041173	0.0065877	0.1052	0.078418	0.017979
0.0062147	0.02834	0.0056679	0.1052	0.025294	0.01698
0.0056497	0.020627	0.0047442	0.1052	0.066817	0.014975
0.0056497	0.015732	0.0023597	0.1052	0.04249	0.012462
0.0057988	0.012386	0.003592	0.1052	0.084145	0.01391
0.0057396	0.010019	0.0020037	0.1052	0.065816	0.012413
0.0057396	0.0082914	0.0055552	0.1052	0.028714	0.016125
0.0057396	0.0070135	0.016832	0.1052	0.09396	0.03569

Table 6.3.6: Relative Standard Deviations and Relative Extended Uncertainty

Finally, by using average display values and the relative extended uncertainty, the absolute extended uncertainty can be calculated. Considering all these findings together as it is shown in Table 6.3.7, it can be concluded that there is generally a significantly small relative extended uncertainty figures at almost all calibration torques. Only for M_2 , there is a substantially higher uncertainty compared to others. It can be explained by a considerably larger interpolation deviation for low torque values. In other words, when considering Fig. 6.3.1, at very little torques, data points and curve fitting for linear interpolation significantly differs. If third degree polynomial function is preferred rather than linear one, it could lead to smaller uncertainties for low torque values.

Display [V]	W_{abs} [V]	M_K [Nm]	$\pm\Delta M_K$ [Nm]	$W(M_K)$
0	0	0	0	0
0.064875	± 0.010397	8.46	1.36	0.16025
0.23662	± 0.011152	30.04	1.42	0.047128
0.43688	± 0.011919	55.54	1.52	0.027282
0.70112	± 0.012606	88.90	1.60	0.017979
1.0186	± 0.017296	130.10	2.21	0.01698
1.3995	± 0.020958	178.10	2.67	0.014975
1.835	± 0.022868	234.00	2.92	0.012462
2.3306	± 0.03242	296.80	4.13	0.01391
2.8814	± 0.035765	367.40	4.56	0.012413
3.4816	± 0.056143	444.90	7.17	0.016125
4.116	± 0.14686	529.20	18.89	0.03568

Table 6.3.7: Relative extended uncertainty and Absolute extended uncertainties

Considering average values of discrete calibration torques with corresponding deviations in terms of Nm, it can be commented that there are significantly less deviation values in comparison with average values. For almost all torque levels, the torque fluctuation remains below 10 Nm, except for the highest torque level. It was mentioned in 5.3.2 that ± 10 Nm torque dispersion results in only 13 MPa, which is negligible part of the maximum flank pressure for all preloading cases. Therefore, the influence of these small load fluctuations on experimental test results can be clearly neglected.

As a result, it can be ended up that torque measurement system is sufficiently precise, due to reasonably small deviation quantities. Therefore, applied torque on test cycle by appropriate tools, is measured and displayed in an accurate level.

7. Conclusion

Eventually, this thesis describes the definition and evaluation of feasible sources of dispersion of the experimental test results at the Back-to-Back Hypoid Test Rig at the Gear Research Center (FZG) at the Chair of Machine Elements of the Technical University of Munich. It was analyzed to identify why pitting failure occurs at any shifted position on the flank surface of pinion and wheel after numerous load cycles, although the contact pattern is initially arranged in the center of flank surface.

To begin with, with considering related literature works, experimental investigations were carried out for analyzing the influence of the micropitting on the scatter of test results. According to results of tests carried out at the test rig, it can be clearly identified that the existence of micropitting can significantly lead to shifting of contact pattern. In other words, the existence of micropitting is substantially associated with not proper accumulation of contact pattern on gear flanks.

Afterwards, other possible variables that might also influence on the deviation of experimental results were analyzed, such as input torque, its minor fluctuations, preloading on pinion shaft bearings and accuracy of torque measurement system. According to the findings from appropriate analysis methods, it was determined that none of these variables has a significant effect on the deviation of contact pattern. As a result, the micropitting was identified as the dominant influencing factor on the scatter of the experimental results.

Further Comments

Considering all the findings of this thesis, the main suggestion for elimination of scatter of experimental results, can be increase of oil viscosity, which can lead to increase of safety against micropitting. However, while checking the completed research activities at the Gear Research Center FZG, it becomes evident that this method has already been applied and has not fully prevented the occurrence of micropitting. Micropitting and its effects on the dispersion of experimental results should be highly considered for this Back-to-Back Hypoid Test Rig with a very high axial offset (31.75 mm).

Bibliography

- [1] Bevel gear strength rating: The appropriate combination of FEM with rating standards. Gear Solutions Magazine Your Resource to the Gear Industry. (2022, December 15). <https://gearsolutions.com/features/bevel-gear-strength-rating-the-appropriate-combination-of-fem-with-rating-standards/>

- [2] Boiadjiev, I. (2019). Schadensentwicklung und tragfähigkeit carbonitrierter Kegelradverzahnungen Untersuchung der tragfähigkeit von carbonitrierten kegelrad- und Hypoidverzahnungen (thesis).

- [3] DIN 51309. (2005). Werkstoffprüfmaschinen - Kalibrierung von Drehmomentmessgeräten für statische Drehmomente.

- [4] DIN Deutsches Institut für Normung. (1984). Internationales Wörterbuch der Metrologie - International vocabulary of basic and general terms in metrology, Berlin.

- [5] DIN EN ISO 376. (2011). Metallische Werkstoffe - Kalibrierung der Kraftmessgeräte für die Prüfung von Prüfmaschinen mit einachsiger Beanspruchung.

- [6] DIN V ENV 13005. (1999). Leitfaden zur Angabe der Unsicherheit beim Messen.

- [7] Drechsel, A., Constien, L., Pellkofer, J., Boiadjiev, I., & Stahl, K. (2022). Extended calculation method for determining the pitting load carrying capacity of bevel and hypoid gears. *Forschung Im Ingenieurwesen*, 86(4), 829–844. <https://doi.org/10.1007/s10010-022-00596->

- [8] FZG Website. Startseite. (2023). <https://www.mec.ed.tum.de/fzg/startseite/>
- [9] Gear Solutions Magazine. Gear Solutions Magazine Your Resource to the Gear Industry. (2017, January 9). <https://gearsolutions.com/news/klingelnberg-adopts-industry-4-0-through-compatibility-among-systems/>
- [10] Höhn, B. R., Stahl, K., & Wirth, C. (2011). New calculation method for the load capacity of bevel and hypoid gears based on loaded tooth contact analysis. *Applied Mechanics and Materials*, 86, 237–242. <https://doi.org/10.4028/www.scientific.net/amm.86.237>
- [11] Hösel, T., & Goebbelet, J. (1979). Empfehlung zur Vereinheitlichung von Flankentragfähigkeitsversuchen an vergüteten und gehärteten Zylinderrädern. FVA-Merkblatt Nr. 0/5.
- [12] ISO 10300-2:2014. (2014). Calculation of Load Capacity of Bevel Gears — Part 2: Calculation of Surface Durability (Pitting). International Organization for Standardization.
- [13] ISO 23509:2016. (2016). Bevel and Hypoid Gear Geometry. International Organization for Standardization.
- [14] ISO 6336-2:2019.(2019). Calculation of Load Capacity of Spur and Helical Gears — Part 2: Calculation of Surface Durability (Pitting). International Organization for Standardization.
- [15] JCGM 100.2008. (2008). Guide to the expression of uncertainty in measurement - JCGM 100:2008 (GUM 1995 with minor corrections - Evaluation of measurement data. URL: https://www.bipm.org/utils/common/documents/jcgm/JCGM_100_2008_E.pdf
- .

- [16] JCGM Joint Committee for Guides in Metrology. (2012). JCGM 200:2012 International vocabulary of metrology - Basic and general concepts and associated terms (VIPM).
- [17] Kawalec, A., Wiktor, J., & Ceglarek, D. (2005). Comparative analysis of tooth-root strength using ISO and AGMA standards in spur and helical gears with FEM-based verification. *Journal of Mechanical Design*, 128(5), 1141–1158. <https://doi.org/10.1115/1.2214735>
- [18] Kegellradverzahnungen. TU Dresden. (2023, April 20). <https://tu-dresden.de/ing/maschinenwesen/imm/me/forschung/kegellradverzahnungen>
- [19] KIMOS SOFTWARE - INDUSTRY 4.0 IN PRACTICE: DESIGN OF BEVEL GEAR GEOMETRY AND THE MANUFACTURING PROCESS. Klingelberg group: Geometry, process, and tool design for Bevel Gears. (n.d.). <https://klingelberg.com/en/business-divisions/bevel-gear-technology/software/kimos>
- [20] Kimos Bevel Gear Design. Coroflot. (n.d.). <https://www.coroflot.com/lucaghiotto/KIMoS-Bevel-Gear-Design>
- [21] Klingelberg, J. (2016). *Bevel Gear Fundamentals and Applications*. Springer.
- [22] Landler, S.; Leonhardt, C. (2019). Messunsicherheit nach GUM eines Prüfstands zur Ermittlung des Drehmoments und des Drehwinkels, Lehrstuhl für Maschinenelemente - Forschungsstelle für Zahnräder und Getriebebau (FZG) - Technische Universität München.
- [23] Leitfaden zur Angabe der Unsicherheit beim Messen. (1995).

- [24] Metrodata GmbH. (2010). GUM Workbench - Benutzerhandbuch für Version 1.3, 2.3 und 2.4, Metrodata GmbH, Weil am Rhein.
- [25] Pellkofer, J., Boiadjiev, I., Kadach, D., Klein, M., & Stahl, K. (2019). New calculation method for the scuffing load-carrying capacity of bevel and hypoid gears. Proceedings of the Institution of Mechanical Engineers, Part C: Journal of Mechanical Engineering Science, 233(21–22), 7328–7337. <https://doi.org/10.1177/0954406219843954>
- [26] Pellkofer, J., Hein, M., Stahl, K., Reimann, T., & Hombauer, M. (2019). New calculation method of the micropitting load carrying capacity of bevel and hypoid gears. International Conference on Gears 2019, 517–528. <https://doi.org/10.51202/9783181023556-517>
- [27] Siebert, B. R. L.; Sommer, K.-D. (2004). Weiterentwicklung des GUM und Monte-Carlo-Techniken (New Developments of the GUM and Monte Carlo Techniques). tm -Technisches Messen, 71(2), 67–80.
- [28] SMT MASTA Documentation. SMT. (n.d.). <https://www.smartmt.com/>
- [29] Sommer, K.-D.; Siebert, B. R.L. (2004). Praxisgerechtes Bestimmen der Messunsicherheit nach GUM. Technisches Messen, 71.
- [30] TechBlog. Antriebstechnik Software, Seminare, Kongresse. (n.d.). <https://www.fva-service.de/en/software/techblog/>
- [31] Thomas, J. (1998). Flankentragfähigkeit und Laufverhalten von hart-feinbearbeiteten Kegelrädern. Dissertation. TU München.

- [32] Várkuli, M. G., & Bognár, G. (2022). History of Gleason Works Spiral Bevel Gear Technology. *Design of Machines and Structures*, 12(2), 146–152. <https://doi.org/10.32972/dms.2022.024>
- [33] Vollhüter, F. (1992). Einfluss der Achsversetzung auf die Grübchen- und Zahnfußtragfähigkeit von spiralverzahnten Kegelrädern. Dissertation. TU München.
- [34] Weber, M. (2018). Entwicklung einer Vorrichtung zum Bestimmen und Einstellen des Tellerradeinbaumaßes im FZG-Hypoidverspannungsprüfstand sowie Ausarbeitung.
- [35] Weber, M. (2019). Untersuchungen zur Kalibrierung und Messunsicherheit an einem Hypoid-Wirkungsgradprüfstand (thesis).
- [36] Wirth, C. (2009). Zur tragfähigkeit von kegelrad- und hypoidgetrieben (thesis). Shaker.
- [37] Zusammenhang Technisches Datenblatt SHELL. (2023). <https://www.shell-livedocs.com/data/published/de-AT/2e7a1c41-905a-4e28-83e0-2394f9040dda.pdf>

A. Appendix A

Step of Test	Measured Value
Before 1 st preloading	0.018 V
After 1 st preloading	4.205 V
Before 2 nd preloading	0.024 V
After 2 nd preloading	4.177 V
Before 3 rd preloading	0.025 V
After 3 rd preloading	4.174 V
3-minute phase of relaxation	
Before installing calibration lever	0.017 V
After installing calibration lever	0.088 V
After installing hanger	0.259 V
After installing m_4	0.460 V
After installing m_5	0.720 V
After installing m_6	1.044 V
After installing m_7	1.424 V
After installing m_8	1.859 V
After installing m_9	2.367 V
After installing m_10	2.904 V

After installing m_11	3.514 V
After installing m_12	4.178 V
After removing m_12	3.519 V
After removing m_11	2.912 V
After removing m_10	2.354 V
After removing m_9	1.860 V
After removing m_8	1.423 V
After removing m_7	1.045 V
After removing m_6	0.722 V
After removing m_5	0.466 V
After removing m_4	0.263 V
After removing hanger	0.095 V
After removing calibration lever	0.028 V
After installing calibration lever	0.089 V
After installing hanger	0.260 V
After installing m_4	0.460 V
After installing m_5	0.722 V
After installing m_6	1.047 V
After installing m_7	1.419 V
After installing m_8	1.860 V
After installing m_9	2.367 V
After installing m_10	2.912 V
After installing m_11	3.520 V
After installing m_12	4.181 V

Table A.1: Measured data at Position 1

Step of Test	Measured Value
Before preloading	0.022 V
After preloading	4.178 V
3-minute phase of relaxation	
Before installing calibration lever	0.034 V
After installing calibration lever	0.088 V
After installing hanger	0.258 V
After installing m_4	0.459 V
After installing m_5	0.721 V
After installing m_6	1.041 V
After installing m_7	1.418 V
After installing m_8	1.861 V
After installing m_9	2.355 V
After installing m_10	2.901 V
After installing m_11	3.464 V
After installing m_12	3.986 V
After removing m_12	3.507 V
After removing m_11	2.915 V
After removing m_10	2.353 V
After removing m_9	1.862 V
After removing m_8	1.425 V
After removing m_7	1.044 V
After removing m_6	0.742 V

After removing m_5	0.473 V
After removing m_4	0.268 V
After removing hanger	0.088 V
After removing calibration lever	0.019 V

Table A.2: Measured data at Position 2

Step of Test	Measured Value
Before preloading	0.024 V
After preloading	4.169 V
3-minute phase of relaxation	
Before installing calibration lever	0.026 V
After installing calibration lever	0.090 V
After installing hanger	0.266 V
After installing m_4	0.459 V
After installing m_5	0.724 V
After installing m_6	1.044 V
After installing m_7	1.425 V
After installing m_8	1.860 V
After installing m_9	2.357 V
After installing m_10	2.903 V
After installing m_11	3.507 V
After installing m_12	4.218 V
After removing m_12	3.515 V
After removing m_11	2.907 V
After removing m_10	2.355 V

After removing m_9	1.864 V
After removing m_8	1.426 V
After removing m_7	1.046 V
After removing m_6	0.731 V
After removing m_5	0.461 V
After removing m_4	0.261 V
After removing hanger	0.094 V
After removing calibration lever	0.022 V

Table A.3: Measured data at Position 3

Step of Test	Measured Value
Before preloading	0.021 V
After preloading	4.066 V
3-minute phase of relaxation	
Before installing calibration lever	0.025 V
After installing calibration lever	0.088 V
After installing hanger	0.258 V
After installing m_4	0.457 V
After installing m_5	0.721 V
After installing m_6	1.045 V
After installing m_7	1.423 V
After installing m_8	1.859 V
After installing m_9	2.356 V
After installing m_10	2.910 V
After installing m_11	3.520 V

After installing m_12	4.184 V
After removing m_12	3.511 V
After removing m_11	2.903 V
After removing m_10	2.352 V
After removing m_9	1.859 V
After removing m_8	1.436 V
After removing m_7	1.044 V
After removing m_6	0.732 V
After removing m_5	0.464 V
After removing m_4	0.264 V
After removing hanger	0.092 V
After removing calibration lever	0.025 V

Table A.4: Measured data at Position 4

B. Appendix B



Figure B.1: Test Rig CAD Render Photo

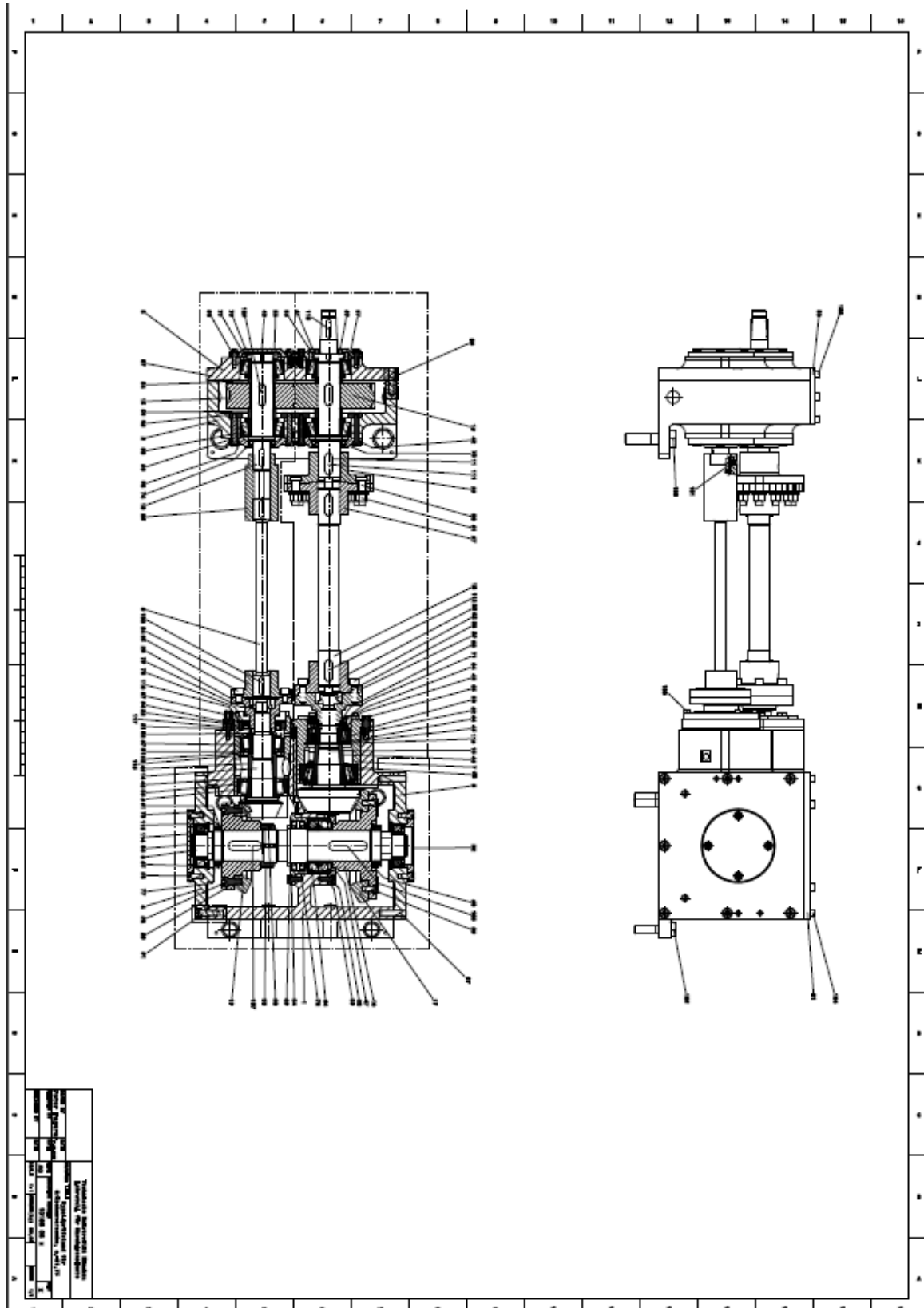


Figure B.2: G31.75 Test Rig 2D Assembly CAD

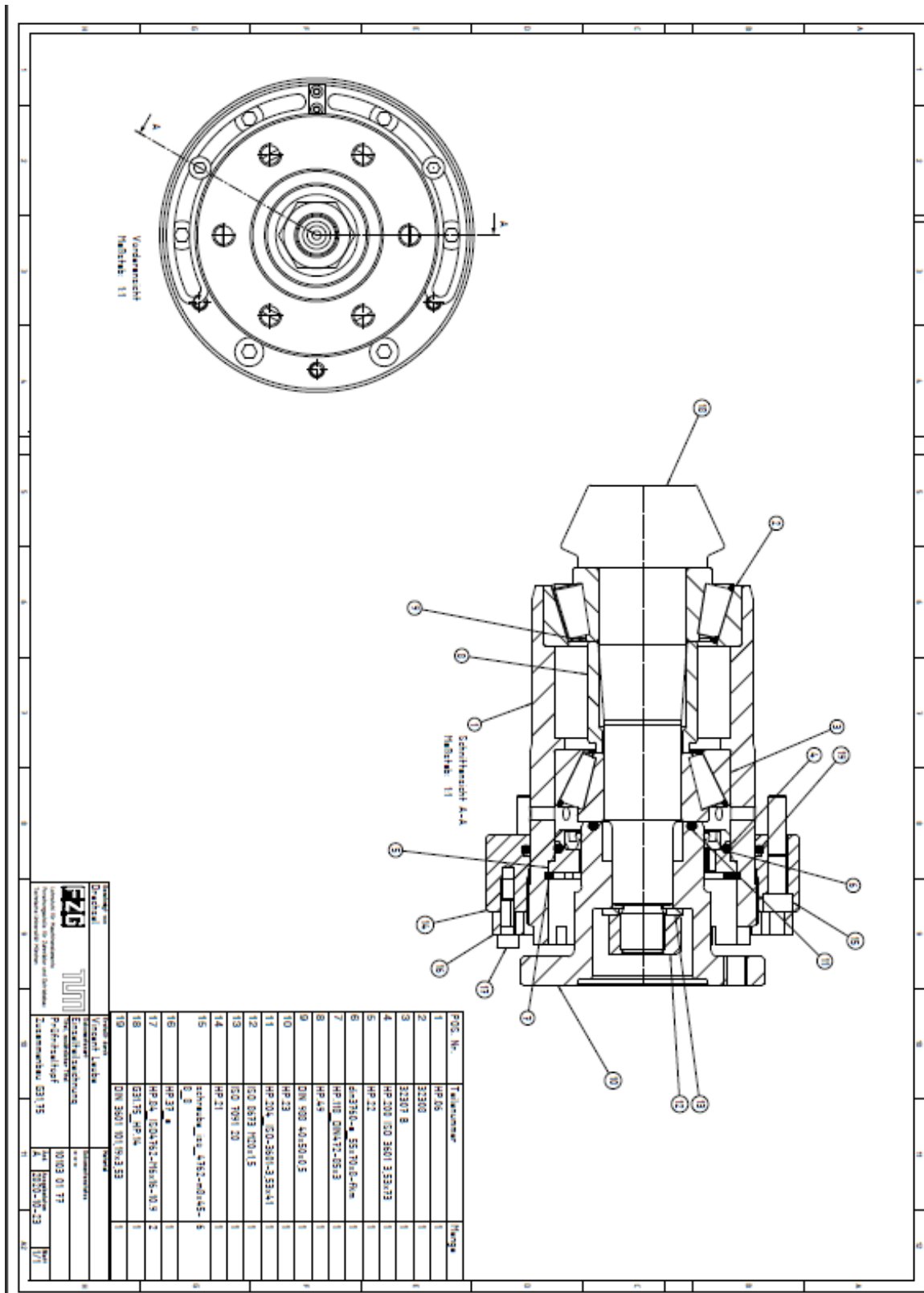


Figure B.3: G31.75 Test Pinion Pot 2D CAD

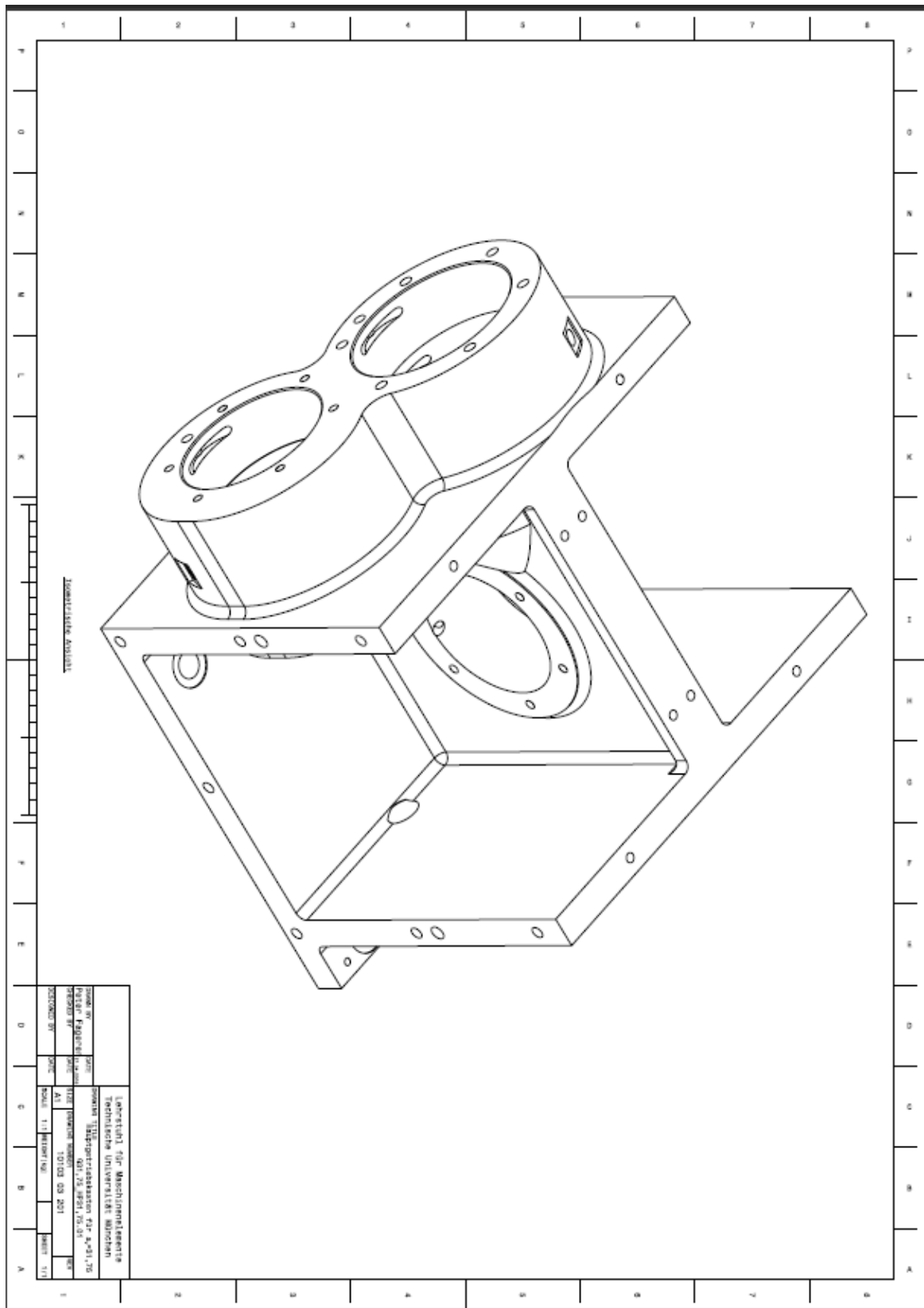


Figure B.4: G31.75 Housing 2D CAD

C. Appendix C

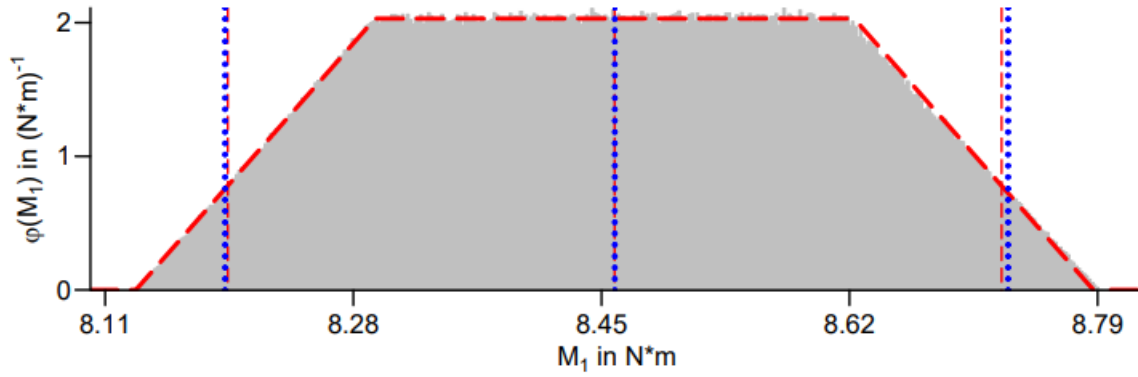


Figure C.1: M1 Distribution

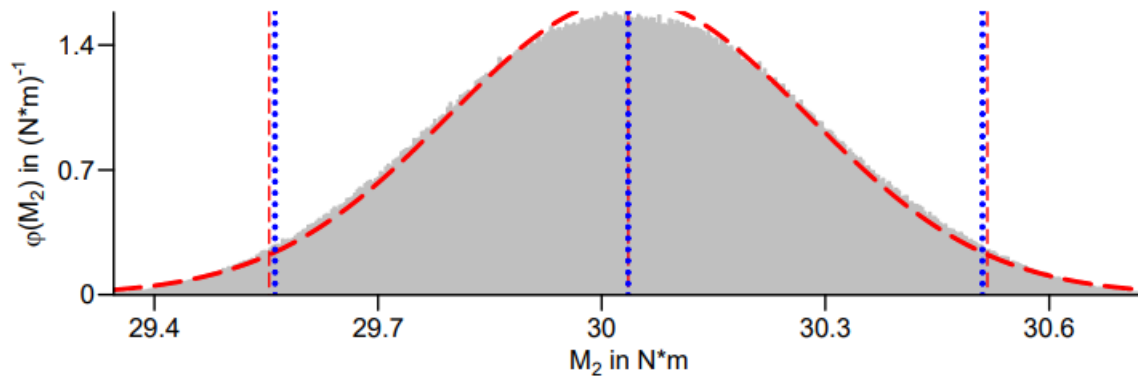


Figure C.2: M2 Distribution

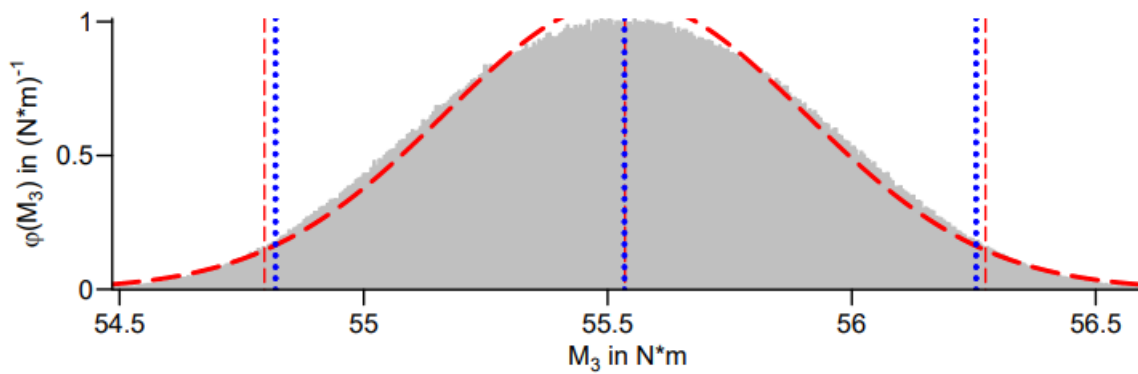


Figure C.3: M3 Distribution

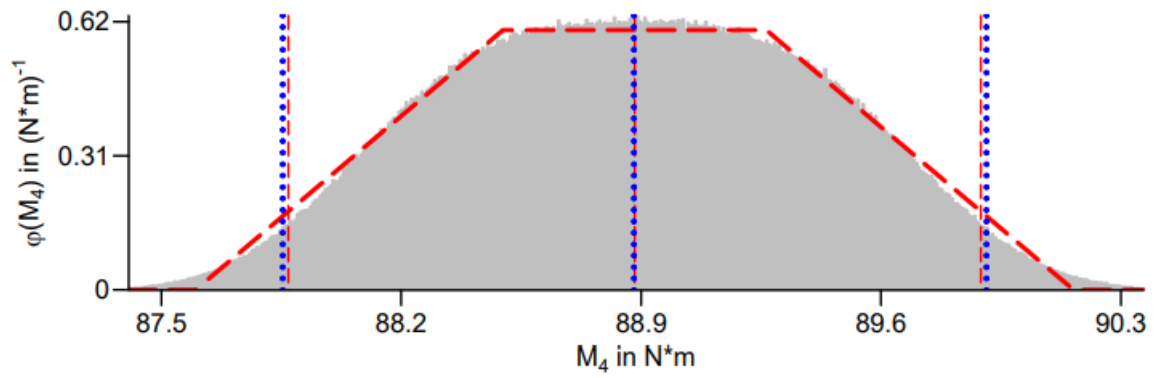


Figure C.4: M4 Distribution

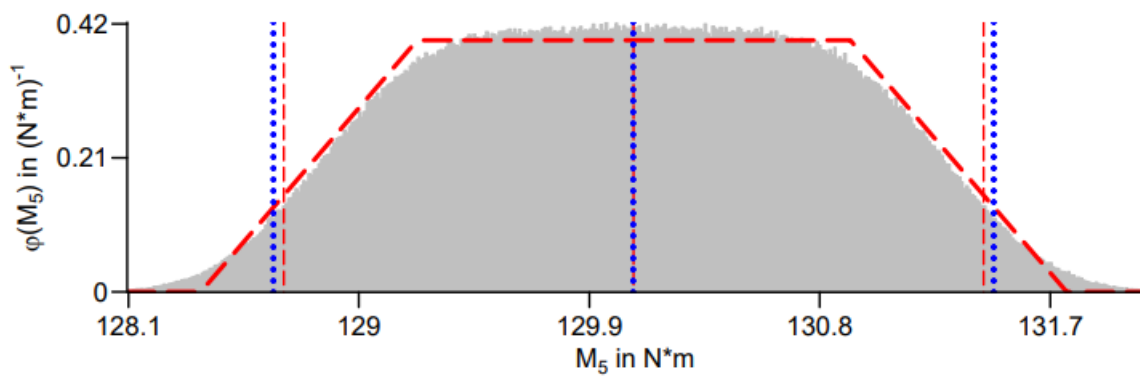


Figure C.5: M5 Distribution

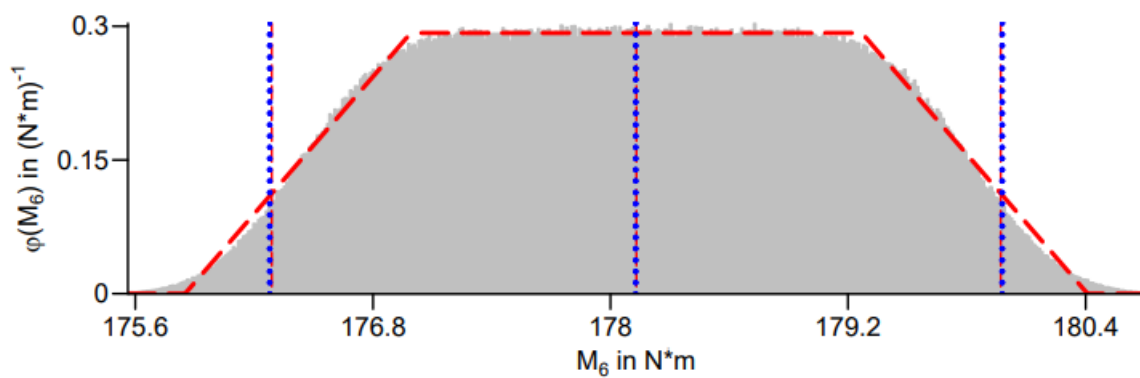


Figure C.6: M6 Distribution

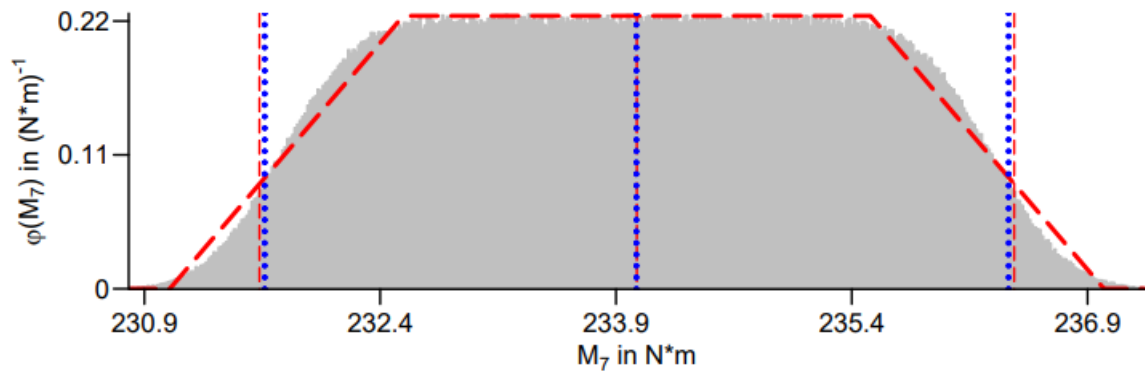


Figure C.7: M7 Distribution

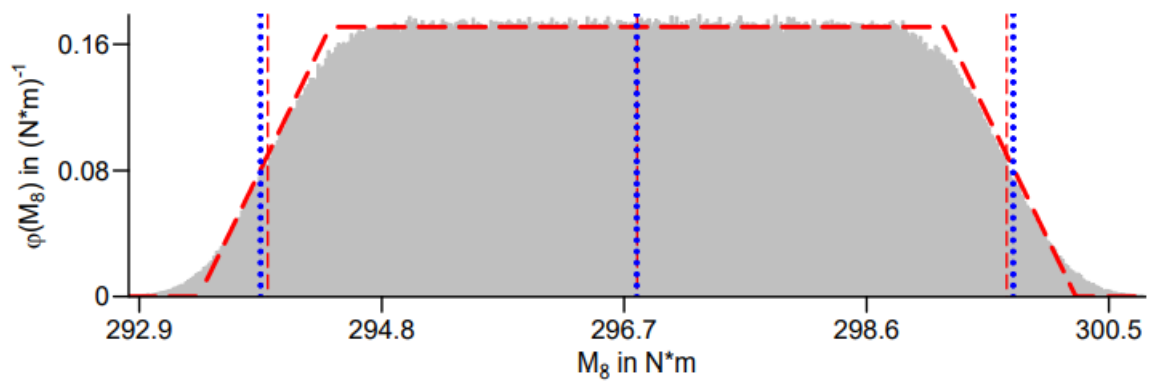


Figure C.8: M8 Distribution

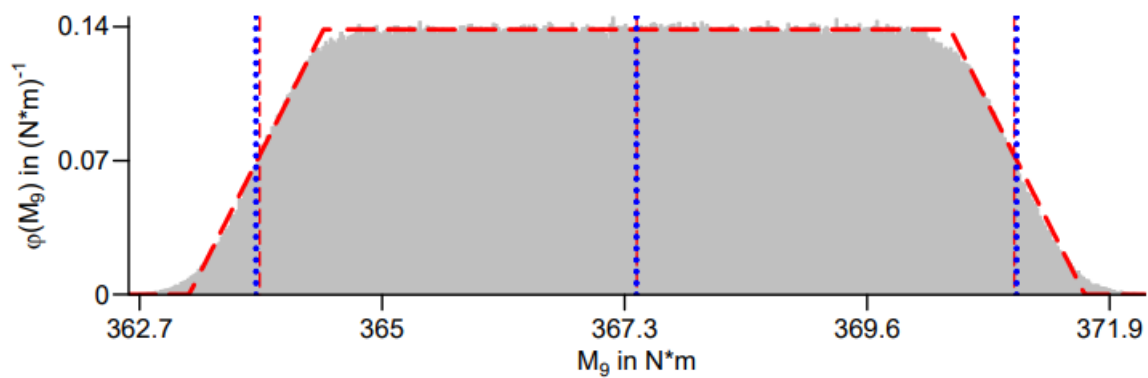


Figure C.9: M9 Distribution

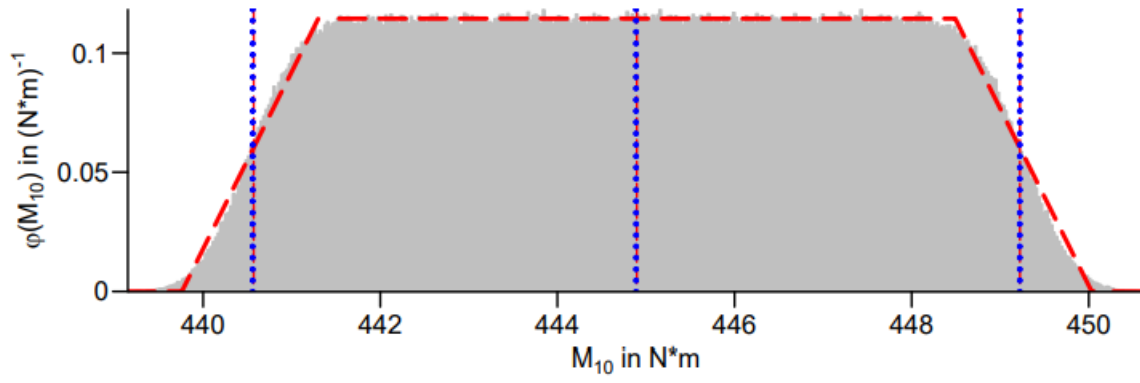


Figure C.10: M10 Distribution

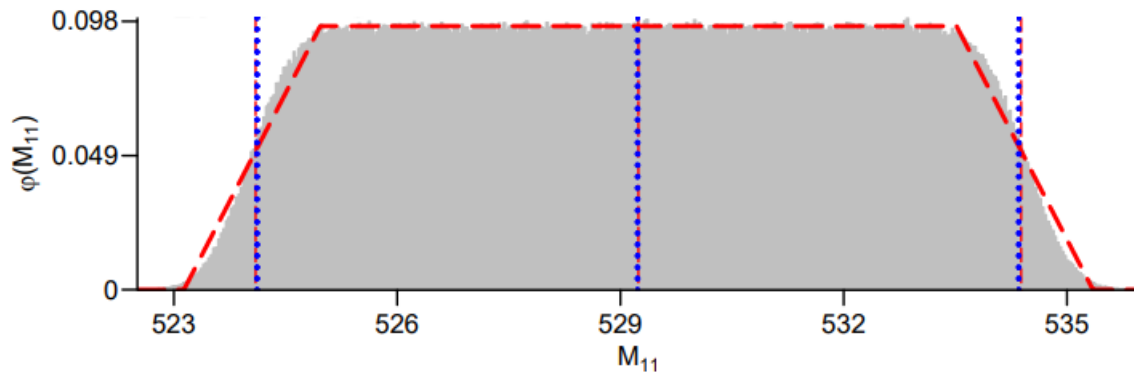


Figure C.11: M11 Distribution

List of Figures

Figure 1.1.1: Straight, skew and spiral bevel gears [21].....	5
Figure 1.2.1: Bevel gear pair.....	8
Figure 1.2.2 : Bevel gear geometry definition in the axial section [13]	9
Figure 1.2.3: Definition of the bevel gear geometry in the mean transverse section [13]	9
Figure 1.2.4: Hypoid gear geometry definition [13]	10
Table 1.2.3: Bevel Gear Designations for Figure 1.2.5 [21].....	10
Figure 1.3.1: Pitting on the Flank Surface [21].....	13
Figure 1.3.2: Crack directions, rolling, and sliding on a gear tooth flank [21]	15
Figure 1.3.3: Micropitting on the Flank Surface [21]	16
Figure 1.4.1: Illustration of the relationships between the calculation techniques for the load carrying capacities of bevel gears explained in the paper by Drechsel et al. [7].	25
Figure 1.4.2: Comparison of the extended approach, ISO 10300-2:2014 and LTCA methods for Hertzian contact stress, permissible contact stress, and safety factor against pitting for G31.75 Gear Set [7].....	26
Figure 1.5.1 : Typical pitting at the pinion flanks on the investigated test gears [10].	27
Figure 1.5.2: left: micro pitting and pitting on pinion flank , right: initial pitting at the addendum of the pinion ($T_1 = 300 \text{ Nm}$, $a = 15 \text{ mm}$) [10].....	27
Figure 1.5.3 : Calculated and Experimentally Investigated Results of Pitting [10].....	28
Figure 1.6.1 : Result types (right) and available methods for rating strength (left) [1]	30
Figure 2.1.1: FZG Back-to-Back Hypoid Test Rig [25].....	34
Figure 2.1.2: Bevel and hypoid gear test rig scheme [8]	35
Figure 2.1.3: Representation of Misalignments [25]	36
Figure 4.1: Graphical Description of the Analysis of Influences of Factors.....	46
Figure 4.1.1: Some analysis modules on MASTA [28]	47
Figure 4.1.2: Gear Import Module and Gear Pair 3D Visualization [28].....	48
Figure 4.1.3: MASTA LTCA 3D View [28].....	49

Figure 4.1.4: Example for MASTA Report	51
Figure 4.2.1: 3D view of modeled testing mechanism	52
Figure 4.2.2: Contact Pattern Visualization on KIMoS [20].....	53
Figure 4.2.3: Test Pinion Housing of G31.75	55
Figure 4.2.4: Meshed Housing(G31.75) in ANSYS	56
Figure 4.2.5: Mesh Statistics	56
Figure 4.2.6: Meshed Housing (G31.75) in MASTA	56
Figure 4.3.1: Misalignment Representation on MASTA [28]	58
Figure 4.3.2: Variation of Shaft angle with respect to different preloading values on pinion shaft bearings, under varying input torque quantities	59
Figure 4.3.3: Variation of Wheel axial displacement with respect to different preloading values on pinion shaft bearings, under varying input torque quantities.	60
Figure 4.3.4 : Variation of pinion axial displacement with respect to different preloading values on pinion shaft bearings, under varying input torque quantities.	60
Figure 4.3.5: Variation of Wheel radial displacement with respect to different preloading values on pinion shaft bearings, under varying input torque quantities.	61
Figure 4.3.6: Comparison between reference results and current simulation results.	62
Figure 4.3.7: Variation of pinion axial displacement with respect to input torque on pinion shaft bearings, under varying preloading on pinion shaft bearings.....	63
Figure 5.1.1: BECAL FVA [18]	65
Figure 5.2.1: Becal Input 1	66
Figure 5.2.2: Becal Input 2	67
Figure 5.2.3: Becal Input 3	67
Figure 5.3.1: The maximum flank pressure variation with respect to preloading on pinion shaft bearings.....	72
Figure 5.3.2 : Flank pressure variation with respect to preloading on pinion shaft bearings for different torque values	73
Figure 6.1.1: Calibration procedures for various installation positions, accordance to DIN 51309 [3]	79
Figure 6.1.2: Expanded measurement uncertainty as value interval.....	88
Figure 6.2.1: Schematic view of lever-mass system used to calibrate the torque measurement system	92
Figure 6.2.2: Attachment of double-lever for unloading the test rig	93
Figure 6.2.3: Fuser Unit.....	94

Figure 6.2.4: Calibration Lever	94
Figure 6.2.5: Hanger	95
Figure 6.2.6 :Calibration Weights.....	95
Figure 6.2.7: The Calibration Setup Installed on the FZG Hypoid Test Rig.....	96
Figure 6.2.8: Basic Load Spectrum	98
Figure 6.2.9: Reduced Load Spectrum.....	99
Figure 6.3.1: Curve Fitting between Display Values and Calibration Torque	101

List of Tables

Table 1.1.1: Overview of the main manufacturing techniques for spiral bevel gears [21]	7
Table 1.2.1: Bevel Gear Designations for Fig 1.2.2 [21]	8
Table 1.2.2: Bevel Gear Designations for Fig 1.2.3 [21]	10
Table 1.2.3: Bevel Gear Designations for Figure 1.2.5 [21].....	10
Table 1.2.4 : Coast and Drive Tooth Flanks [21].....	11
Table 1.4.1: Factors for ZM-B [12].....	22
Table 2.1.1: Lubricant Properties [36, 37]	37
Table 2.1.2: Test Gear Parameters [7].....	38
Table 3.3.1: Results of experiments on G31.75 Test Rig with 400 Nm torque	43
Table 3.3.2: Some Critical Results (in addition to the Table 3.3.1).....	44
Table 4.2.1: Gear Geometrical Dimensions for G31.75.....	54
Table 5.3.1: BECAL 400 Nm test results for different preload values	70
Table 5.3.2: BECAL Result & Actual Contact Pattern	71
Table 5.3.3: Preloading on Pinion Shaft Bearings (μm).....	75
Table 6.1.1: Steps for torque calibration in accordance with DIN 51309 [3]	80
Table 6.1.2: Important variables influencing the display according to DIN 51309 [3] 90	
Table 6.1.3: Relative standard deviations of the characteristic values determined from experimentally determined data according to DIN-51309 [3].	91
Table 6.2.1: Mass values of Calibration weights	97
Table 6.3.1: Measured and averaged display values.....	100
Table 6.3.2: Display values and Calibration Torque values	101
Table 6.3.3: Reproducibility, Zero-point deviation, Interpolation deviation, Resolution	102
Table 6.3.4: Standard deviations of physical quantities used to calculate calibration torques.....	102
Table 6.3.5: Calibration torque values with relative standard deviations	103

Table 6.3.6: Relative Standard Deviations and Relative Extended Uncertainty	103
Table 6.3.7: Relative extended uncertainty and Absolute extended uncertainties	104

List of Symbols

I_j	Display in loaded condition with increasing calibration torque
I'_j	Display in loaded condition with decreasing calibration torque
I_0	Display in unloaded condition before start of measuring series
$I_{f,j}$	Zero value after downward series
I_{NVB}	Display value immediately after the third preload
I_{3min}	Display value 3 minutes after the third preload
M_k	Calibration torque
X_j	Display value of the upward series corrected by the zero value
X'_j	Display value of the downward series corrected by the zero value
f_a	Interpolation error
n	Number of shaft positions
h	Reversal span
Y, Y_h	Calibration result at calibration torque
b	Reproducibility
b'	Repeatability

f_0	Zero-point deviation
Y_a, Y_{ah}	Compensation function value
f_q	Display deviation
KZK	Short-time creep
y	Estimated value for the measurand
u_y	Combined standard deviation of the measurement result
u_{xixj}	Estimated covariance of the variables
r	Correlation coefficient
x_i	Expected values of input variables
u_{xi}, u_{xj}	Standard deviations of the input variables
c_i, c_j	Sensitivity coefficients
I_y	Interval from estimated value
U_y	Extended measurement uncertainty
k_p	Coverage factor
C	Factor for considering a unit of display deviating from the torque unit
δX_i	Influencing variables on the display X_i
δX_1	Influence of the resolution of the display unit on the zero value
δX_2	Influence of the resolution of the display unit on the display value
δX_3	Influence of reproducibility
δX_4	Influence of repeatability
δX_5	Influence of the zero-point deviation

δX_6	Influence of the display deviation or the interpolation deviation
δX_7	Influence of the reversal span
w	Standard measurement uncertainty
w_r	Relative standard deviation determined by the influence of resolution
$w_{b'}$	Relative standard deviation determined by the influence of repeatability
w_b	Relative standard deviation determined by the influence of reproducibility
w_{fa}	Relative standard deviation determined by the influence of the interpolation deviation
w_0	Relative standard deviation determined by the influence of zero-point deviation
K_A	Application factor
K_v	Dynamic factor
$K_{H\beta}$	Face load factor
$K_{H\alpha}$	Transverse load factor
σ_{HO-B1}	Nominal value of contact stress
F_n	Nominal normal force
l_{bm}	Length of contact line in the middle of the zone of action
ρ_{rel}	Radius of relative curvature
Z_{M-B}	Mid-zone factor
Z_{LS}	Load-sharing factor
Z_E	Elasticity factor

Z_K	Bevel gear factor
$\sigma_{H,lim}$	Allowable stress
Z_{NT}	Life factor
Z_X	Size factor
Z_L, Z_V, Z_R	Lubricant film factors
Z_W	Work hardening factor
Z_{Hyp}	Hypoid factor
S	Safety factor
a	Axial offset
m	Gear module
ΔE	Wheel radial displacement
ΔXP	Pinion axial displacement
ΔXW	Wheel axial displacement
$\Delta \Sigma$	Shaft angle

Acknowledgements

I am extremely grateful to everyone who has supported and encouraged me by standing by my side on this important journey to complete my thesis. My sincerest gratitude goes to my parents, Kıymet and Dr. Ferhat, who have been my guiding light with their love and support throughout this endeavor. Special thanks go to my girlfriend Özgü for always being there for me, and to my dear closest friend Tural, who has been my companion both during the thesis process and throughout my master's program. I would like to thank Mr. Lorenz Constien and Mr. Luca Bonaiti for their priceless academic guidance and help. I would also like to express my sincere gratitude to Professor Karsten Stahl for giving me the opportunity to research at the FZG and to Professor Carlo Gorla for all his support. This thesis is a testament to the collective support and contributions of these exceptional individuals. I am extremely grateful to each of you for the part you have taken in my academic journey.

With my deepest appreciation,

Utku AYRANCILAR

The completion of this thesis could not have been possible without great contributions and support of several academic personnel and my close people. Apart from my project partner Mr. Ayrancilar, with whom we shared many great moments within the entire study period at master's degree, I would like to present my warmest thanks to Prof. K. Stahl who accepted my application for collaborative thesis project at FZG. My sincere gratitude also goes to Mr. Constien and Mr. Bonaiti, due to their remarkable guidance with appropriate comments and suggestions. Moreover, I appreciate Prof. Gorla's admirable assist at Polimi side and kindly thanks. Meanwhile, I have to mention great support and attention of my family who have sincerely followed me at the all stages of my life. To be honest, I cannot put into words completely the valuable effort and motivational support of my parents, Shafahat Aghayev and Madina Aghayeva. All the priceless suggestions of my brother Dr. A. Aghayev have undeniably contributed to my academic career as well.

With my profoundest gratitude,

Tural AGHAYEV

